项目组人员情况证明

项目主持人，**黄涌**，男，40 岁，讲师，目前是广东技术师范大学广东工业实训中心在职人员普通教师。特此证明！

项目参与人员信息表

姓名	性别	年龄	职务/职称	工作单位	分工	人员类别
张建伟	男	1988.2	无	广州海芯教育科技有限公司	平台运营	普通教师
严力超	男	1986.2	副研究员	广州市教育研究院	课程研发	普通教师

项目主持人所在学院盖章：

教务处盖章：

2021年11月17日

2021年省高等职业教育教学质量与教学改革工程项目

基于“双模套件+云计算智能教学平台”的高职《人工智能》课程教学改革与实践

支撑材料

支撑材料目录

一、 教学项目

1. 广东技术师范大学质量工程项目，《电路》——线上课程
2. 教育部产学合作协同育人项目，《基于“引企入校，协同育人”模式的 3D 打印人才培养基地建设》
3. 横向项目，《人工智能系列之机器学习应用开发》
4. 横向项目，《开发人工智能基础虚拟仿真实训课程，共建“人工智能基础标注中心”》

二、 教学论文

1. 基于 RC 电路频率响应特性在教学中的研究，电子技术与软件工程，2021.8，209(8):59-61。
2. 混合式教学法在电路教学实践中的应用探索，广东技术师范大学学报，2020.6，41(3):78-82。

三、 教学奖励

1. 2020 校级本科教学观摩竞赛特等奖
2. 2020 校级教师教学创新大赛一等奖
3. 教学学术创新奖（排名第一）
4. 2019-2020 年教学质量优秀奖
5. 2020 年校级教学成果奖一等奖(排名第 4)
6. 2017 年广州市科普讲解大赛二等奖、广州市优秀科普使者，
7. 2017 年广州市科普先进个人

四、 科研项目

1. 广东省教育厅，2019 年，2019KTSCX084，可见光通信器件载流子与频率响应及光效特性机理的研究，9 万，已立项，主持；
2. 广东省科技计划项目，2016 年，2016A070714004，增材制造（3D 打印）科技创新创业人才培训服务体系建设，50 万元，已结题，主持；

五、 科研论文

1. Huang Y, Wang Y, Bai P, et al. Storage Mechanism of Alkali Metal Ions in the Hard Carbon Anode: an Electrochemical Viewpoint[J]. ACS Applied Materials & Interfaces, 2021, 13(32): 38441-38449.(SCI)
2. Yong Huang, Zhiyou Guo, Miao Zhang and Dan Xiang, Improved Performance of GaN-Based Ultraviolet LEDs With Electron Blocking Layers Composed of Double-Peak p-Type $Al_xGa_{1-x}N$/GaN Superlattice Layers, IEEE Access, 2021.4.27, 9, 65246 – 65253 (SCI)
3. Yong Huang, Zhiyou Guo, Xiaojun Huang, Huazhi Li and Dan Xiang, GaN-based high response frequency and high optical power matrix micro-LED for visible light communication, IEEE Electron Device Letters, 2020.10.2, 41(10):

1536-1539; (SCI)
4. Yong Huang, Zhiyou Guo , Hongyong Huang, and Huiqing Sun, Influence of Current density and Capacitance on the Bandwidth of VLC LED, IEEE photonics technology letters 2018.5.1, 30(9): 773~776；(SCI)
5. Yong Huang, Zhi-You Guo, Hui-Qing Sun, and Hong-Yong Huang Micro light emitting diodes Array with dual functions of visible light communication and illumination, Chinese physics B, 2017.8.20, 26(10): 108504. (SCI)

1.教学项目

广东技术师范大学文件

广师大〔2020〕208号

广东技术师范大学关于公布2020年校级质量工程建设项目立项名单的通知

各相关单位:

为进一步深化我校本科教育教学内涵建设，更好地与省级、国家级教学质量与教学改革工程申报工作相衔接，根据《关于开展2020年校级教学质量与教学改革工程申报工作的通知》文件要求，我校开展了校级教学质量与教学改革工程（以下简称“质量工程”）项目申报评审工作。经教师申报、教学单位推荐、学校组织校外评审专家评审、网上公示，确定漆艺等49项2020年校级质量工程建设项目。现将立项名单予以公布，并就有关事项通知如下。

序号	项目编号	所在单位	项目类型	项目负责人	职称	项目名称	团队成员	支持经费
13	2020zlgc13	机电学院	在线开放课程	陈飞昕	讲师	工程力学	宋雷、李纬华、陈天祥、刘大纬、张广潮、钟炜源、陈弘州	3
14	2020zlgc14	工业中心		黄涌	讲师	电路	向丹、赵先美、李争名、向英、马锐军	3
15	2020zlgc15	汽车与交通工程学院		李薇	讲师	交通仿真软件分析与应用	徐伟、杜灿谊、李锋、容颖、王思卓、邓雯苑	3
16	2020zlgc16	外国语学院		黄南芳	讲师	新闻英语视听说	张艳、刘星莹、苏丹、王思思、高阿林	3
17	2020zlgc17	自动化学院		袁飞	讲师	传感器与检测技术	唐德翠、祁伟、刘军、庄志惠	3
18	2020zlgc18	文学与传媒学院		杨欣	讲师	用图说话—漫谈摄影	邓文新、孙墀、王汀若、潘锡荣	3
19	2020zlgc19	财经学院		陈平	讲师	政府与非营利组织会计	刘国庆、蔡军、蔡文英、张颜瑜、唐霏	3
20	2020zlgc20	机电学院		左茜	讲师	材料成型原理	王敏，曹耿华，刘一雄，陈飞昕，莫玲，赵泽盈	3
21	2020zlgc21	自动化学院	卓越工程师教育培养计划试点专业	张先勇	副研究员/副院长	电气工程及其自动化	周卫，岑健，肖蕾，王华秀，伍银波，李丽，郑辞宴，熊建斌，胡俊敏，朱鹰屏，班勃，徐金雄，柳澹，周龙华，陈冰，冯小峰，张继元	5
22	2020zlgc22	数学与系统科学学院	卓越教师培养计划试点专业	陈玉明	副教授/专业负责人	数学与应用数学(师范)	梁海华、黄凤英、王燕、张淑玲、张广亮、付辉、魏凯飞、蔡映霞、洪虹、李宏奕、张俊生	5
23	2020zlgc23	外国语学院		贺显斌	教授/院长	英语（师范）	陈冬桂、张彦琳、蒋银健、徐玲、邵朝杨	5
24	2020zlgc24	文学与传媒学院		白崇	教授/副院长	汉语言文学（师范）	余爱春、贺根民、徐红梅、项裕荣、曾洁、刘莱琳、刘竞、朱华英、蒋颖、林庆	5

省级教研教改项目认定书

项目类别：教育部产学合作协同项目（2019年第二批）

项目名称：基于“引企入校，协同育人”模式的3D打印人才培养基地建设

立项编号：201902122030

项目负责人：黄涌

项目组成员：向丹

根据学校教学指导委员会委员会议决议，已完成结题并通过验收的教育部产学合作协同育人项目、广东省校企合作协同育人项目，可认定为省级教研教改项目。本项目符合条件，现认定为省级教研教改项目，编号：2021SJJYJGRD024。

广东技术师范大学教务处

2021年07月12日

合同编号：

技术开发（委托）合同

项目名称：　人工智能系列之机器学习应用开发

委托方（甲方）：　广东智道智能信息股份有限公司

受托方（乙方）：　广东技术师范大学

签订日期：　2021年7月9日

签订地点：　广州科学城科研路3号A5栋

有效期限：　2021年7月10日 至2021年12月31日

中华人民共和国国家科学技术部印制

本合同甲方委托乙方研究开发 人工智能系列之机器学习应用开发 项目，并支付研究开发经费和报酬。乙方接受委托并进行此项研究开发工作。双方经过平等协商，在真实、充分地表达各自意愿的基础上，根据《 中华人民共和国合同法 》的规定，达成如下协议，并由双方共同恪守。

第一条 本合同研究开发项目的要求如下：

1．技术目标： 开发适用于甲方制定的中小学人工智能系列之机器学习教材相关的人工智能模块，开发与教材配套的课程，开展相应的技术培训和技术咨询服务。

。

2．技术内容： 制定教材中人工智能的主流应用场景和实现方法，内容覆盖人工智能的核心主题领域，并运用到教学当中；人工智能在基本的图像和语音语义应用；人工智能的其它典型应用案例展示，以及大数据和人工智能的社会影响展示等。

3．技术方法和路线： 包括制定教材中的教具硬件、软件开发，及配套 PPT 讲稿编写、微课编辑，教具使用培训等。

第二条 乙方应在本合同生效后 30 日内向甲方提交研究开发计划。研究开发计划应包括以下主要内容：

1. 指定教材配套的教具研发计划；
2. 指定教材的培训计划及教学方案；
3. 技术服务以及咨询等服务实施计划和保障措施；
4. 无。

第三条 乙方应按下列进度完成研究开发工作：

1. 2021年7月至8月 人工智能教具研发工作 ；
2. 2021年8月至9月 技术培训服务 ；
3. 2021年9月至12月 课程开发及技术总结 ；
4. ；

第四条 甲方应向乙方提供的技术资料及协作事项如下：

1. 技术资料清单： 制定教材相关套件的技术研发资料以及课件等乙方必要的技术资料；

。

2. 提供时间和方式： 2021年7月31日

。

3. 其它协作事项： 无

本合同履行完毕后，上述技术资料按以下方式处理： 交还甲方

。

第五条 甲方应按以下方式支付研究开发经费和报酬：

1. 研究开发经费和报酬总额为 10万元 。

其中：(1) 技术研发4万元 ；

(2) 课程开发1.2万元 ；

(3) 技术培训和技术咨询4.8万 ；

(4) 。

2. 研究开发经费由甲方 一次 （一次、分期或提成）支付乙方。具体支付方式和时间如下：

甲方：广东智道智能信息股份有限公司（盖章）

法定代表人/委托代理人（签名）

2021年7月9日

乙方：广东技术师范大学（盖章）

项目负责人：（签名）

法定代表人/委托代理人：（签名）

2021年7月9日

合 同 书

委托方（甲方）：广州市贸易职业高级中学

受托方（乙方）：广东智道智能信息股份有限公司

项目名称：开发人工智能基础虚拟仿真实训课程，共建“人工智能基础标注中心”

签订时间：2021 年 8 月 2 日

根据甲方人工智能基础课程及共建“人工智能基础课程仿真工具 LV1”，单一来源采购结果，按照《中华人民共和国政府采购法》、《中华人民共和国合同法》的规定，经双方协商，本着平等互利和诚实信用的原则，一致同意签订本合同如下。

第一条 服务内容与要求

1.技术服务的目标：协助学校开发人工智能基础虚拟仿真实训课程，共建”人工智能基础标注中心”，合作开办人工智能基础标注师班，建立校外实习基地并提供相应的咨询服务。

2.技术服务的内容、服务方式、时限：

序号	项目内容	技术要求简述	服务（完成）期限
1	协助学校开发人工智能基础虚拟仿真实训课程	（1）学校成立 1 个课程开发团队，企业为开发团队聘请 1 位企业实践专家； （2）企业为《人工智能基础虚拟仿真实训》课程开发提供各类企业真实场境案例 10 个、仿真案例 10 个； （3）安排专业教师到企业实践（不少于 1 人），并安排技术能手对专业教师进行指导； （4）聘请专家（3 人或以上）对开发的教材进行审核与评估。	协议签订日至 2021 年 12 月 30 日
2	共建“人工智能基础课程仿真工具 LV1”	（1）安排企业技术人员（1 名或以上）协助开发“人工智能基础课程仿真工具 LV1”； （2）工具功能需求：1、化繁为简的算法，机器学习更具象化，界面交互更简单，2、拍摄实物即刻学习物品特征，再将训练成果运用到编程。3、基于机器学习的数据，利用编程体现其中蕴含的规律或判断规则，深入浅出地探究和学习人工智能原理； （3）接收学校相关专业教师和学生在企业内实习；企业技术人员进行指导；	协议签订日至 2021 年 12 月 30 日
3	合作开办人工智能标注师班	（1）从二年级学生中双向选择合适的学生成立人工智能标注师班，不少于 20 人； （2）安排企业技术骨干到校为订单班学生授课，每学期不少于 10 次；	协议签订日至 2022 年 3 月 31 日

		（3）提供基础班的授课计划表及任课教师的简历； （4）安排企业技术骨干到校协助部分专业课程教学。	
4	建立校外实习基地	（1）成立校外实习基地，接纳我校相关专业学生到企业职业体验、见习和顶岗实习（每年顶岗实习不少于 10 人）； （2）为我校相关专业学生提供岗前培训和见习、实习指导； （3）提供岗前培训授课计划； （4）对我校顶岗实习学生给予考核和评价	协议签订日至 2022 年 3 月 31 日

第二条 合同金额

合同总额人民币小写：¥60000；大写：陆万元整。

第三条 付款方式

1.合同签订日起 30 天内，支付第一期为总额的 70%；

2.本项目验收后的 30 天内，支付第二期为总额的 30%。

如果由于财政支付进度原因造成的资金延误支付，甲方不承担延误支付责任。

第四条 甲乙双方的权利和义务

1. 甲方的权利和义务

（1）甲方成立 1 个课程开发团队，在乙方企业专家的协助下完成《人工智能基础虚拟仿真实训》课程的开发；

（2）甲方安排课程开发组教师到乙方场所进行企业实践；

（3）甲方做好人工智能标注师班双向选择的组织工作及教学管理工作；

（4）甲方做好学生到乙方开展职业体验和实习的组织管理工作。

2. 乙方的权利和义务

（1）乙方需聘请行业专家参与甲方的课程开发小组，并为甲方的课程开发提供企业真实场境案例等资源；

（2）乙方为甲方课程开发教师提供企业实践机会，安排企业技术人员对甲方专业教师进行指导；

（3）乙方聘请专家对甲方开发的教材进行审核与评估；

（4）乙方与甲方共同做好人工智能标注师班的管理工作，乙方接纳甲方专

业学生到乙方开展职业体验、见习和顶岗实习，做好岗前培训和实习指导，并对甲方学生的顶岗实习给予考核和评价。

第五条　验收方式

由甲方组织专家评审验收。

第六条　售后服务要求

乙方须配合甲方的要求，对项目继续提供后续服务和指导。

第七条　保密要求

甲方：

1.保密内容：合作期间乙方相关企业案例资料。

2.涉密人员范围：相关参与项目的教师。

3.保密期限：五年。

4.泄密责任：承担违约责任并赔偿乙方造成的损失。

乙方：

1.保密内容（包括技术信息和经营信息）：合作期间双方相关课程开发的相关资料。

2.涉密人员范围：相关参与项目的人员。

3.保密期限：五年。

4.泄密责任：承担违约责任并赔偿乙方造成的损失。

第六条 本合同的变更必须由双方协商一致，并以书面形式确定。

第七条 双方确定：在本合同有效期内，技术服务工作成果所完成的新的技术成果，归双（甲、乙）方所有。

第八条 双方确定，按以下约定承担各自的违约责任：

1. 甲方违反本合同第二、四、七条约定，应当在履行义务或者积极采取补救措施后，赔偿乙方造成的损失额30%。

2. 乙方违反本合同第二、四、七条约定，应当在履行义务或者积极采取补救措施后，赔偿甲方造成的损失额30%。

第九条 本合同一式肆份，具有同等法律效力。

第十条 本合同经双方签字盖章后生效。

（以下无正文）

甲方： 广州市贸易职业高级中学

地址： 广州市中山六路瑞兴新街7号

法人代表：陈建瑜

电话：13600006351；020-83329736

开户银行： 工行广州庙前直街支行

账号：3602001029200132416

签署日期：2021 年 8 月 2 日

乙方： 广东智道智能信息股份有限公司

地址：广州市高新技术产业开发区科学城科研路 3 号自编 A5 栋 104/106 房

法人代表：张建伟

电话：15014151184；020-32201448；

开户银行：中国银行股份有限公司广州华南碧桂园支行

账号：7107 7158 0520

签署日期：2021 年 8 月 2 日

2.教学获奖

荣誉证书

黄　涌　老师：

荣获广东技术师范大学二〇二〇年本科课堂教学观摩竞赛特　等奖。

特发此证，以资鼓励。

广东技术师范大学

2020年11月29日

荣誉证书

黄涌、胡李亚洲、钟森鸣老师：

荣获广东技术师范大学首届教师教学创新大赛决赛（中级组）一等奖。

特发此证，以资鼓励。

广东技术师范大学

二〇二一年一月

荣誉证书

黄涌、胡李亚洲、钟森鸣老师：

荣获广东技术师范大学首届教师教学创新大赛决赛 教学学术创新奖。

特发此证，以资鼓励。

广东技术师范大学

二〇二一年一月

荣誉证书

黄　涌同志被评为2019—2020学年度课堂教学质量优秀教师，特发此证，以资鼓励。

广东技术师范大学

二〇二〇年七月

荣誉证书

2020年度广东技术师范大学校级教学成果奖

获奖成果： 基于产教融合的“新工科”大电类公共教学平台建设探索与实践

主要完成人： 向丹、王晓军、姚屏、黄涌、马锐军、杨忠高

获奖等级： 一等奖

广东技术师范大学

2021年5月20日

荣誉证书

CERTIFICATE OF HONOR

黄涌 同志：

在2017年广州地区科普讲解大赛（开发区分赛区）中荣获 二 奖。特发此证，以资鼓励。

广州开发区科技创新和知识产权局

广州开发区科学技术协会

2017年4月5日

荣誉证书

同志：

在2017年广州地区“讲科学、秀科普”大赛暨2017年全国科普讲解大赛选拔赛中表现优异，荣获“二等奖”。

特发此证，以资鼓励。

广州市科技创新委员会　共青团广州市委员会

二〇一七年四月二十八日

荣誉证书

黄涌同志：

在2017年广州地区“讲科学、秀科普”大赛暨2017年全国科普讲解大赛选拔赛中表现优异，荣获“最佳形象奖”。

特发此证，以资鼓励。

广州市科技创新委员会　共青团广州市委员会

二〇一七年四月二十八日

荣誉证书

黄涌 同志：

在2017年广州地区“讲科学、秀科普”大赛暨2017年全国科普讲解大赛选拔赛中表现优异，被授予“广州市优秀科普使者”称号。

特发此证，以资鼓励。

广州市科技创新委员会 共青团广州市委员会

二〇一七年四月二十八日

3.教学论文

混合式教学法在电路教学实践中的应用探索

黄 涌，向 丹，王晓军，庄 权，程俊棠
（广东技术师范大学 工业中心，广东，广州 510665）

摘 要：电路是自动化、电子信息等本科教学中的重要基础课程，从教学反馈来看，教师与学生均认为该课程难度较大，学生不易掌握其理论知识与实际应用．在教学实践中，运用将基础知识深入浅出、复杂物理问题简单化解析的教学理念，通过梳理电路所要求的各章节内容，将其分解成必须掌握的数学工具和物理基础知识，学生掌握必要的基础知识后再结合多媒体教学、仿真软件、板书推导等混合式辅助教学方法，可增强学生对于该课程学习的信心和兴趣，提升学习效果．

关键词：电路；学习兴趣；仿真软件
中图分类号：G642.0 **文献标识码：**A **文章编号：**2096-7764（2020）03-0078-05
DOI:10.13408/j.cnki.gjsxb.2020.03.013

0 引言

电路课程是自动化、电子信息等本科教学中的重要基础课程，为电子与电气类专业课程学习准备了必要的电学基础知识[1]．在教学发展过程中，培养学生创新意识的项目式教学方法[2-3]、MOOC等互联网+新教学手段相继得到应用，取得了良好的效果．但目前在教学活动中，仍主要采用教师为中心，教纲为主线的传统教学模式，因此，在教学活动中如何贯彻以学生为中心的教学理念，运用灵活多变的教学方法[4-5]，实现学生掌握理论知识和实际应用的目的，成为电路教学亟待解决的问题[6-7]．

本文从授课教师和学生两方面出发，对如何解决电路课程教学与学习中存在的问题进行了理论分析和实际举例．本文还运用从繁化简，深入浅出的教学理念，提出了该课程的混合式教学方法新模式，为教学提供参考．

1 电路课程特点及“教”与“学”现状分析

从电路（本文以邱关源《电路》第五版为例）课程的主干内容来看，它包括了电路的基础定理、元件特性和基本分析方法，具体来说，可分为电阻电路的一般分析方法、电路定理，含有电容、电感电路的暂态过程、正弦稳态和非正弦周期电路、动态电路复频域分析等．以电路知识运用为基础的后续专业课程包括模拟电路、数字电路，信号与系统、电力电子技术等课程等．因此，电路是工科学生必须掌握的基础工程学科．

教师在学生的学习过程中发挥着重要的引导作用，教师的教学理念、教学方法和教学手段对完成课程的学习任务提供了保障．从教学反馈情况来看，主要有两方面，一是由于课程知识量大，理论性强，课堂教学任务重，课堂主要用于对公式推导，例题、习题的快速讲解，缺乏

收稿日期：2020-03-09
基金项目：广东省教学团队项目（电路与电子基础课程群教学团队）；广东省研究生教育创新计划项目：凸显区域特色的机械类卓越中职教师“校企校”协同创新培养模式的构建与实践；广州市工业机器人智能驱控技术及部件重点实验室项目(201805010001)；广东省科技计划项目(2016B090927009)，2016B090927002.
作者简介：黄 涌，博士，广东技术师范大学讲师．

时间对于该课程知识分解，将内容形象化、具体化，以及学习方法、技巧的引导等；二是部分学生对于必要的基础知识掌握程度差，在学习过程中电路分析能力较弱，影响教学活动的开展及教学质量.

学生是课程学习的主体，学生的基础知识、学习方法、兴趣和信心是影响学习效果的重要因素[8]. 学生集中反映了学习中存在两方面问题：一是学习过程中需要大量高等数学、复变函数等数学工具和电学基础知识，知识面宽而且理论性强，学习难度大；二是学习过程中，认为正弦稳态电路及频率响应、动态电路复频域分析等章节内容过于抽象，推导过程复杂，不了解这些知识点的学习目的与实际应用意义，因此缺乏学习信心和兴趣，学习效果较差，甚至对该课程的学习形成恶性循环，影响整个专业课程的学习.

2　电路理论教学方法讨论

2.1　着眼整体，对知识结构进行深度解析，教学实践中对基础知识进行精细化准备

电路课程在研究抽象电路时，运用的概念、公式以及数学工具、推理过程都较多，因此，对电路的基础知识进行数学工具和电学知识的深度解析显得尤为重要. 图1所示为电路1-14章学习的主要内容以及需要的数学工具和电学基础知识对应关系简图（第六章放大电路在模拟电子技术或电工电子技术课程中讲解，电路课程中不作要求）. 电路课程分为两大部分，第一部分为包含纯电阻电路、独立电源和受控电源的电路模型以及电容、电感元件的基本特性；第二部分为包含电路基本元件的电路正弦交流、非正弦周期电流电路分析及线性电路复频域分析等. 在第一部分章节中，需要掌握的电学基础知识包括简单电路的认识、纯电阻欧姆定律、串并联电路的电学特性，数学工具主要包括多元一次方程组和一阶、二阶线性微分方程求解. 第二部分章节中，需要掌握的电学基础知识包括电容、电感元件的阻抗和欧姆定律的相量形式，数学工具包括三角函数公式中特别是积化和差、和差化积公式等内容，相量法在复平面中的表示，典型的积分公式，非正弦周期函数傅里叶变换和拉普拉斯变换等. 在这部分学习中，还需要运用第一部分所介绍的KCL、KVL定理，四种一般电路的分析方法，分别是支路电流法、网孔电流法、回路电流法和节点电压法，五个基本电路定理，分别是叠加定理、替代定理、戴维宁定理、诺顿定理和最大功率传输定理. 通过梳理知识结构可知，以我校开设电路课程的专业为例（理论课84学时或48学时），涵盖自动化学院、电子与信息学院、机电学院、光电学院等4个学院15个专业，从这些专业学生的高等数学和物理电学基础来看，均具备学习电路所需的基础知识.

以该知识结构梳理为基础，在具体章节的讲授过程中，采用复杂物理问题简单化的思路，分解电学知识和数据工具的方法进行实际应用，不仅能将重难点清晰有效地讲授，同时可有效消除学生畏难心理，取得良好的教学效果. 如非正弦周期电流电路计算应用举例中，根据给定的电路元件参数、电路图和矩形波电压的傅里叶展开式求解电流表达式和功率. 由于本章需要应用非正弦周期函数的傅里叶级数变换，对于非数学专业学生而言，傅里叶级数变换属难点内容，再结合电学知识，难度进一步提升. 但本章内容在讲授的过程中，如能将本节所需要的数学工具和电学基础知识进行分解并做

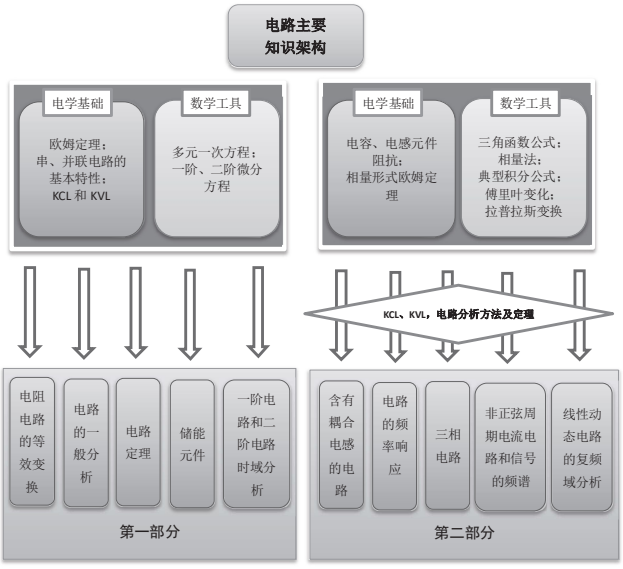

图1　电路1-14章学习的主要内容以及需要的数学工具和电学基础知识对应关系简图

好知识预备，可实现复杂问题简单化. 具体做法是，在本例题中，教学前数学工具准备包括非正弦周期函数傅里叶级数展开式的基本形式与参数含义，注重结论的识记与应用而非数学过程推导，电学知识准备包括LC电路各元件阻抗与欧姆定律的相量形式等. 分解完成后，对于非正弦周期电流电路的求解只需要按照基本步骤进行计算就可完成电路的分析. 因此，在难度较大的章节讲解过程中，将电学知识和数学工具分解开来进行运用，可有效提高学生学习的效果，帮助学生树立学好该课程的信心.

2.2 摸清讲授内容的要点和难点，强化关键步骤推导和演算过程

目前各高校普遍采用多媒体教学，在课堂上有较好的呈现效果，能将图片、视频甚至动画效果能带入课堂，互联网+手段还能更好地实时互动，形成良好的师生沟通互动的平台，起到了充分调节课堂气氛的作用. 但如何在改善学习氛围的同时提升学生分析问题的能力仍值得探讨. 实践证明，教师摸清讲授内容的要点和难点，采用传统的板书方法将关键步骤推导和演算过程展示出来，在部分章节讲授过程中仍发挥着不可替代作用. 这是由于在教学过程中，电路教学的核心内容仍是对物理模型的熟练分析和运用，教学形式的选择始终要以提升学生的知识运用能力为目的.

以教材例14-9为例，应用拉氏变换求解电路(图2所示)，已知电路原处于稳态，t=0时开关S闭合，用运算法求解换路后的电流i_L. 若采用教材中列出的求解过程直接讲解，根据回路电流法列出I_a和I_b的方程组，求出I_a和I_b后进行反拉氏变换，可得出电流i_L的时域表达式；该求解过程能将主要步骤展示并完成例题讲解，但学生对于该部分内容实际掌握效果不佳，若能结合板书推导展示求解过程，特别是重点要求学生掌握的数学运算方法，在推算过程中加以强调，教学效果能得到较大改善. 这是因为本题求解关键步骤除根据回路电流方程列出方程组和应用共轭复根的求解以外，还要熟练运用和理解多元方程组求解、洛必达法则、欧拉公式、复数的计算及三角函数公式等数学工具，同时，还要理解电容、电感的运算阻抗和附加电源等

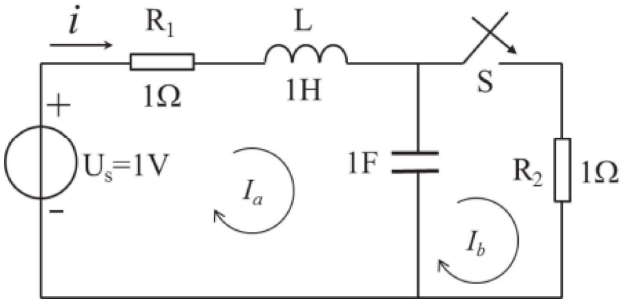

图 2 应用拉氏变换分析线性电路

物理知识，才能求解出正确答案，对学生提出了较高的要求. 在第十四章线性动态电路的复频域分析教学过程中，先将拉氏变换和反拉氏变换的数学部分知识熟练运用后，再对大纲要求知识点进行板书推导和演算，学生可以充分理解本章的重难点，使本章的学习效果得到有效提升.

2.3 采用虚拟教学软件，将抽象电路具体化，理论推导数据化

在电路教学中学生不仅要掌握大纲要求的知识点，同时还要形成电子工程类课程的思维方法，处理实际问题的能力，对教师提出了较高的要求. 实践证明，妥善处理多样化的教学方式与核心任务，形成多种教学手段的配合来提升学生学习效果的目的是达到教师教学要求的重要途径之一. 由于电路课程通常安排在本科教学的低年级阶段，此时，学生普遍未接触与实际应用相关的课程，对于抽象电路中分析正弦电流、电压特性等缺乏直观体验，并不能深刻理解其内容. 大纲要求的实验虽能辅助学生对于实际应用的理解，但由于在众多高校的电路教学中，课程安排或实验条件实际上无法完全与理论课程同步，如常见模式为理论课一般在1-16周开设，实验课则集中在4-8周完成，由于实验室要在全校进行不同专业和班级轮换以完成全部实验教学任务，通常会导致理论学习与实验脱节，影响学习效果. 因此，理论教学过程中，若采用电子电路仿真软件如Multisim软件进行电路图的验证探索、半设计调试或全设计调试应用可有效辅助学生理解教材中的电路.

以第十一章电路频率响应习题11-5为例，如图3(a)所示，已知R、L和电压源相关特性，需

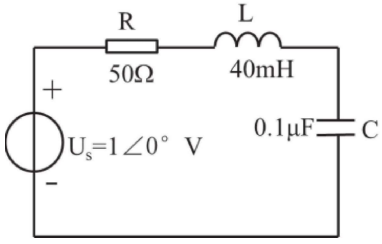

(a)

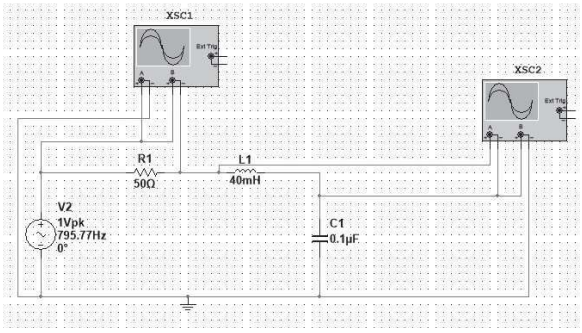

(b)

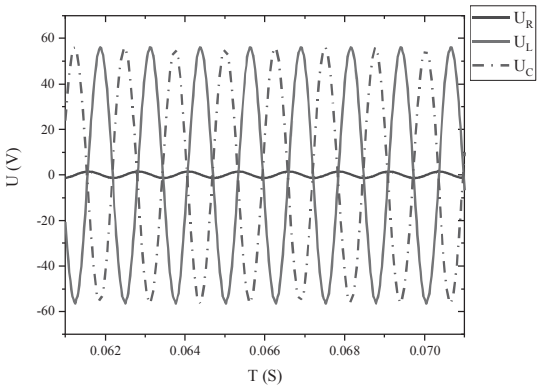

(c)

图 3　Multisim 软件模拟 RLC 串联谐振电路的计算
(a) 电路图 (b)Multisim 设计效果图
(c) 输入谐振频率正弦电压时各元件电压波形图

对谐振频率、电容参数、各元件的电压之间的关系进行分析. 本题讲解过程中，利用谐振频率公式 $\omega_0 = 1/\sqrt{LC}$ 以及品质因素 $Q = \omega_0 L/R$ 求得相关结果，运算过程并不复杂，但学生的认知只能停留在理论推导阶段. 若利用 Mulitism 软件将电路图进行设计和虚拟实验，如图 3(b) 所示，对电路加载谐振频率正弦电压，可得到 R、L、C 各元件电压的瞬时值、相位关系等，如图 3(c) 所示. 该内容的教学就实现了由理论计算向直观展示的转变，同时也展示出了 RLC 电路中电容电感元件的电压值有效值远大于输入电压有效值的特性. 如需进一步了解谐振频率、品质因素之间关系，本题还可以延伸，如输入两倍谐振频率正弦电压时各元件电压波形图，电路各元件与输入电源关系也可以用同样方法进行模拟，将电路的抽象理论计算与实际应用较好地结合起来.

因此，将课程中的电路通过软件进行虚拟实验，可直观地展示各元件的响应情况，实现将抽象电路具体化，理论推导数据化，亦能进行应用拓展，激发学生学习兴趣，加深对所学内容的理解.

3　总结

由于电路学习通常为大一下学期和大二上学期完成，周期长，内容抽象，在实际教学过程中，部分学生认为前面基础章节掌握不好后续复杂内容学不好是理所当然，自信心受挫折. 但通过梳理电路课程的知识编排发现事实并非如此，章节之间的内容虽有联系，但又相对独立. 从图 1 知识结构图中也可以看出，第十三、十四章与第十章至第十二章的内容联系较小，通过鼓励学生树立自信心，可实现对于难度较大的非正弦周期电路分析与复频域分析掌握程度与基础章节掌握程度相当. 因此在教学过程中需要将知识结构梳理清楚，分阶段鼓励学生在学习过程中善始善终，在学习过程中只要多一份努力，就会多一份收获和回报，最终达到提升学习效果的目的.

总之，电路作为一门基础课程，具备其自身的特点，在教学准备过程中，应注重高屋建瓴，整体把握教材，将复杂物理问题简单化，通过梳理电路所要求的各章节内容，将其分解成必须掌握的数学工具和电学基础知识；在教学实践中，以基础为重，平衡多媒体教学、仿真软件、板书推导等多种方式辅助教学，把教学内容中的抽象理论模型变得生动、具体化，培养不同专业学生对于学习电路的信心和兴趣，就能通过该课程培养学生分析问题和解决问题的能力，为实际应用和进一步的理论学习做好知识储备.

参考文献：

[1] 付立军 . 电路原理全英文混合式教学模式研究与实施 —— 以大连民族大学为例 [J]. 大连民族大学学

报 ,2019,21(06):564-567.
[2] 张伟 , 韩素敏 , 谢东垒 . 电路课程项目式驱动教学模式探索 [J]. 教育教学论坛 ,2019(49):105-106.
[3] 华成英 , 王红 , 叶朝辉 . 电子技术基础课程研究型教学模式的探索与实践 [J]. 北华航天工业学院学报 ,2011,21(04):41-43.
[4] 朱广 , 姬敬 , 龚雪 , 张润梅 , 赵汝海 , 程秀芝 . 混合式教学在高校电路原理教学中的应用探索 [J]. 成才之路 ,2019(36):12-13.
[5] 王二萍 , 乐丽琴 , 蔡艳艳 , 张洋洋 , 张金平 .《电路分析及应用》创新教材建设探索 [J]. 当代教育实践与教学研究 ,2017(12):203.
[6] 殷惠莉 , 薛秀云 , 宋淑然 . 电路课程建设与教学改革探索 [J]. 教育教学论坛 ,2019(33):120-121.
[7] 刘小群 . 创新型人才培养背景下电子类专业实践教学改革研究 [J]. 西部素质教育 ,2018,4(24):126-127.
[8] 叶朝辉 , 华成英 . 关于提高《模拟电子技术基础》学习兴趣的研讨 [A]. 全国电子技术研究会 . 全国电子技术研究会 2005 年会论文集 [C]. 全国电子技术研究会 : 华北航天工业学院学报编辑部 ,2005:3.

[责任编辑 : 刘向红]

Research on the Application of Blended Teaching in *Electric Circuit* Teaching Practice

HUANGY Yong, XIANG Dan, WANG Xiao-jun, ZHUANG Quan, CHENG Jun-tang
(Guangdong Polytechnic Normal University, Guangzhou Guangdong 510665)

Abstract: *Electric Circuit* is an important basic course for undergraduate majors such as automation, electronic information and so on. Both teachers and students believe that the course is difficult, and students have difficulties in mastering its theoretical contents and practical skills. In the teaching practice, by analyzing the basic knowledge and complex physical problems, the contents of each chapter required by the circuit are integrated and decomposed into the necessary mathematical tools and basic physical knowledge that must be mastered. After students master the necessary basic knowledge, blended teaching is applied by using multimedia teaching, simulation software, blackboard derivation in the classroom teaching. It is proved this teaching method can enhance students' confidence and interest in learning as well as their learning effect.

Key words: *Electric Circuit*; interest in learning; simulation software

(上接第 72 页)

Fundamentals of Industrial Robot Technology Curriculum Development Based on Work Process in Secondary Vocational Schools

XU Lan-ying[1], MAO Shi-jie[1], HE Bao-lan[1], ZHAO Peng[1], WU Qiang[2]
(1. School of Mechatronic, Guangdong Polytechnic Normal University, Guangzhou Guangdong 510665; 2. School of Automobile and Transportation Engineering, Guangdong Polytechnic Normal University, Guangzhou Guangdong 510665)

Abstract: To produce the market suitable talents, the present study proposes a curriculum development approach based on work process for the specialty of Industrial Robot, to be specific, for the course of *Fundamentals of Industrial Robot Technology*. The practice is achieved through the in-depth survey with enterprises and secondary vocational schools, which results in defining typical work tasks and the teaching design based on work process by analyzing inductive action areas in these work tasks, the conversion of the learning areas, the design of visual learning context. The defined course goals, the process of the course development and the teaching evaluation are all revealed in this study to provide practical experiences for the curriculum development in related field.

Key words: work process; industrial robot; curriculum development

基于 RC 电路频率响应特性在教学中的研究

黄涌　杨瑶　蔡秋荧　向丹
（广东技术师范大学　广东省广州市　510665）

摘　要：本文通过研究 RC 电路的特性，利用虚拟仿真软件将抽象内容具体化，让学生正确理解电路频率特性中的基本概念，并能结合实际需要进行灵活运用，达到降低学习难度，并熟练掌握该部分内容的目的。

关键词：网络函数；频率响应；仿真软件

电路频率响应研究的 RC 电路在实际应用中较为广泛，如通信、自动控制系统以及测量仪器系统等，因此该类电路的特性研究是电路教学中的重要内容。在频率响应的教学过程中，网络函数、频率特性等均利用概念介绍、公式推导等方式进行阐述，内容较为抽象且不易理解。从教学目标来看，本章节内容对学习目标提出了较高的要求，不仅要求理解网络函数、频率响应等基本概念，还要求灵活分析电路频率响应特性，对 RC 串并联电路的特性、品质因素等进行运用和计算，学生普遍反映该部分内容学习难度大 [1]。通过调查发现，学生对于该部分理解的难度主要存在有两点，第一是对网络函数的概念是公式化的理解，应用场景缺乏直观感受，第二是电路的频率响应特性变化过程过于抽象。因此，如何通过图形化的方式，结合实际应用对电路频率响应特性的讲解，是电路课程在该章节的教学中要着力解决的问题。

实际应用举例教学过程中，教师引入与本章基础知识和重点内容相关联的例子，引导学生积极思考，特别是将学习到的基本概念和理论在实际例子中运用，这样学生不仅能深刻理解学习本章的作用和目的，又能体验到学以致用的乐趣。本章节教学过程中，以较为简单的 RC 振荡电路为基础，借助 Multisim 仿真软件 [2-5]，对电路的输入输出特性、实际应用等情况进行虚拟仿真，并通过电路参

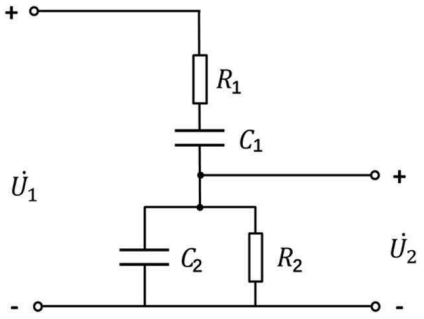

图 1：RC 串并联选频网络结构图

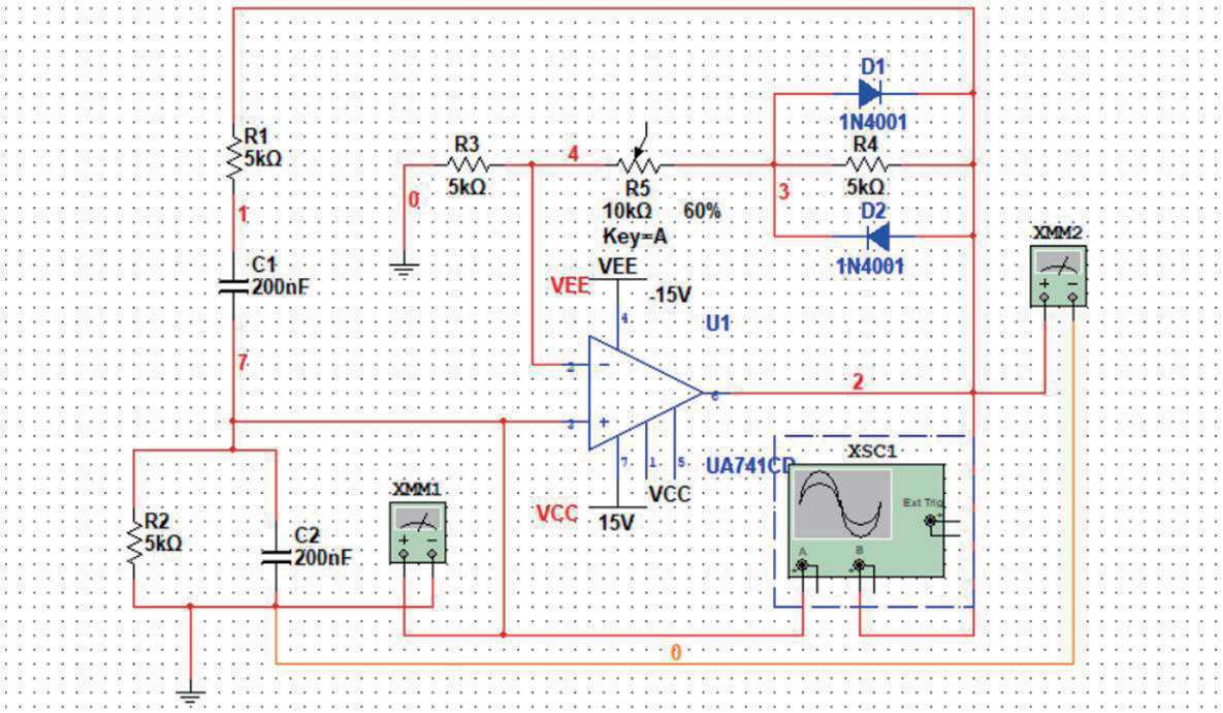

图 2：RC 正弦振荡电路结构示意图

●基金资助：广东省教学团队项目（电路与电子基础课程群教学团队）；广东省研究生教育创新计划项目：凸显区域特色的机械类卓越中职教师“校企校”协同创新培养模式的构建与实践；广州市工业机器人智能驱控技术及部件重点实验室项目（201805010001）。

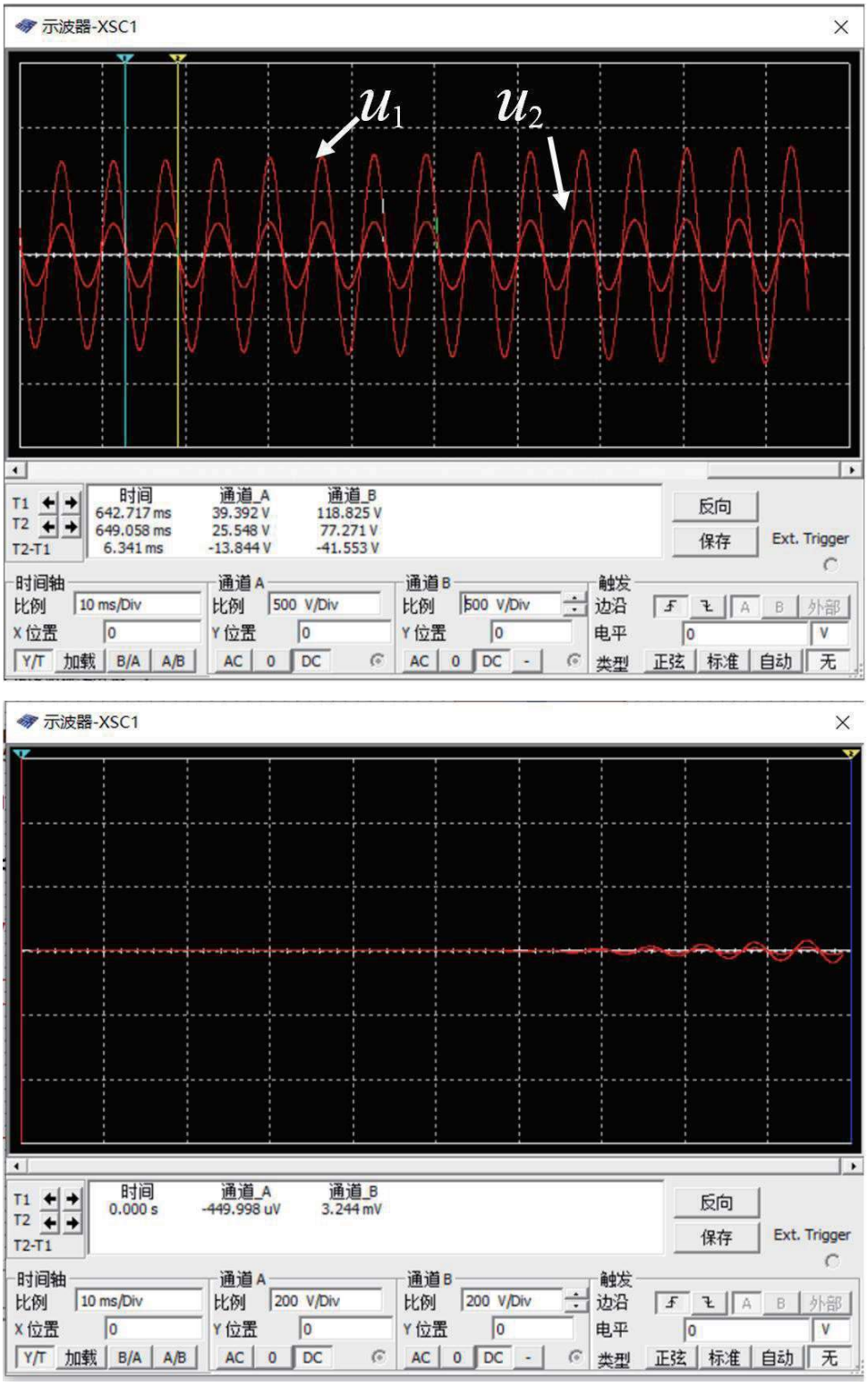

图 3：正弦波振荡电路起振和稳幅过程

数的变化，优化电路的输出特性，达到掌握基本概念和熟练运用知识的目的。

1 RC正弦波振荡电路频率响应特性计算

RC 正弦波振荡电路可以将直流能量转换为交流能量，在中低频信号时得到广泛应用。它是由放大电路、RC 串并联正反馈选频网络、稳幅环节四个部分组成，其选频部分的结构如图 1 所示。

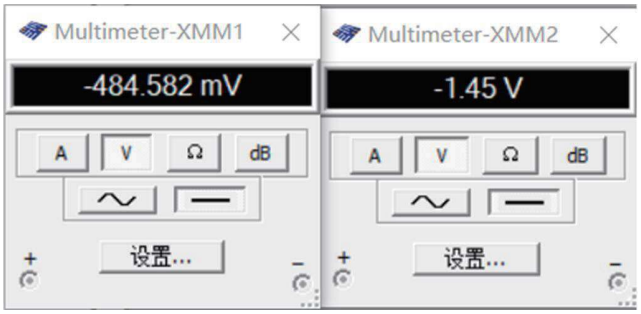

图 4：RC 正弦波振荡电路稳幅时输入电压（左）和输出电压（右）的数值

RC 串并联选频网络的频率特性为：$\omega_0=\frac{1}{\sqrt{R_1R_2C_1C_2}}$

其谐振频率：$f_0=\frac{\omega_0}{2\pi}=\frac{1}{2\pi\sqrt{R_1R_2C_1C_2}}$

利用电压网络函数：

$$F=\frac{\dot{U}_2}{\dot{U}_1}=\frac{R_2//\frac{1}{j\omega C_2}}{R_1+\frac{1}{j\omega C_2}+R_2//\frac{1}{j\omega C_2}}=\frac{1}{1+\frac{R_1}{R_2}+\frac{C_1}{C_2}+j\sqrt{\frac{R_1C_2}{R_2C_1}}\left(\frac{f}{f_0}-\frac{f_0}{f}\right)}$$

可得到输入输出的幅频和相频特性：

$$\left|\vec{F}\right|=\frac{1}{\sqrt{\left(1+\frac{R_1}{R_2}+\frac{C_2}{C_1}\right)^2+\frac{R_1C_2}{R_2C_1}\left(\frac{f}{f_0}-\frac{f_0}{f}\right)^2}}\quad \varphi=-\arctan\frac{\sqrt{\frac{R_1C_2}{R_2C_1}}\left(\frac{f}{f_0}-\frac{f_0}{f}\right)}{\left(1+\frac{R_1}{R_2}+\frac{C_2}{C_1}\right)}$$

2 RC正弦波振荡电路仿真实验

图 2 所示的电路是由 Multisim 软件创建的 RC 正弦波振荡电路，放大电路是由集成放大器 741 与三个电阻 R_3、R_4、R_5 以及由两个二极管 D_1、D_2 组成的负反馈网络构成的；二极管 D_1、D_2 为电路的稳幅环节；两个电阻 R_1、R_2 以及两个电容 C_1、C_2 组成 RC 串并联正反馈选频网络。电路中的双踪示波器 XSC1 用来观测输入电压 u_1 和输出电压 u_0 的波形，数字万用表 XMM1 用来测量输入电压 u_1 的数值，万用表 XMM2 是用来测量输出电压 u_0 的数值。

RC 串并联网络在电路中充当两种网络，一种是正反馈网络，另一种是选频网络，当电路中的电阻和电容满足 $R_1=R_2=R=5K\Omega$、$C_1=C_2=C=200nF$ 时，电路的振荡频率 f_0 为：

$$f_0=\frac{1}{2\pi RC}$$

由图 2 所示的电路选取的电容值和电阻值，就可以计算出电路的振荡频率 f_0 为：

$$f_0=\frac{1}{2\pi RC}=\frac{1}{2\pi\times5\times10^3\times200\times10^{-9}}=159.235Hz$$

设定 R_5=60%×10KΩ，按下仿真开关的按钮进行电路的仿真测量，从双踪示波器就可以观测出电路的输出电压 u_0 和输入电压 u_1 的幅值以及电路中从起振到稳幅的振荡波形，如图 3 所示，其中幅度较大的是输出电压 u_0 的波形，幅度较小的是输入电压 u_1 的波形，并且可以从中看出，输出电压 u_0 和输入电压 u_1 同相位。图 4 所示的是电路稳幅输出时，用数字万用表测量的输出电压 u_0 和输入电压 u_1 的数值。

由图 4 的测量值并且考虑输出电压 u_0 和输入电压 u_1 同相位，可以计算出来稳幅后电路的电压放大倍数和反馈系数是：

$$\vec{A}=\frac{\overrightarrow{U_0}}{\overrightarrow{U_1}}=\frac{1450}{484.582}=3\ 和\ \vec{F}=\frac{\overrightarrow{U_1}}{\overrightarrow{U_2}}=\frac{484.582}{1450}=\frac{1}{3}$$

从上面的计算结果表明，仿真所计算的结果与理论值相等。通过仿真实验，可以看出当电路不满足起振条件时，无论电路是否具有稳幅环节，都无法实现自激振荡，即电路是不能起振的；如果电路满足起振条件，没有稳幅环节的电路可以起振，并产生波形，原因是电路利用电路中的正反馈而形成的自激起振，其输出幅度会变得越来越大，最终导致运算放大器输出达到饱和，形成失真，在这种情况下，电路是不能自动进入到正弦振荡状态；而有稳幅环节的电路既可以正常起振，也能够输出稳定且标准的正弦波。由此可以得出具有稳幅环节的 RC 正弦波振荡电路才是一个完善的 RC 正弦波振荡电路。

3 小结

在电路教学中，网络函数是难点，通过对电路主要参数以及实验仿真的方法，让学生理解网络函数意义在于能从不同“窗口”，例如电路的结构，参数值，输入、输出变量以及端口对的相互位置来分析研究网络的频率特性，可以从不同角度寻找电路比较优越的频率特性和电路工作的最佳频率范围。借助 Multisim 仿真软件应用对电路频率响应特性图像化，使讲解 RC 电路的电路频率特性更直观易懂。

参考文献

[1] 李新.RC 桥式正弦波振荡电路探析 [J]. 科技创新与应用，2014(20):94-94.
[2] 马敬敏．基于 Multisim 10 的 RC 桥式正弦波振荡电路仿真分析 [J]. 渤海大学学报（自然科学版），2012(04):324-328.
[3] 胡兰芳．基于 Multisim 11 的 RC 桥式振荡电路研究 [J]. 成都师范学院学报，2015,31(05):116-120.
[4] 艾宝，艾永乐．基于 Multisim 的 RC 文氏振荡电路探讨 [J]. 北京电子科技学院学报，2007.
[5] 张静，王瑜．基于 Multisim12 的 RC 正弦波振荡器的仿真及分析 [J]. 绥化学院学报，2017,37(02):151-154.

作者简介

黄涌（1981-），男，湖南省湘潭市人。讲师，博士研究生。研究方向为电子技术。
杨瑶（2002-），女，广东省汕头市人。大学本科学历。研究方向为测控技术与仪器。
蔡秋荧（2001-），女，广东省清远市人。大学本科学历。研究方向为测控技术与仪器。
向丹（1980-），女，湖北省宜昌市人。博士研究生，教授。研究方向为自动控制。

4.科研项目

附件1

2019年广东省普通高校特色创新类项目（本科）

1.自然科学类				
序号	项目编号	项目名称	负责人姓名	所属学校
1	2019KTSCX001	隧道工程智慧建造技术及其应用研究	周建春	华南理工大学
2	2019KTSCX002	镉-多溴联苯醚复合污染的植物效应研究	梁钰贞	华南理工大学
3	2019KTSCX003	产线/仓储环境中的智能AGV自主导航及应用示范	全思博	华南理工大学
4	2019KTSCX004	智能多液相酶拆分体系制备高纯度手性药物研究	李志刚	华南理工大学
5	2019KTSCX005	再生制动条件下地铁列车节能操纵的鲁棒优化技术研究	郑亚晶	华南理工大学
6	2019KTSCX006	温和体系中工业木质素定向解聚制备芳香类平台化合物	侯轶	华南理工大学
7	2019KTSCX007	粤港澳大湾区交通枢纽客流安全智能监测、预警与协同管控研究	黄玲	华南理工大学
8	2019KTSCX008	MaaS背景下基于用户选择行为的公交网络协同调度优化设计研究`	巫威眺	华南理工大学
9	2019KTSCX009	特异性LncRNAs协同调控MIF导致新发糖尿病相关胰腺癌发病的分子机制研究	王迎雪	暨南大学
10	2019KTSCX010	分布式知识的统一插值及在分布式系统中的应用	方良达	暨南大学
11	2019KTSCX011	重组人胶原蛋白医用植入原料的研究开发	项琪	暨南大学
12	2019KTSCX012	电化学催化产氧解决肿瘤乏氧问题	马丽	暨南大学
13	2019KTSCX013	基于大数据和人工智能的空地一体化荔枝龙眼生长精准管控关键技术研究与应用示范	谢家兴	华南农业大学

77	2019KTSCX079	有氧运动调控IRS-1信号通路改善非酒精性脂肪肝的分子机制研究	于洋	广州体育学院
78	2019KTSCX080	田径专项功能性体能训练方法学体系与专项器材研制的创新研究	袁运平	广州体育学院
79	2019KTSCX081	低温环境下运动和限制能量摄入改善肥胖大鼠脂代谢及调节ANGPTLs效应研究	翁锡全	广州体育学院
80	2019KTSCX082	运动对自闭症大鼠微生物-肠-脑轴影响的血清素机制研究	侯晓晖	广州体育学院
81	2019KTSCX083	基于复系数金兹堡-朗道方程的涡旋光孤子传输及调控研究	仇云利	广东技术师范大学
82	2019KTSCX084	可见光通信器件载流子与频率响应及光效特性机理的研究	黄涌	广东技术师范大学
83	2019KTSCX085	骨组织工程用Mg颗粒强韧化nHA复合材料微波烧结组织与性能研究	刘一雄	广东技术师范大学
84	2019KTSCX086	基于深度随机森林的转子故障多源信息融合智能诊断方法研究	陈飞昕	广东技术师范大学
85	2019KTSCX087	基于超材料的光子晶体拓扑特性及其拓扑界面态研究	邓寒英	广东技术师范大学
86	2019KTSCX088	一类经济模型的动力学分析	钟吉玉	岭南师范学院
87	2019KTSCX089	基于GRU-CNN深度学习的半监督叠前密度反演方法研究	梁立锋	岭南师范学院
88	2019KTSCX090	球形核壳复合吸波材料的微结构设计、可控合成及其性能调控与机理研究	田春华	岭南师范学院
89	2019KTSCX091	新型近红外生物质碳量子点生物传感器的制备及其在肿瘤细胞pH检测与比率荧光成像的应用研究	薛茗月	岭南师范学院
90	2019KTSCX092	图与超图优化指标研究	于广龙	岭南师范学院
91	2019KTSCX093	钒酸锌基Z-型光催化体系理性构建及界面调控机制研究	罗金	岭南师范学院
92	2019KTSCX094	基于粗糙集的高光谱特征波段选择方法研究及其在贝类重金属无损检测中的应用	刘瑶	岭南师范学院

受理编号：c163171900010

项目编号：2016A070714004

文件编号：粤科规财字〔2016〕48号

2016A070714004

广东省省级科技计划项目

合同书

项目名称：增材制造（3D打印）科技创新创业人才培训服务体系建设

计划类别：科技创新创业人才服务领域

项目起止时间：2016-01-01　至　2017-12-31

管理单位(甲方)：广东省科学技术厅

承担单位(乙方)：广州市光机电技术研究院

乙方主管部门(丙方)：广州市科技创新委员会

通讯地址：广东省广州市萝岗区广州高新技术产业开发区科学城科研路3号

邮政编码：510663　　单位电话：020-32068940

项目负责人：黄涌　　联系电话：020-32290283

项目联系人：黄逸　　联系电话：020-32068940

广东省科学技术厅

二〇一四年制

一、项目实施内容

1.主要内容：

本项目将以3D专业技术、创新方法、人才培养模式、创业服务咨询等为主要内容，对3D打印技术创新创业人才进行培训服务，并完成3D打印创新创业人才服务体系的建设。

2.拟解决的关键问题及技术路线

本项目将通过建设3D打印技术创新创业人才培训服务体系，为企业提供3D打印技术人才培养平台、科技交流平台、创业服务咨询平台，为省重大专项和重点支持方向提供技术咨询与人才培养服务，提供新兴产业人才培养新模式。

3.创新点

本项目将结合3D打印技术、创新创业以及人才培养模式等作为主要内容，逐步形成资源丰富、特色鲜明、管理规范、成效显著的专业创新人才培训服务体系。

（1）新技术

本项目的专业方向是3D打印技术，该技术是我省重点支持的战略新兴产业，列入了重点支持项目。

（2）新结合

本项目以3D打印的专业技术与创新方法相结合，突出使用系统理论指导创新创业人才在3D打印技术科研和产业发展过程中进行创新活动。

（3）新模式

坚持以面向3D打印专业创新创业人才、传授实用知识、服务区域行业发展、发挥自身优势、培养复合型高端人才为指导思想，强化申报单位作为人才培养平台和技术交流平台的作用，提高创新创业人才的培养水平，充分利用省内地区高校、科研院所和企业的教学资源和应用环境，结合3D打印产业发展的实际情况，构建区域人才培养新模式，营造创新创业技术人才通过专业技术的创新方法培训学习提高创新和研发的效率，为企业创造更大效益，同时企业积极鼓励专业技术人员学习创新的良好氛围。

二、项目考核指标

<table>
<tr><td colspan="6">1.项目完成后提供的研究开发成果及形式（须明确产品、专利、版权、标准等成果的类型及数量）</td></tr>
<tr><td colspan="2">成果形式</td><td>成果数量</td><td colspan="2">成果形式</td><td>成果数量</td></tr>
<tr><td rowspan="2">发明专利</td><td>申请</td><td></td><td colspan="2">引进人才(人)</td><td></td></tr>
<tr><td>授权</td><td></td><td colspan="2">培养人才(人)</td><td>100</td></tr>
<tr><td rowspan="2">实用新型专利</td><td>申请</td><td></td><td colspan="2">科技人才奖励(人)</td><td></td></tr>
<tr><td>授权</td><td></td><td rowspan="2">技术标准制定</td><td>牵头(个)</td><td></td></tr>
<tr><td rowspan="2">外观设计专利</td><td>申请</td><td></td><td>参与(个)</td><td></td></tr>
<tr><td>授权</td><td></td><td colspan="2">科技报告(篇)</td><td></td></tr>
<tr><td rowspan="2">国外专利</td><td>PCT受理</td><td></td><td colspan="2">软件著作权(项)</td><td></td></tr>
<tr><td>授权</td><td></td><td colspan="2">论文论著(篇)</td><td></td></tr>
<tr><td colspan="2">获得国家级奖项(项)</td><td></td><td rowspan="3">其中：被收录论文数(篇)</td><td>SCI</td><td></td></tr>
<tr><td colspan="2">获得省级奖项(项)</td><td></td><td>EI</td><td></td></tr>
<tr><td colspan="2">新服务(项)</td><td></td><td>ISTP</td><td></td></tr>
<tr><td colspan="2">新产品（或新材料、新装备、新品种（系））</td><td></td><td colspan="2">新工艺（或新方法、新模式、新技术）</td><td></td></tr>
<tr><td colspan="2" rowspan="2">创新载体项目必填</td><td colspan="3">技术服务数量（项）</td><td></td></tr>
<tr><td colspan="3">服务企业数量（家）</td><td></td></tr>
<tr><td colspan="2" rowspan="4">科技金融项目必填</td><td colspan="3">开展培训宣讲活动场次(次)</td><td></td></tr>
<tr><td colspan="3">服务企业数量(家)</td><td></td></tr>
<tr><td colspan="3">帮助企业融资(万元)</td><td></td></tr>
<tr><td colspan="3">引进专业机构(家)</td><td></td></tr>
<tr><td colspan="2" rowspan="4">院士工作站项目必填</td><td colspan="3">引进院士及其团队科技成果转化数量</td><td></td></tr>
<tr><td colspan="3">院士开展的战略咨询和技术指导次数</td><td></td></tr>
<tr><td colspan="3">院士年进站次数</td><td></td></tr>
<tr><td colspan="3">院士及院士团队年进站时间</td><td></td></tr>
<tr><td colspan="2" rowspan="8">软科学项目必填</td><td colspan="3">决策咨询报告(篇)(至少1篇)</td><td></td></tr>
<tr><td colspan="3">研究总报告(篇)(至少1篇)</td><td></td></tr>
<tr><td colspan="3">研究中期报告(篇)</td><td></td></tr>
<tr><td colspan="3">研究分报告(篇)</td><td></td></tr>
<tr><td colspan="3">调研报告(篇)</td><td></td></tr>
<tr><td colspan="3">专著(篇)[须注明“广东省软科学研究计划项目(项目编号：)资助”]</td><td></td></tr>
<tr><td colspan="3">核心期刊论文(篇)[以第一作者发表，须注明“广东省软科学研究计划项目(项目编号：)资助”]</td><td></td></tr>
<tr><td colspan="3">培养人才(人)</td><td></td></tr>
</table>

	获国家级奖项(项)	
	获省级奖项(项)	
	其他（具体形式：用户填）	
其他成果及形式说明：		
结合3D打印技术、创新创业及人才培养模式等，形成资源丰富、特色鲜明、管理规范、成效显著的人才培训服务体系。 1.新技术 专业方向是3D打印技术，该技术是我省重点支持的战略新兴产业。 2.新结合 3D打印技术与创新方法相结合，突出使用系统理论指导创新创业人才在研发过程中创新。 3.新模式 利用人才培养和技术交流平台，及高校、科研院所和企业的教学资源和应用环境，构建人才培养新模式。		
2.主要技术经济指标及社会效益		
累计新增销售收入（万元）		
累计新增利税（万元）		
其他主要技术经济指标及社会效益说明：		
项目将以3D打印创新创业人才培训为主题，建立有针对性的科技创业领军人才培训课程体系，每年开展2-3期特色鲜明的培训活动，每期组织不少于100人次参加，通过参与者在培训期间的个人学习成果、企业发展变化及导师意见等形成培训结业报告，完成3D打印技术创新创业人才培训服务体系建设，为我省3D打印技术行业发展培养一批创新能力强、团队结构优的高层次创新科技人才队伍，促进我省在增材制造技术及相关专业技术人才水平走向国际前列，加快产业转型升级步伐。		
项目负责人（签章）：　　年　　月　　日		

三、项目进度和阶段目标

开始日期	结束日期	主要工作内容
2016-01-01	2016-03-31	制定项目总体计划，确定培训内容及培养模式等；
2016-04-01	2016-12-31	开展第一阶段培训，完成2-3期3D打印和创新方法等主题的培训班，组织论坛交流活动等；
2017-01-01	2017-09-30	根据第一阶段培训反馈信息和经验总结，开展第二阶段培训，完成2-3期培训班或论坛交流活动，完善人才培训模式体系建设；
2017-10-01	2017-12-31	完成项目指标，项目总结，验收。

四、承担、参与单位工作分工及经费分配情况

承担/参与单位名称（盖章）	工作分工	总经费分摊（万元）	省科技厅经费分配（万元）
广州市光机电技术研究院	项目承担单位，负责项目计划制定，项目具体实施以及项目总结工作。 项目申报单位以3D打印创新创业人才培训为主题，建立有针对性的科技创业领军人才培训课程体系，每年开展2-3期特色鲜明的培训活动，每期组织不少于100人次参加，利用申报单位的科研平台、科技交流平台和3D产业联盟等平台，每年引进2-3名行业创新专家或其团队进行项目相关技术和人才培训服务，完善3D打印创新创业人才培训模式体系建设。	50.00	50.00
	合计	50.00	50.00

五、项目总经费及省科技厅经费预算

<table>
<tr><td colspan="6">1.省科技厅经费下达总额： （大写）伍拾万圆整；（小写 ）50.00万元；</td></tr>
<tr><td colspan="6">2.省科技厅经费拨付方式： 一次性拨款</td></tr>
<tr><td colspan="6">3.省科技厅经费年度下达计划：总额50.00(万元)</td></tr>
<tr><td colspan="3">分期</td><td colspan="3">经费(万元)</td></tr>
<tr><td colspan="3">第1期</td><td colspan="3">50</td></tr>
<tr><td colspan="6">4.总经费开支预算计划：</td></tr>
<tr><td colspan="5">经费筹集情况：</td><td>（单位：万元）</td></tr>
<tr><td colspan="6">总投入经费：50.00</td></tr>
<tr><td rowspan="2"></td><td rowspan="2">省科技厅经费</td><td colspan="3">自筹资金</td><td rowspan="2">合计</td></tr>
<tr><td>自有资金</td><td>贷款</td><td>地方政府投入</td><td>其它</td></tr>
<tr><td>已投入经费：</td><td></td><td></td><td></td><td></td><td></td><td></td></tr>
<tr><td>新增经费：</td><td>50.00</td><td></td><td></td><td></td><td></td><td>50.00</td></tr>
<tr><td>政府部门、境外资金及其他资金投入情况说明：</td><td colspan="5"></td></tr>
</table>

新增经费预算：				（单位：万元）
	新增经费总额		省科技厅经费	
支出经费	经费额	用途说明	经费额	用途说明
基建费：				
1、直接费用：	45.00		45.00	
(1)设备费：				
(2)材料费：				
(3)测试化验加工外协费：				
(4)燃料动力费：				
(5)差旅费：	5.00	服务团队、技术团队差旅费用	5.00	服务团队、技术团队差旅费用
(6)会议费：	5.00	科技服务团队参加会议费用	5.00	科技服务团队参加会议费用
(7)国际合作与交流费：	8.00	合作交流与培训费用	8.00	合作交流与培训费用
(8)出版/文献/信息传播/知识产权事务费：	4.00	培训相关资料制作、宣传等费用	4.00	培训相关资料制作、宣传等费用
(9)租赁费：	1.00	培训场地租赁费用	1.00	培训场地租赁费用
(10)人员费：	15.00	科技服务、技术服务团队人员费用	15.00	科技服务、技术服务团队人员费用
(11)专家咨询费：	5.00	培训专家费用	5.00	培训专家费用
(12)直接费用其他支出：	2.00	审计验收、资料费等	2.00	审计验收、资料费等
(13)科技金融服务体系其他费用：	0.00		0.00	
①信用评级补贴：				
②大赛场租：				
③特派员奖励与补贴：				
2、间接费用：	5.00		5.00	
管理与绩效费：	5.00	项目管理与绩效支出费用	5.00	项目管理与绩效支出费用
合计：	50.00		50.00	

六、人员信息

项目负责人情况								
姓名	**年龄**	**性别**	**职称**	**职务**	**学历**	**在项目中承担的任务**	**所在单位**	**签名**
黄涌	35	男	工程师	继续教育基地常务副主任	硕士研究生	项目总负责	广州市光机电技术研究院	

主要研究开发人员								
姓名	**年龄**	**性别**	**职称**	**职务**	**学历**	**在项目中承担的任务**	**所在单位**	**签名**
李健	30	男	助理工程师	继续教育基地副主任	本科	电子技术、方案策划与培训组织	广州市光机电技术研究院	
黄瑶瑶	29	女	助理工程师	技术干部	本科	宣传策划、培训组织	广州市光机电技术研究院	
陈宁	25	女	助理经济师	人秘部副部长	大专	培训管理	广州市光机电技术研究院	
朱倩	37	女	助理工程师	博管办主任	硕士研究生	培训管理	广州市光机电技术研究院	
冼云帆	31	女	经济师	计划供应部副部长	本科	培训管理	广州市光机电技术研究院	
赵博	37	男	高级工程师	副总工程师	博士研究生	3D打印技术支持	广州市光机电技术研究院	
李长春	34	男	工程师	技术干部	本科	3D打印技术支持	广州市光机电技术研究院	
苏文强	41	男	经济师	副主任	本科	培训组织	广州市光机电技术研究院	

戚晓燕	26	女	助理工程师	技术干部	本科	计算机软件技术支持	广州市光机电技术研究院	
肖瑶	26	女	助理工程师	技术干部	本科	自动化技术支持	广州市光机电技术研究院	
王小辉	52	男	高级工程师	副院长	硕士研究生	技术顾问、培训策划	广州市光机电技术研究院	

七、承担、参与单位合作协议（须与申报书中合作协议或意向书相一致）

无

八、合同条款

第一条 甲方与乙方根据《中华人民共和国合同法》及国家有关法规和规定，为顺利完成（2016）年**增材制造（3D打印）科技创新创业人才培训服务体系建设**专项项目（项目编号：**2016A070714004**）经协商一致，特订立本合同，作为甲乙双方在项目实施管理过程中共同遵守的依据。

第二条 甲方的权利义务：

1.按合同书规定进行经费核拨的有关工作协调。

2.根据甲方需要，在不影响乙方工作的前提下，定期或不定期对乙方项目的实施情况和经费使用情况进行检查或抽查。

3.根据《广东省科技计划项目信用管理办法(试行)》对乙方进行科技计划信用管理。

第三条 乙方的权利义务：

1.确保落实自筹经费及有关保障条件。

2.按合同书规定，对甲方核拨的经费实行专款专用，单独列账，并随时配合甲方进行监督检查。

3.使用财政资金采购设备、原材料等，按照《广东省实施〈中华人民共和国招标投标法〉办法》有关规定，符合招标条件的须进行招标。

4.项目实施完成或实施到一定程度，须按照《广东省省级科技计划项目结题管理的实施细则（试行）》提出验收或终止结题的申请，并按甲方要求做好项目结题工作。

5.在每年1月向甲方如实提交上年度工作情况报告，报告内容包含上年度项目进展情况、经费决算和取得的效果等。

6.按照国家和省有关规定，每年须提交年度科技报告；项目验收时，须提交验收科技报告。

第四条 在履行本合同的过程中，如出现广东省相关政策法规重大改变等不可抗力情况，甲方有权对所核拨经费的数量和时间进行相应调整。

第五条 在履行本合同过程中，需要对项目起止时间、项目经费使用（包括自筹经费、经费分配及经费支出预算等）、项目内容（包括研发内容、技术指标、经济指标及成果指标等）、项目名称、项目承担单位（包括承担单位更名、承担单位替换）、参与单位、项目负责人和成员等进行变更的，甲乙双方按照《广东省省级科技计划项目合同书管理的
实施细则（试行）》有关规定执行。

第六条 在履行本合同的过程中，当事人一方发现可能导致项目整体或部分失败的情形时，应及时通知另一方，并采取适当措施减少损失，没有及时通知并采取适当措施，致使损失扩大的，应当就扩大的损失承担责任。

第七条 本项目技术成果的归属、转让和实施技术成果所产生的经济利益的分享，除双方另有约定外，按国家和广东省有关法规执行。

第八条 属技术保密的项目，甲乙双方应另行订立技术保密条款，作为本合同正式内容的一部分，与本合同具有同等效力。

第九条 根据项目具体情况，经双方另行协商订立的附加条款，作为本合同正式内容的一部分，与本合同具有同等效力。

第十条 本合同的争议应由双方本着协商一致的原则解决，如双方协商不成的，则应向甲方所在地法院提起诉讼。

第十一条 保密条款：

1. 本合同保密内容范围为：

无

2. 本合同保密期限为：

无

3. 乙方应与可能知悉保密内容的人员签订技术秘密保护协议。

4. 各方应建立技术秘密保护制度。

5. 属技术保密的项目必须经省负责技术保密部门审查后，确定可否发表或用于国际合作和交流。

第十二条 甲方可根据具体情况决定乙方是否需要单位担保，若需要保证单位，应订立担保条款，作为本合同正式内容一部分。当乙方不履行或不完全履行本合同，以及没有或没有完全承担违约责任时，乙方的保证单位承担连带保证责任。

第十三条 本合同一式六份，各份具有同等效力。甲方存三份，乙方存二份，丙方存一份，本合同自签字之日起生效，有效期至项目结题后一年内。各方均应负合同的法律责任，不应受机构、人事变动的影响。

说明：本合同书中，凡是当事人约定无需填写的内容，应在空白处划（/）。

九、本合同签约各方

管理单位（甲方）：　广东省科学技术厅　（盖章）

单位地址：　广东省广州市连新路171号

法定代表人（或授权代表）：　黄宁生　_____　（签章）

联系人（经办人）姓名：　张燕　_____　（签章）

Email：　111@1.com

电话：　020-83163633

年　月　日

承担单位（乙方）：　广州市光机电技术研究院　（盖章）

二级部门：

单位地址：　广东省广州市萝岗区广州高新技术产业开发区科学城科研路3号

法定代表人（或法人代理）：　任豪　_____　（签章）

联系人（项目主管）姓名：　黄逸　_____　（签章）

Email：　huangyi0101@aliyun.com

电话：　020-32068940

开户单位名称：　广州市光机电技术研究院

开户银行及帐号：　中国工商银行广州石牌支行　3602098609000142256

年　月　日

乙方主管部门（丙方）：　广州市科技创新委员会　（盖章）

单位地址：　广东省广州市广州市越秀区府前路1号市政府大院

法定代表人（或法人代理）：　马正勇　_____　（签章）

联系人（项目主管）姓名：　创新人才处　_____　（签章）

Email：　lixiaoyin@gz.gov.cn

电话：　020-83127018

开户单位名称：　广州市科学和信息化局

开户银行及帐号：　广州银行营业管理部　328808010650

年　月　日

5.科研论文

IEEE Access
Multidisciplinary | Rapid Review | Open Access Journal

IEEE PHOTONICS SOCIETY SECTION

Received March 30, 2021, accepted April 22, 2021, date of publication April 27, 2021, date of current version May 5, 2021.

Digital Object Identifier 10.1109/ACCESS.2021.3075991

Improved Performance of GaN-Based Ultraviolet LEDs With Electron Blocking Layers Composed of Double-Peak *p*-Type $Al_xGa_{1-x}N$/GaN Superlattice Layers

YONG HUANG[1], ZHIYOU GUO[2,3], MIAO ZHANG[2,3], AND DAN XIANG[1]

[1]Guangdong Industrial Training Center, Guangdong Polytechnic Normal University, Guangzhou 510665, China
[2]Institute of the Opto-Electronic Materials and Technology, South China Normal University, Guangzhou 510631, China
[3]Guangdong Engineering Technology Research Center of Optoelectronic Functional Materials and Devices, South China Normal University, Guangzhou 510631, China

Corresponding author: Dan Xiang (gsdxdan@163.com)

This work was supported in part by the Guangdong Science and Technology Project under Grant 2016B090927009, Grant 2016B090927002, and Grant 201805010001; in part by the Special Projects in Universities' Key Fields of Guangdong Province under Grant 2020ZDZX2002; in part by the Special Projects in Key Fields of Artificial Intelligence in Colleges and Universities of Guangdong Province under Grant 2019KZDZX1042; and in part by the Project of Innovation in Colleges and Universities of Guangdong Province under Grant 2019KTSCX084.

ABSTRACT Past studies have demonstrated the positive impact of step-graded *p*-type $Al_xGa_{1-x}N$/GaN superlattice (SL) electron blocking layer (EBL) structures on the efficiency performance of ultraviolet (UV) GaN-based light-emitting diodes (LEDs). However, the optimal Al-grading structure of these SL EBLs remains unclear owing to a lack of systematic investigation. The present work addresses this issue by applying EBL composed of alternating half-peak, single-peak, and double-peak *p*-type $Al_xGa_{1-x}N$/GaN SL structures with varying values of x ranging from 0.05 to 0.15 in 0.05 step increments. Simulation analysis is employed to obtain the internal quantum efficiency (IQE), energy band diagrams, polarization compensation factor, hole concentration, and electron concentration of GaN-based UV LEDs with three different SL-EBL structures. The results obtained at an injection current of 200 mA demonstrate that UV LEDs with double-peak SL-EBL structures provide the maximum IQE, which is ~38% greater than that of devices employing the conventional EBL in simulation experiment. This SL-EBL is demonstrated to improve the hole injection and electron overflow performance of GaN-based UV LEDs owing to the polarization charge and lattice mismatch at the *p*-$Al_xGa_{1-x}N$/GaN interfaces. The reduced Al composition on the *p*-GaN side reduces the potential barrier of hole injection. Moreover, the predicted increase in the IQE of GaN-based UV LEDs with the optimal SL-EBL is verified experimentally.

INDEX TERMS Light emitting diodes, ultraviolet sources, superlattice electron blocking layers.

I. INTRODUCTION

Ultraviolet light-emitting diodes (UV-LEDs) have generated intensive interest due to their many advantages compared to conventional UV mercury lamps, as well as their wide applicability in numerous applications such as in water purification, medical treatment, analytical sensing and high-density optical storage devices [1]–[4]. Among the many developed UV LED technologies, GaN-based UV LEDs have attracted considerable attention owing to their direct bandgap, high electron saturation mobility, and large optical power output density [5], [6]. One of the most prominent advantages of GaN based UV LED technology is observed in AlGaN/GaN quantum well (QW)/quantum barrier (QB) heterostructures with different Al contents [7], [8]. However, the polarity of Ga-N covalent bonds generates electric dipole moments, which have a strong spontaneous polarization effect, leading to the formation of a built-in polarization field in GaN crystals. Accordingly, GaN-based UV LEDs suffer from various problems such as efficiency droop, electron leakage,

The associate editor coordinating the review of this manuscript and approving it for publication was Leo Spiekman.

nonuniform carrier distributions, and light extraction efficiency (LEE). All of these efficiencies are responsible for the low EQE of AlGaN UV LEDs [9].

This issue has been addressed by applying a *p*-type AlGaN electron blocking layer (EBL) to prevent the electron overflow, which has resulted in increased external quantum efficiency (EQE) and optical power output [2], [10]. Other studies have applied *p*-type $Al_xGa_{1-x}N$ layers with step-graded values of x as EBLs in GaN-based LEDs. For example, the application of an EBL composed of three thin *p*-type $Al_xGa_{1-x}N$ layers with step-graded values of $x = 0.04$, 0.08, and 0.12 was found to limit the observed droop in the EQE to just 29% less than its initial value, while the application of a 50 nm thick *p*-type $Al_{0.16}Ga_{0.84}N$ EBL exhibited a corresponding decrease of 44% [11]. In addition, the application of double-sided, step-graded $Al_xGa_{1-x}N$ EBL, with x being 5%, 10%, and 15% and a step width of 4 nm along each growth direction (from the last QW to p-AlGaN), improves internal quantum efficiency (IQE), optical output power, and nearly eliminating the droop in the IQE [12]. While these past studies have demonstrated the beneficial impact of step-graded $Al_xGa_{1-x}N$ EBLs on the IQE droop of GaN-based LEDs, absolute enhancements in the IQE and optical output power of the devices remain limited because hole injection is affected by the downward band-bending induced by the serious polarization at the interface between the EBL and the last QB of the LED [13], [14]. This issue has been addressed by the application of AlGaN/GaN superlattice (SL) structures as EBLs. For example, the application of an EBL composed of a *p*-type AlGaN/GaN SL with a graded Al doping composition was demonstrated to enable better hole injection and reduced electron leakage [15]. Analyses of LED devices with different AlGaN-based EBL materials have demonstrated that the Al component provides an important contribution toward their electron overflow suppression effect due to the resulting polarization field in the EBL [16]. Efforts to improve the hole injection and confine electron overflow in UV LEDs have led to the application of double-side step-graded SL-EBL (DSGS-EBL) structures [2]. Here, the DSGS-EBL structure was demonstrated to increase efficiency and optical power output due to the formation of effective conduction band barrier height, which prevented electron overflow into the *p*-type region. Zhang and Yin [17] investigated two types of AlGaN/GaN SL-EBL structures in GaN-based LEDs, and found that the SL-EBL with a step-graded Al molar fraction markedly decreased the efficiency droop. Lin *et al.* [18] reported that the application of an AlGaN/GaN SL-EBL in GaN-based LEDs markedly enhanced the optical power output by as much as 60%. While the above-discussed studies have demonstrated the optimal Al-grading structure of these SL-EBLs, the mechanism remains unclear owing to a lack of systematic investigation.

This paper addresses this issue by evaluating the performance of GaN-based UV LEDs with alternating half-peak, single-peak, and double-peak *p*-type $Al_xGa_{1-x}N$/GaN SL-EBL structures with x values ranging from 0.05 to 0.15 in

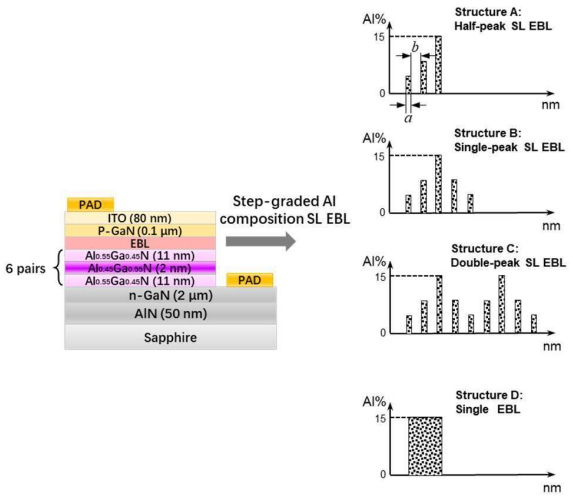

FIGURE 1. Schematic diagrams of the GaN LED with four structures of EBL.

increments of 0.05. Simulation analysis employing Advanced Physical Models of Semiconductor Devices (APSYS) software [16] are employed to obtain the IQE values, optical output power, and energy band diagrams of the LED structures. The results obtained demonstrate that GaN-based UV LEDs with the double-peak SL-EBL structures composed of double-peak step-graded Al composition SL EBL provide IQE values that are markedly greater than those of devices employing conventional, half-peak and single-peak SL-EBL structures. Moreover, the predicted increase in the IQE of GaN-based UV LEDs with the optimal SL-EBL structure is verified experimentally.

II. SIMULATIONS AND EXPERIMENTS

The structure of the multiple QW LEDs employed in the numerical analyses is illustrated in Fig. 1. The epitaxial layers consisted of the following: 1) a 50 nm thick undoped AlN buffer layer on a *c*-plane sapphire substrate; 2) a 2 μm thick n+-doped $Al_{0.65}Ga_{0.35}N$ contact layer with an Si doping of 5×10^{18} cm^{-3}; 3) six $Al_{0.45}Ga_{0.55}N$ QWs separated by seven 11 nm $Al_{0.55}Ga_{0.45}N$ GaN QBs; 4) *p*-type SL-EBLs with p doping of 9×10^{18} cm^{-3}; 5) a 0.1 μm thick *p*-type GaN contact layer with Mg doping of 2×10^{19} cm^{-3} provided by Cp_2Mg; 6) a 80 nm transparent conductive indium-tin-oxide (ITO) layer for current spreading. In addition, the different *p*-type EBL structures considered are presented in Figs.1 (a)-(d). Here, the thickness of an individual *p*-type $Al_xGa_{1-x}N$ layers is denoted as a, and the thickness of an individual *p*-type GaN layers is denoted as b. The effects of different values of a and b were investigated. In addition, the Al concentrations of the individual $Al_xGa_{1-x}N$ layers in the $Al_xGa_{1-x}N$/GaN SL-EBL structures are given, where structure A was composed of $Al_{0.05}Ga_{0.95}N$/GaN/$Al_{0.10}Ga_{0.90}N$/GaN/$Al_{0.15}Ga_{0.85}N$, structure B was composed of $Al_{0.05}Ga_{0.95}N$/GaN/$Al_{0.10}Ga_{0.90}N$/GaN/$Al_{0.15}Ga_{0.85}N$/GaN/$Al_{0.10}Ga_{0.90}N$/GaN/$Al_{0.05}Ga_{0.95}N$, and structure C was a concatenation of two structure B SL-EBLs. In structure D, we evaluated its

performance which is a conventional EBL that was a 10 nm thick p-type $Al_{0.15}Ga_{0.85}N$ EBL, for comparison.

The band diagram, as well as electrical and optical properties, were calculated in the simulations by the Poisson's equation, the Schrodinger equation, and the carrier transport equations. The Schockley-Read-Hall (SRH) lifetime within quantum wells was estimated to be 100 ns. The Auger recombination coefficient was set to $1 \times 10^{-30} cm^{-6}/s$ [19], [20]. The built-in interface polarization charges were calculated with the methods proposed by Fiorentini *et.al* [21]. The band offset ratio ($r = \Delta E_C/\Delta E_g$) was varied between 0.5 and 0.60 to accommodate the alternating step-graded Al composition of $x = 0.05 - 0.15$ in accordance with previously proposed practices for AlGaN and InGaN material systems [22], [23].

The experiments employed multiple QW LEDs grown on c-plane sapphire substrates by metal-organic chemical vapor deposition (MOCVD). The buffer layer, active layer, three types of SL EBL, and the conventional EBL of the devices were consistent with the finite element design. The growth temperature of the EBLs was 970 °C, and that of the other layers was 780 °C. The ITO film was deposited by magnetron sputtering and then a metal conductive coating (Pad; Fig. 1) consisting of Cr/Al/Cr/Ti/Au layers with respective thicknesses of 2/200/25/45/2000 nm was applied. In this electrode structure, Cr serves as an adhesion layer, Au serves as an excellent conductive and anti-oxidation layer, and the Al and Ti electrodes are included to improve the reliability of the devices. Finally, the diameter of the cylindrical LED mesa was 200 μm.

III. RESULTS AND DISCUSSION

The spontaneous polarization of GaN will be aligned along the [0001] direction because the epitaxial growth of GaN is in the c-plane direction of the sapphire substrate [24]. As such, the spontaneous polarization density of GaN can be given as

$$P_{pz,z}^{GaN} = (e_{31} - \frac{c_{13}}{c_{33}} e_{33})\varepsilon_1 \quad (1)$$

where e_{31}, e_{33}, c_{13}, and c_{33} are the relevant piezoelectric and elastic constants for GaN, and ε_1 is the strain tensor. The relationship between the polarization charge ρ_P and the magnitudes of the spontaneous polarization P_{sp} and piezoelectric polarization P_{pe} densities of the individual layers of $Al_xGa_{1-x}N$/GaN heterojunctions are given as follows.

$$\rho_P = P_{sp}(Al_xGa_{1-x}N) - P_{sp}(GaN) + P_{pe}(Al_xGa_{1-x}N) \quad (2)$$

The polarization charge density σ_{pol} per electron charge e at the $Al_xGa_{1-x}N$/GaN heterojunction interfaces and the electron sheet concentration n_s in the two dimensions can be respectively approximated by

$$\sigma_{pol}/e = -2[e_{31} - (c_{13}/c_{33})e_{33}](a_{GaN}/a_{AlN} - 1)x + P_{sp,z}^{GaN} - P_{sp,z}^{AlGaN} \quad (3)$$

$$n_s = \frac{\sigma_{pol}}{e} - (\varepsilon_{AlGaN}/de^2)(e\phi_b + E_F - \Delta E_c) + \frac{1}{2}N_d \quad (4)$$

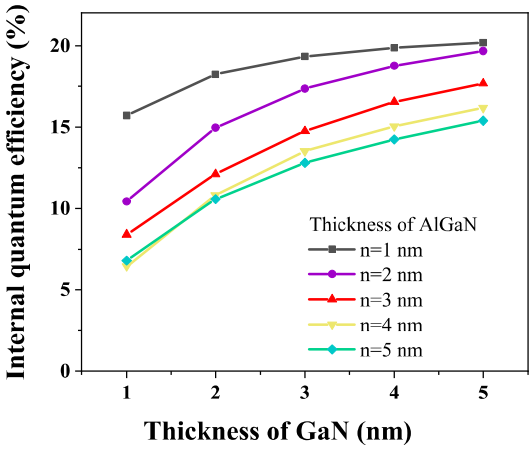

FIGURE 2. Simulated IQE values obtained for LED devices with an SL-EBL conforming to Structure A (i.e., a half-peak structure) operating at an injection current of 200 mA as a function of GaN layer thickness *b* with the AlGaN layer thickness *a* varied from 1-5 nm.

Here, a_{GaN} and a_{AlN} are the lattice constants of GaN and AlN, respectively, the values $P_{sp,z}$ accompanied by superscripts GaN and AlGaN denote the spontaneous polarization densities of GaN and AlGaN calculated based on Eq. (1), respectively, ε_{AlGaN} is the dielectric constant of $Al_xGa_{1-x}N$, d is the thickness of the $Al_xGa_{1-x}N$ barrier layer, ϕ_b is the Schottky barrier height of $Al_xGa_{1-x}N$, E_F is the Fermi energy, ΔE_c is the conduction-band offset ratio, and N_d is the donor concentration. It was confirmed that the two- dimensional (2D) carrier concentrations calculated from Eqs. (2), (3) and (4) at low to moderate Al concentrations (i.e., $x < 0.20$) were in very good agreement with those expected to arise from the combined effects of spontaneous and piezoelectric polarization [24].

We first evaluated the simulated IQE values obtained for a LED device with a SL-EBL in structure A at an injection current of 200 mA as a function of the GaN layer thickness b with the AlGaN layer thickness a varied from 1-5 nm. The results are presented in Fig. 2. We note that the IQE of the LED devices reaches maximum values in the range of 16% to 21% with varying b when $a = 1$ nm. This is accompanied by a high 2D electron sheet concentration in the AlGaN/GaN heterostructures, and the electrons are very close to the AlGaN/GaN interfaces. We also note that a decreasing QB-EBL thickness leads to a significant increase in the transconductance [25]. Therefore, the thickness of AlGaN in EBL is 1 nm in the subsequent simulations and experimental prepared device.

The simulated curves reflecting the IQE versus the injection current and the injection current versus voltage (I-V) obtained for LED devices with an SL-EBL conforming to structure A for various values of b and a fixed value of $a = 1$ nm are presented in Figs. 3(a) and (b), respectively. As shown in Fig. 3(a), the IQE increased with increasing b at an injection current ranging from 100 to 250 mA. The I-V curves exhibit a leftward shift for b values in the range of 1

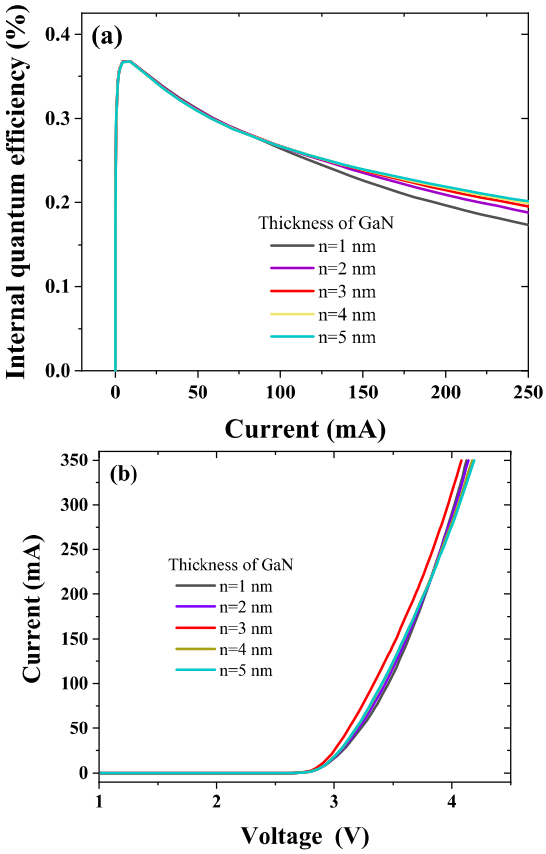

FIGURE 3. Simulated results obtained for LED devices with an SL-EBL in structure A for various of GaN thickness with a fixed 1 nm AlGaN; (a) IQE versus injection current; (b) inject current versus voltage (I-V).

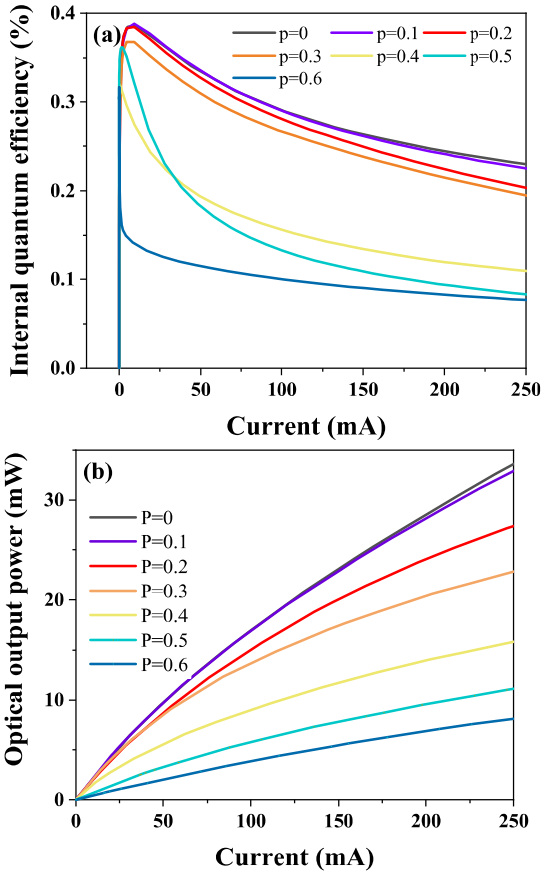

FIGURE 4. Simulated (a) IQE curves and (b) current-optical output power curves of the LEDs EBL polarization compensation factor of 0 to 0.6 in structure A.

to 3 nm, but further increases in b lead to a rightward shift. When the thickness of GaN increased from 1 to 3 nm, the polarization effect at the interface will be enhanced and hole injection improved, so the turn-on voltage will decrease and the I-V curves show the left shift. But when the thickness continues to increase, the injected carriers do not continue to increase, and the turn-on voltage increases for the device thickness greatly increased, so the curves show the right shift. Accordingly, we can conclude that $b = 3$ nm is the optimal value. Therefore, a value of $b = 3$ nm was applied in all subsequent simulations.

The simulated IQE-current curves and the optical power output versus injection current curves obtained for LED devices with an optimally designed SL-EBL conforming to structure A for various values of the EBL polarization compensation factor p in the range of 0 to 0.6 are presented in Figs. 4(a) and (b), respectively. The figures clearly indicate that the IQE and optical power output of the LEDs with the half-peak SL-EBL decrease as p increases from 0 to 0.6. Polarization arises at the AlGaN/GaN interfaces due to the different lattice constants of the materials, which generates tensile and compressive stresses that deform the lattice to form additional dipole moments by separating positive and negative charge centers [26], [27]. In addition, high-quality epitaxial growth of AlGaN materials is difficult to achieve due to the severe lattice mismatch and thermal expansion coefficient mismatch between AlGaN and the sapphire substrate, which results in AlGaN layers with high threading dislocation density (TDD) values. Therefore, these crystalline defects limit the extent to which the value of p can be reduced [13]. Accordingly, all subsequent simulations employed a value of $p = 0.2$.

The simulated I-V curves, IQE-current curves and current-optical output power curves obtained for LED devices having SL-EBL structures conforming to the three optimally designed structures A–C and the conventional EBL structure D are presented in Figs. 5(a), (b), and (c), respectively. As shown in Fig. 5(a), the I-V curves of the LED devices with the three SL-EBL structures A to C progressively shift rightward owing to the increasing overall thickness of the SL-EBLs. In addition, we note that the thickness of structure D lies between those of structures A and C. Therefore, the I-V curve of the LED device with EBL structure D also lies between those of the LED devices with SL-EBL structures A and C. As shown in Fig. 5(b), the IQE values at an injection current of 200 mA are 21.7%, 24.7%, 26.9%, and 19.7% for LEDs with EBL structures A, B, C, and D, respectively. Accordingly, the IQE value obtained for the LED device employing structure C was ∼24% greater than that obtained when employing structure A. Moreover, the

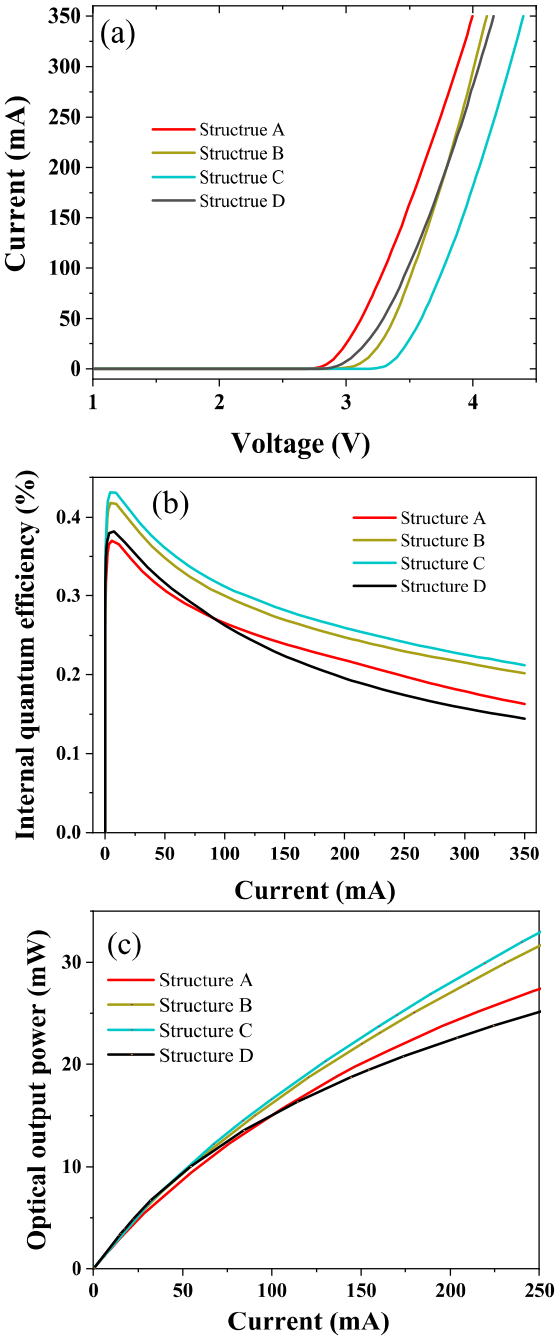

FIGURE 5. Simulation results obtained for LED devices having SL-EBLs conforming to the three different structures with optimal values of a = 1 nm and b = 3 nm (structures A–C), and the conventional EBL (structure D): (a) (I-V) curves; (b) IQE-current curves; (c) current-optical output power curves of the four LEDs.

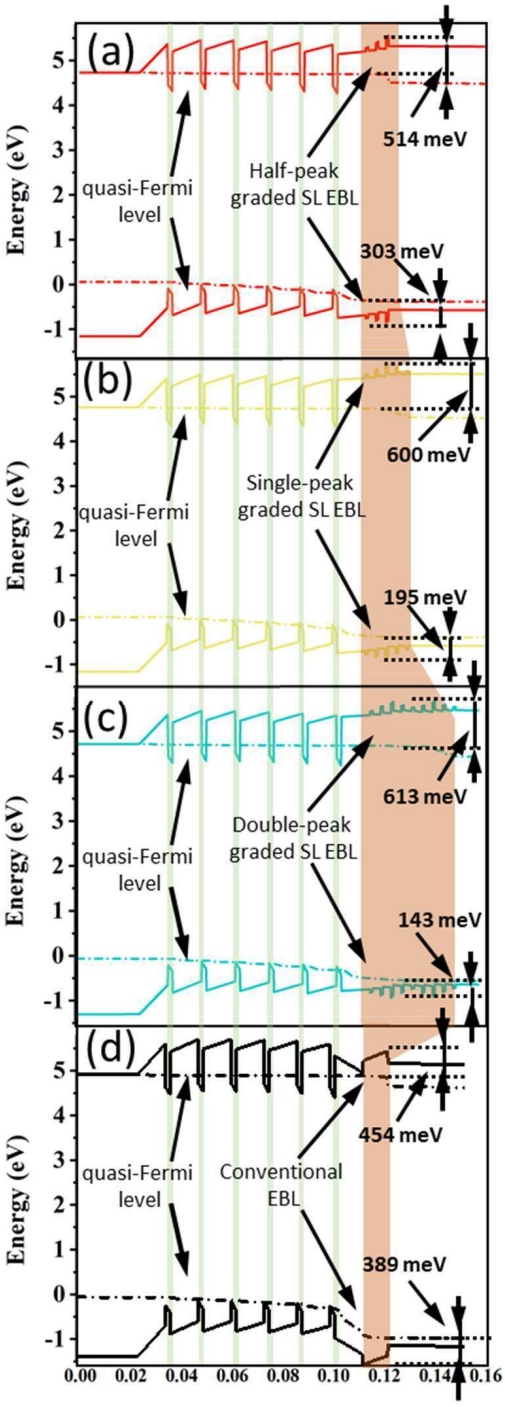

FIGURE 6. Simulated energy band diagrams for LED devices with different EBL structures: (a) structure A (half-peak SL-EBL); (b) structure B (single-peak SL-EBL); (c) structure C (double-peak SL-EBL); (d) structure D (conventional EBL).

IQE value obtained for the LED device employing structure C was ∼38% greater than that of the device employing the conventional EBL structure D. These results demonstrate that the IQE of the LED devices is sensitive to the structure of the *p*-type $Al_xGa_{1-x}N$/GaN SL-EBL, and the EBL structure accordingly affects the overall device performance. The IQE values also demonstrate a standard optimization behavior, where the IQE values of the devices initially increase with an increasing number of $Al_xGa_{1-x}N$/GaN SL layers from half-peak to double-peak structures.

These results can be further analyzed from the perspective of the energy band diagrams given in Fig. 6(a)–(d). Here, we note that the electron barrier heights of the LEDs with SL-EBL structures A, B, and C were 514 meV, 600 meV, and 613 meV, respectively, while that of the LED with

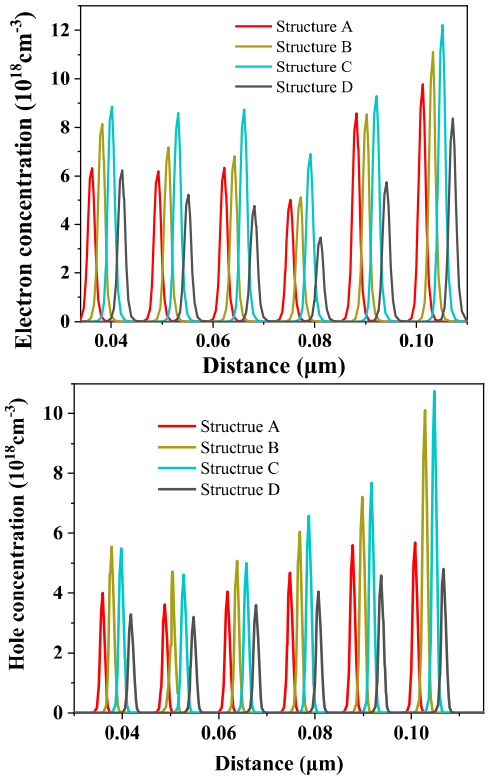

FIGURE 7. Simulation results obtained at an injection current of 200 mA for LED devices having SL-EBLs conforming to structures A–C, and the conventional EBL structure D: (a) electron concentration; (b) hole electron concentration.

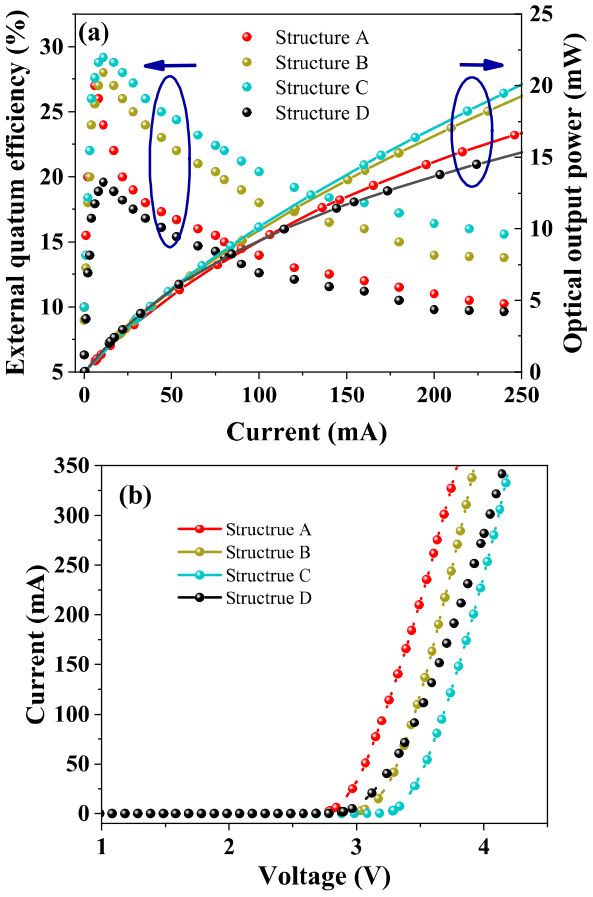

FIGURE 8. The external quantum efficiency (EQE) versus injection current and current-optical output power (a) and I-V curves (b) measured at room temperature for four types of EBL in UV LED, and the inset figure shows the current-optical output power curves of the four LEDs.

conventional EBL structure D was 454 meV. The increasing electron concentration with increasing electron barrier height observed for structures A–C increased the IQE values obtained by the LEDs, but also increased the leakage current, which in turn increased the extent to which the IQE droops with increasing injection current [28], [29]. However, we further note from Fig. 6 that the hole barrier heights of the LEDs, given as $E_F - E_V$, where E_V is the valence band energy, were also affected by the four EBL structures. Here, the hole barrier heights of the LEDs with SL-EBL structures A, B, and C were 303 meV, 195 meV, and 143 meV, respectively, while that of the LED with conventional EBL structure D was 389 meV. The increasing hole concentration with decreasing hole barrier height observed for structures A–C increased hole injection, which in turn increased LED efficiency.

Fig.7 shows the electron concentration and hole concentration in the active region of the four structure devices at an injection current of 200 mA respectively. The horizontal position of carrier concentration has been slightly right-shifted for structure B, C, and D. The progressively increasing electron concentration and decreasing hole injection barrier observed for the LED devices employing SL-EBL structures A–C can be analyzed as follows. We first note that surface states are the source of 2D electron sheet concentrations, and these states varying according to the thickness and alloy composition of the AlGaN barrier layers [7]. Moreover, according to equation (2), $P_{sp}\,(Al_xGa_{1-x}N)$ increases with increasing x. Therefore, the initially successive addition of $Al_xGa_{1-x}N$ layers with increasing x progressively increased the spontaneous polarization density of the SL-EBL structure, and the increasing spontaneous and piezoelectric polarization effects of the $Al_xGa_{1-x}N$/GaN layers decreased the hole barrier height owing to the progressive shifting of the valance band. In addition, grading the Al composition progressively increased the lattice mismatch at the interfaces of the AlGaN/GaN heterostructures, which generated large polarization-induced electric fields. The reason that the hole injection and electron overflow differed between the LED employing single-peak SL-EBL structure A and the LED employing half-peak SL-EBL structure B is because the lower Al composition on the p-type GaN side of structure B reduced the potential barrier to hole injection, decreased the lattice mismatch between the AlGaN and GaN layers, and lowered the overall Al content in the SL-EBL [27]. The LED employing double-peak SL-EBL structure C has the lowest electron leakage and largest hole concentration in the QWs due to the double electron blocking effect of the SL-EBL structure and the greatest hole injection efficiency.

Finally, Fig. 8(a) and (b) presents measured EQE values, the current-optical output power and the I-V curves of the

multiple QW LED devices fabricated with the three SL-EBL structures and conventional EBL structure D as a function of the injected current at room temperature. The experimental EQE values of the LEDs employing SL-EBL structures A, B, and C, and that employing conventional EBL structure D obtained at an injection current of 200 mA, are 13.0%, 14.1%, 16.4%, and 11.8%, respectively. Accordingly, the EQE value obtained for the LED device employing structure C was ∼26% greater than that obtained when employing structure A. Moreover, the EQE value obtained for the LED device employing structure C was ∼38% greater than that of the device employing conventional EBL structure D.

IV. CONCLUSION

This paper addressed the absence of systematic investigation into the optimal Al-grading structure of SL-EBLs by evaluating the effect of three types of step-graded $Al_xGa_{1-x}N$ SL-EBLs on the performance of GaN-based UV LEDs via simulations. The results obtained at an injection current of 200 mA demonstrate that UV LEDs with double-peak SL-EBL structures provide the maximum IQE, which is ∼38% greater than that of devices employing the conventional EBL at an injection current of 200 mA in simulations, and this improvement was confirmed by experiments. The double-peak SL-EBL structure was demonstrated to improve the hole injection and electron overflow performance of GaN-based LEDs owing to the polarization charge and lattice mismatch at the p-type $Al_xGa_{1-x}N$/GaN interfaces. Lower Al composition on the p-type GaN side reduced the potential barrier to hole injection. Finally, the predicted increase in the IQE of GaN-based UV LEDs with the optimal SL-EBL structure was verified experimentally.

REFERENCES

[1] K. Song, M. Mohseni, and F. Taghipour, "Application of ultraviolet light-emitting diodes (UV-LEDs) for water disinfection: A review," *Water Res.*, vol. 94, pp. 341–349, May 2016, doi: 10.1016/j.watres.2016.03.003.

[2] B. Jain, R. T. Velpula, S. Velpula, H.-D. Nguyen, and H. P. T. Nguyen, "Enhanced hole transport in AlGaN deep ultraviolet light-emitting diodes using a double-sided step graded superlattice electron blocking layer," *J. Opt. Soc. Amer. B, Opt. Phys.*, vol. 37, no. 9, pp. 2564–2569, Aug. 2020, doi: 10.1364/JOSAB.399773.

[3] K. Ding, V. Avrutin, Ü. Özgür, and H. Morkoç, "Status of growth of group III-nitride heterostructures for deep ultraviolet light-emitting diodes," *Crystals*, vol. 7, no. 10, p. 300, Oct. 2017, doi: 10.3390/cryst7100300.

[4] Z. Ren, H. Yu, Z. Liu, D. Wang, C. Xing, H. Zhang, C. Huang, S. Long, and H. Sun, "Band engineering of III-nitride-based deep-ultraviolet light-emitting diodes: A review," *J. Phys. D, Appl. Phys.*, vol. 53, no. 7, Dec. 2019, Art. no. 073002, doi: 10.1088/1361-6463/ab4d7b.

[5] A. Pandey, W. J. Shin, J. Gim, R. Hovden, and Z. Mi, "High-efficiency AlGaN/GaN/AlGaN tunnel junction ultraviolet light-emitting diodes," *Photon. Res.*, vol. 8, no. 3, pp. 331–337. Mar. 2020, doi: 10.1364/PRJ.383652.

[6] D. Li, K. Jiang, X. Sun, and C. Guo, "AlGaN photonics: Recent advances in materials and ultraviolet devices," *Adv. Opt. Photon.*, vol. 10, no. 1, pp. 43–110, Jan. 2018, doi: 10.1364/AOP.10.000043.

[7] H. Sun, S. Mitra, R. C. Subedi, Y. Zhang, W. Guo, J. Ye, M. K. Shakfa, T. K. Ng, B. S. Ooi, I. S. Roqan, Z. Zhang, J. Dai, C. Chen, and S. Long, "Unambiguously enhanced ultraviolet luminescence of AlGaN wavy quantum well structures grown on large misoriented sapphire substrate," *Adv. Funct. Mater.*, vol. 29, no. 48, Sep. 2019, Art. no. 1905445, doi: 10.1002/adfm.201905445.

[8] Z. Zhuang, D. Iida, and K. Ohkawa, "Enhanced performance of N-polar AlGaN-based deep-ultraviolet light-emitting diodes," *Opt. Exp.*, vol. 28, no. 21, pp. 30423–30431, Oct. 2020, doi: 10.1364/OE.403168.

[9] H.-Y. Ryu, I.-G. Choi, H.-S. Choi, and J.-I. Shim, "Investigation of light extraction efficiency in AlGaN deep-ultraviolet light-emitting diodes," *Appl. Phys. Exp.*, vol. 6, no. 6, Jun. 2013, Art. no. 062101, doi: 10.7567/APEX.6.062101.

[10] C. Chu, Q. Chen, K. Tian, J. Che, H. Shao, J. Kou, Y. Zhang, C. Chen, Z.-H. Zhang, and J. Dai, "Modulating the layer resistivity by band-engineering to improve the current spreading for DUV LEDs," *IEEE Photon. Technol. Lett.*, vol. 31, no. 15, pp. 1201–1204, Aug. 1, 2019, doi: 10.1109/LPT.2019.2920527.

[11] B.-C. Lin, K.-J. Chen, C.-H. Wang, C.-H. Chiu, Y.-P. Lan, C.-C. Lin, P.-T. Lee, M.-H. Shih, Y.-K. Kuo, and H.-C. Kuo, "Hole injection and electron overflow improvement in InGaN/GaN light-emitting diodes by a tapered AlGaN electron blocking layer," *Opt. Exp.*, vol. 22, no. 1, pp. 463–469, Jan. 2014, doi: 10.1364/OE.22.000463.

[12] S. Prasad, R. K. Mondal, V. Chatterjee, and S. Pal, "Double-side step-graded AlGaN electron blocking layer for nearly droop-free GaN-based blue LEDs," *Superlattices Microstructures*, vol. 132, Aug. 2019, Art. no. 106167, doi: 10.1016/j.spmi.2019.106167.

[13] S.-H. Han, D.-Y. Lee, S.-J. Lee, C.-Y. Cho, M.-K. Kwon, S. P. Lee, D. Y. Noh, D.-J. Kim, Y. C. Kim, and S.-J. Park, "Effect of electron blocking layer on efficiency droop in InGaN/GaN multiple quantum well light-emitting diodes," *Appl. Phys. Lett.*, vol. 94, no. 23, Jun. 2009, Art. no. 231123, doi: 10.1063/1.3153508.

[14] H. Hirayama, Y. Tsukada, T. Maeda, and N. Kamata, "Marked enhancement in the efficiency of deep-ultraviolet AlGaN light-emitting diodes by using a multiquantum-barrier electron blocking layer," *Appl. Phys. Exp.*, vol. 3, no. 3, Feb. 2010, Art. no. 031002, doi: 10.1143/APEX.3.031002.

[15] J. H. Park, D. Y. Kim, S. Hwang, D. Meyaard, E. F. Schubert, Y. D. Han, J. W. Choi, J. Cho, and J. K. Kim, "Enhanced overall efficiency of GaInN-based light-emitting diodes with reduced efficiency droop by Al-composition-graded AlGaN/GaN superlattice electron blocking layer," *Appl. Phys. Lett.*, vol. 103, no. 6, Aug. 2013, Art. no. 061104, doi: 10.1063/1.4817800.

[16] Z. M. S. Li, "On the importance of AlGaN electron blocking layer design for GaN-based light-emitting diodes," *Appl. Phys. Lett.*, vol. 103, no. 23, Dec. 2013, Art. no. 233505, doi: 10.1063/1.4839417.

[17] Y. Y. Zhang and Y. A. Yin, "Performance enhancement of blue light-emitting diodes with a special designed AlGaN/GaN superlattice electron-blocking layer," *Appl. Phys. Lett.*, vol. 99, no. 22, Nov. 2011, Art. no. 221103, doi: 10.1063/1.3653390.

[18] B.-C. Lin, K.-J. Chen, H.-V. Han, Y.-P. Lan, C.-H. Chiu, C.-C. Lin, M.-H. Shih, P.-T. Lee, and H.-C. Kuo, "Advantages of blue LEDs with graded-composition AlGaN/GaN superlattice EBL," *IEEE Photon. Technol. Lett.*, vol. 25, no. 21, pp. 2062–2065, Nov. 2013, doi: 10.1109/LPT.2013.2281068.

[19] Y. C. Shen, G. O. Mueller, S. Watanabe, N. F. Gardner, A. Munkholm, and M. R. Krames, "Auger recombination in InGaN measured by photoluminescence," *Appl. Phys. Lett.*, vol. 91, no. 14, Oct. 2007, Art. no. 141101, doi: 10.1063/1.2785135.

[20] Y.-K. Kuo, J.-Y. Chang, F.-M. Chen, Y.-H. Shih, and H.-T. Chang, "Numerical investigation on the carrier transport characteristics of AlGaN deep-UV light-emitting diodes," *IEEE J. Quantum Electron.*, vol. 52, no. 4, pp. 1–5, Apr. 2016, doi: 10.1109/JQE.2016.2535252.

[21] V. Fiorentini, F. Bernardini, and O. Ambacher, "Evidence for nonlinear macroscopic polarization in III–V nitride alloy heterostructures," *Appl. Phys. Lett.*, vol. 80, no. 7, pp. 1204–1206, Feb. 2002, doi: 10.1063/1.1448668.

[22] J. Piprek and Z. M. S. Li, "Sensitivity analysis of electron leakage in III-nitride light-emitting diodes," *Appl. Phys. Lett.*, vol. 102, no. 13, Apr. 2013, Art. no. 131103, doi: 10.1063/1.4799672.

[23] L. Lu, G. G. Ding, Y. Zhang, Y. H. Liu, and F. J. Xu, "Improved performance of AlGaN-based deep ultraviolet light-emitting diode using modulated-taper design for p-AlGaN layer," *Semicond. Sci. Technol.*, vol. 33, no. 3, Feb. 2018, Art. no. 035008, doi: 10.1088/1361-6641/aaa8b2.

[24] E. T. Yu, X. Z. Dang, P. M. Asbeck, S. S. Lau, and G. J. Sullivan, "Spontaneous and piezoelectric polarization effects in III–V nitride heterostructures," *J. Vac. Sci. Technol. B, Microelectron. Nanometer Struct.*, vol. 17, no. 4, pp. 1742–1749, Aug. 1999, doi: 10.1116/1.590818.

[25] O. Ambacher, B. Foutz, J. Smart, J. R. Shealy, N. G. Weimann, K. Chu, M. Murphy, A. J. Sierakowski, W. J. Schaff, L. F. Eastman, R. Dimitrov, A. Mitchell, and M. Stutzmann, "Two dimensional electron gases induced by spontaneous and piezoelectric polarization in undoped and doped AlGaN/GaN heterostructures," *J. Appl. Phys.*, vol. 87, no. 1, pp. 334–344, Jan. 2000, doi: 10.1063/1.371866.

[26] J.-R. Chen, C.-H. Lee, T.-S. Ko, Y.-A. Chang, T.-C. Lu, H.-C. Kuo, Y.-K. Kuo, and S.-C. Wang, "Effects of built-in polarization and carrier overflow on InGaN quantum-well lasers with electronic blocking layers," *J. Lightw. Technol.*, vol. 26, no. 3, pp. 329–337, Feb. 2008, doi: 10.1109/JLT.2007.909908.

[27] H. J. Kim, S. Choi, S.-S. Kim, J.-H. Ryou, P. D. Yoder, R. D. Dupuis, A. M. Fischer, K. Sun, and F. A. Ponce, "Improvement of quantum efficiency by employing active-layer-friendly lattice-matched InAlN electron blocking layer in green light-emitting diodes," *Appl. Phys. Lett.*, vol. 96, no. 10, Mar. 2010, Art. no. 101102, doi: 10.1063/1.3353995.

[28] B. Jogai, "Influence of surface states on the two-dimensional electron gas in AlGaN/GaN heterojunction field-effect transistors," *J. Appl. Phys.*, vol. 93, no. 3, pp. 1631–1635, Feb. 2003, doi: 10.1063/1.1530729.

[29] A. David, M. J. Grundmann, J. F. Kaeding, N. F. Gardner, T. G. Mihopoulos, and M. R. Krames, "Carrier distribution in (0001)InGaN / GaN multiple quantum well light-emitting diodes," *Appl. Phys. Lett.*, vol. 92, no. 5, Feb. 2008, Art. no. 053502, doi: 10.1063/1.2839305.

YONG HUANG received the B.S. degree from Foshan University, in 2004, the M.S. degree from the South China University of Technology, in 2007, and the Ph.D. degree from South China Normal University, in 2018. His research interests include GaN based UV LED, visible light communication LED, and micro-LED.

ZHIYOU GUO was born in Liaoning, China, in 1959. He is currently the Professor from South China Normal University, China, in 2006. His research interests include wide band gap semiconductor materials and devices and GaN based micro-LED devices for visible light communication.

MIAO ZHANG received the B.S. degree in electronic science and technology from Hohai University, China, in 2019. He is currently pursuing the M.S. degree in microelectronics and solid-state electronics with South China Normal University, China.

DAN XIANG was born in Yichang, Hubei, China, in 1980. She received the Ph.D. degree from the South China University of Technology, China. She works with Guangdong Polytechnic Normal University. Her research interests include digital design and LED manufacturing technology and application.

GaN-Based High-Response Frequency and High-Optical Power Matrix Micro-LED for Visible Light Communication

Yong Huang, Zhiyou Guo, Xiaojun Wang, Huazhi Li, and Dan Xiang

***Abstract*— Light-emitting diodes (LEDs) with high response frequency and high power can be applied in visible light communication(VLC). This letter studies the response frequency and optical output power of the gallium nitride (GaN) based matrix micro-LED (μLED) for visible light communication. The blue-emitting GaNμLEDs with the format from 1 × 1 to6 × 6 are fabricated and used to analyze the relationship between the matrix format and the response frequency, as well as the output optical power and the data transmission performance of the matrix μLED. The experimental and analysis results show that the GaN-based matrix μLED responsefrequency can be improved by an increase in the injection current density increased and a decrease in device capacitance. The experimental comparison result indicates that the −3 dB response frequency changed from 85 MHz to401 MHz at a 60mA injection current progressively increased as the matrix array size from 1 × 1 to 6 × 6, the 6 × 6 matrix μLED optical output power reaches a value of 356.7 mW.**

***Index Terms*— Matrix micro-LED, response frequency, visible light communication.**

I. Introduction

VISIBLE light communication (VLC) has numerous advantages over typical radio-based communication, including ultra-high data transmission rates, high security requirements, and no need for radio spectrum authentication [1], [2]. These advantages make the VLC light-emitting diodes (LEDs) suited for short-distance communication, indoor positioning, indoor internet networks, and communication under electromagnetic field sensitivity conditions.

Manuscript received August 15, 2020; accepted August 31, 2020. Date ofpublication September 2,2020; date of current version September 25, 2020. This work was supported in part by the Guangdong Science and Technology Project under Grant 2016B090927009, Grant 2016B090927002, and Grant 2019KTSCX084; in part by the Guangzhou Science and Technology Project under Grant 201805010001; and in part by theNational Key ResearchandDevelopment Project under Grant 2016YFC0104900. The review of thisletter was arranged by Editor L. K. Nanver. *(Corresponding author: Dan Xiang.)*

Yong Huang, Xiaojun Wang, and Huazhi Li are with the Industrial Training Center, Guangdong Polytechnic Normal University, Guangzhou 510665, China.

Zhiyou Guo is with the Institute of the Opto-Electronic Materials and Technology, South China Normal University, Guangzhou 510631, China.

Dan Xiang is with the Industrial Training Center, Guangdong Polytechnic Normal University, Guangzhou 510665, China, and also with Guangzhou Sonostar Technology Company Ltd., Guangzhou 510665, China (e-mail: gsxd@gpnu.edu.cn).

Color versions of one or more of the figures in this letter are available online at http://ieeexplore.ieee.org.

Digital Object Identifier 10.1109/LED.2020.3021282

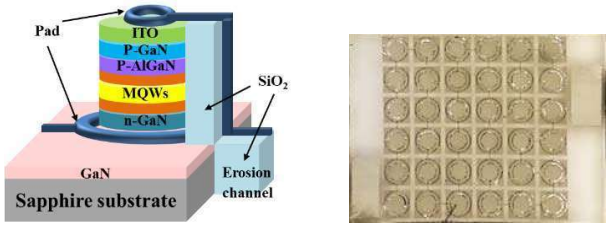

Fig. 1. (a) Schematic illustrating the structure of a single cylindrical GaN LED composed of epitaxial layers and toroidal electrodes. (b) Image of a 6 × 6 matrix μLEDarray chip.

The common transmissioncomponent of a VLC system is a LED andan optimal VLC system capable of high-speed data transmission requires an LED device with high optical output power coupled with a high electrical-to-optical response frequency [1]. The −3 dB response frequency of an LED device can be dramatically increased to hundreds of MHz by using micro light-emitting diodes (μLEDs) [3], [4]. Also, by forming a quenching center by doping the epitaxial layers of a device to enhance the modulation speed [2], [5], or by adopting a quantum well structure to reduce the carrier lifetime to the order of a tenth of a nanosecond, the device's response frequency improved [3]. Xie *et al.* [6] fabricated a matrix array, and the achieved optical output power was greater than 18.0 mW at the −6 dB modulation bandwidth of 285 MHz. In the mentioned studies, carrier diffusion has been demonstrated to be related to the structural characteristics of μLEDs, including the electrode shape, electrode conductivity, and the degree to which the resistivity of epitaxial layer materials is matched [7]. Also, the capacitance characteristics have been demonstrated to be related to the device's operating frequency and active area size. The presence of mutually influential relationships between the mentioned factors has also been demonstrated [8].

To improve the device's response frequency and optical output power, this letter reports a series-connected6 × 6 matrix μLED, where the −3 dB response frequency reached 401 MHz at an optical output power of 356.7 mW.

II. Experiment and Testing

A. Electronic Device Fabrication

The structure of the epitaxial layers and toroidal electrodes of cylindrical GaN LEDs analyzed in this study is presented in Fig.1(a). To ensure high response frequency and brightness, the epitaxial layers consisted of the following:

1) a 800 nm thick un-doped GaN buffer layer on a c-plane substrate; 2) a 3000 nm thick n+-doped GaN confinement layer; 3) a multi-quantum well (MQW) active region consisting of five 3 nm thick $In_{0.15}Ga_{0.85}N$ quantum wells separated by six12nm thick GaN barrier layers; 4) a 20 nm thick p-$Al_{0.1}Ga_{0.9}N$ confinement layer; and 5) a 100 nm thick p-doped GaN capping layer. The ITO film and a multi-layer metal conductive coating (Pad) consisting of Cr/Al/Cr/Ti/Au with thicknesses of 20/2,000/250/ 450/20,000 Å was applied. The diameter of the fabricated cylindrical layered LED was uniform andequal to 30 μm for all matrix arrays. In the processing of the prepared LED, SiO_2 was deposited in the erosion channel as a pad bridge between the matrix array unit, and eachunit was independently connected in series using conductive metal wires to ensure a high optical output power. The image of a 6×6 μLED array chip is displayed in Fig.1 (b). The outer ring of each unit was the negative electrode, and the inner ring was the positive electrode, which is connected in series. Six μLEDs were manufactured by the similar design and preparation processing with the matrix format from 1×1 to 6×6.

B. Testing System

In the test system, a DC bias current and a continuous sine wave modulation signal were both fed to the LED by Bias Tee DC bias Pulsar. The test equipment included the Vector Network Analyzer ZNB 4, and a high-speed photodetector Newport 818-BB- 21A. The Vector Network Analyzer ZNB 4 was used in the small signal response frequency test, and an oscilloscope (Tektronix DSO73304D 33 GHz) and arbitrary waveform generator (AWG, Tektronix AWG7122C 24 Gsa/s) were used for theeye diagram testing. The optical output power was tested by an Optical power meter (HAAS-2000 EVERFINE).

III. Results and Discussion

There are two major influencing factors of the optical response frequency of LEDs: the carrier recombination time and the RC time constant [9].

The I-V curves of six matrix μLEDs are shown in Fig.2 (a), where it is presented how the operating voltage was related to the unit number of the μLEDs. The operating voltage of the 6×6 matrix μLED was $\sim$ 114V. The optical output power of the μLEDs is shown in Fig.2 (b), where the injection current was 60 mA, and the output optical power of the 6×6 matrix μLED reached 356.7 mW.

The -3 dB response frequency, which is proportional to the current density J, can be expressed as follows [3]:

$$f_{-3dB} = \frac{1}{2\pi\tau}\sqrt{\frac{BJ}{qd}} \tag{1}$$

Based on the spontaneous emission time of carriers and recombination mechanism in the LED, the carrier lifetime τ can be calculated by [10]:

$$\frac{1}{\tau} = \frac{1}{\tau_r} + \frac{1}{\tau_{nr}} \tag{2}$$

A shorter lifetime τ can be achieved by reducing both radiative (τ_r) and non-radiative (τ_{nr}) times, as they are both related

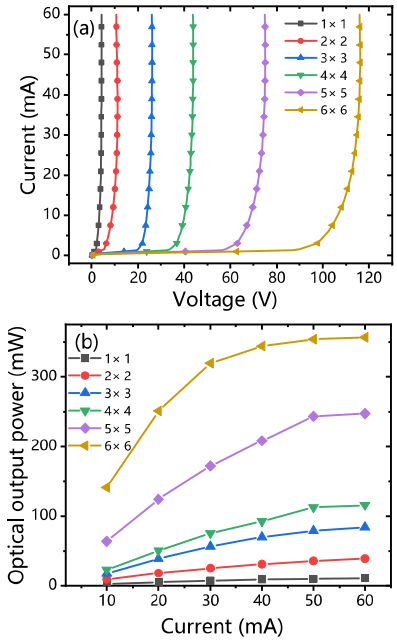

Fig. 2. The performance of sixmatrix μLEDs: (a) I-V curves, and (b) L-I curves.

the current density J. The normalized responses concerning the response frequency of 6×6 μLED matrix arrays, where the response frequency varied from 103 MHz to 401 MHz, at the injection current from 10 mA to 60 mA are presented in Fig. 3 (a). As shown in the inset imagein Fig. 3 (a), the current was larger than 60 mA, i.e., 65 mA, and the metal wire was burnt due to the excessive current. This occurred because the width of the metal wire was only 3 μm and the pad temperature increased dramatically when the current reached about 65 mA.

The response frequency of a LED represents the relationship between the modulation frequency and the output power. Since the speed at which a LED injects carriers is lower than the frequency of the modulation signal, the output power decreases at high frequencies. The power transfer function of a LED device can be expressed as [11]

$$P(f) = \frac{1}{\sqrt{1 + (2\pi f\tau)^2}} \tag{3}$$

where $P(f)$ donates the response frequency, f represents the modulation frequency, and τ is time constant and $\tau \approx RC$ in this equation.

When a LED turns on, the junction capacitance consists of two main parts: the depletion layer capacitance C_{dl}, and the diffusion capacitance C_{diff}. For an array consisting of n LED units, the capacitance decreases linearly concerning n, so the capacitance of the array is given as:

$$C_n = C_{dl}/n \tag{4}$$

The diffusion capacitance was caused by the rearrangement of a few carriers when the device was biased forward. The diffusion capacitance is [12]:

$$C_{diff} = \frac{qI}{KT}(\tau/2\omega)^2 \tag{5}$$

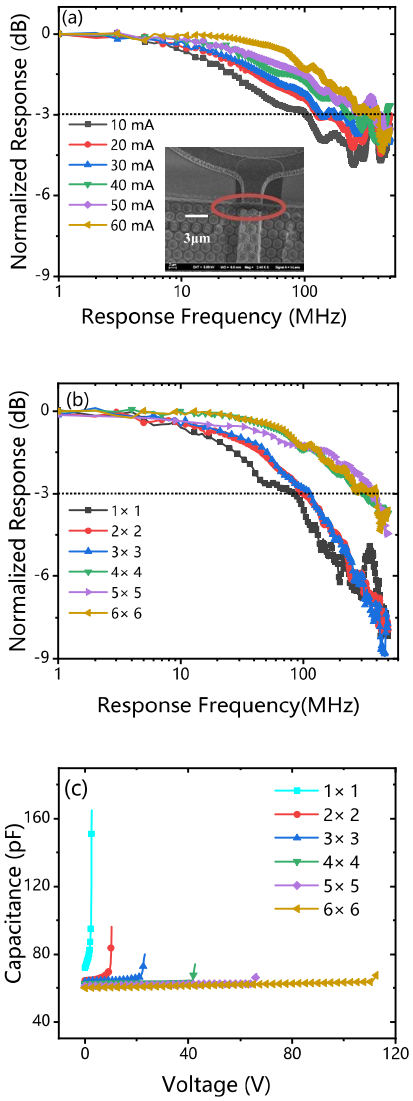

Fig. 3. (a) Normalized responses concerning the response frequency of the 6 × 6 μLED matrix array at the injection current from 10 mA to 60 mA. The inset image shows the wire break between matrix units when the injection current over 60 mA. (b) Normalized response frequency of 1 × 1 to 6 × 6 matrix μLEDs at 60 mA injection current, and (c) for the capacitance of μLEDs when they are superimposed on a 60 mA and 30 MHz signal frequency.

where q is the electroncharge, K is Boltzmann constant, I donates the forward bias current, T is the thermodynamic temperature, τ is the minority carriers' lifetime and ω is the signal frequency, The excess carriers' lifetime in a LED was the minority carriers' lifetime.

As shown in Fig. 3 (b), the −3 dB response frequency from 85 MHz to 401 MHzat a 60 mA injection current progressively increased as the matrix array size from 1 × 1 to 6 × 6. According to (5), C_{diff} is inversely proportional to signal frequency ω, so when the time constant decreases, and in (3), $P(f)$ could be increasing and the tested -3 dB response frequency improves.

Fig.3 (c) shows that the capacitance decreased from 165 pF to 96.4 pF, 80.9 pF, 74.2 pF, 68.3 pF, and 67.3 pF gradually (device capacitance was tested using a Hewlett Packard 4192A

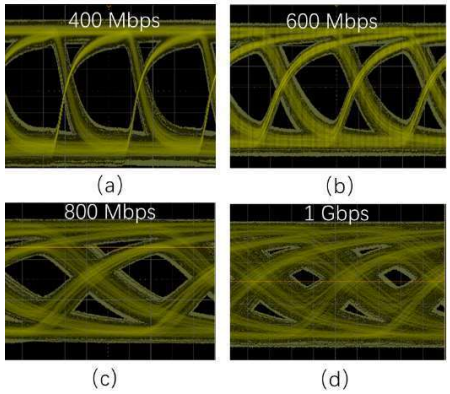

Fig. 4. The eye diagrams of a 6 × 6 matrix VLC LED at (a) 400 M, (b) 600 M, (c) 800 M and (d)1G bps.

LF impedance analyzer, andthe test signal frequency was 30 MHz). Before the matrix μLED turns on, the capacitance is ∼61pF. Inthe LED timeconstant formula, R consist of the resistance of each light-emitting diode unit, the wire resistance, and ohmic contact resistance. According to (4), capacitance reduction was fixed. In 5 × 5 and 6 × 6 devices, the resistance increased faster than the capacitance decreased according tothe series resistance formula. So, the −3 dB response frequency was not further increasing remarkedly when the matrix number increasing.

In the eye diagram test, the signal obtained by the arbitrary waveform generator peak to peak voltage was $V_{pp} = 0.6$ V, and the device was superimposed on a 60 mA dc bias with bias tee. The optical signal was coupled by a high-speed photodetector (Newport 818-BB-21A). Fig. 4 (a)-(d) show the eye diagrams of the 6 × 6 matrix μLED triggered by an arbitrary wave generator at 400 Mbps, 600 Mbps, 800 Mbps, and 1 Gbps, respectively. When the signal frequency increased from 400 Mbps to 1 Gbps, the rise time increased from 10 ns to 40 ns, the fall time increasedfrom 5ns to 30ns, and the eye-crossing percentage decreased from ∼75% to ∼50%. Therefore, a poor signal-to-noise ratio in small-size devices can limit largesignal modulation. When thetransmission rate reached 1 Gbps, the eye diagram gradually became obscured, which indicated that the inter symbol interference has increased significantly.

IV. Conclusion

This letter studies the response frequency and optical output power of a VLC LED by fabricating a series of high-operating voltage blue-emitting GaN μLED arrays in various matrix formats from 1 × 1 to 6 × 6 and evaluating their VLC performancesin terms of the response frequency, optical output power, and susceptibility to the eyediagram. The experimental comparisonresults indicated that the −3 dB response frequency increased from 85 MHz to401 MHz at an injection current of 60mA when the matrix array size changed from 1 × 1 to 6 × 6, and the optical output power of the 6 × 6 matrix μLED reached 356.7 mW. The designed GaN-based matrix micro-LED with high response frequency and high optical output power could be applied to visible light communication systems.

REFERENCES

[1] M. Manikandan, D. Nirmal, J. Ajayan, P. Mohankumar, P. Prajoon, and L. Arivazhagan, "A review of blue light emitting diodes for future solid-state lighting and visible light communication applications," *Superlattices Microstruct.*, vol. 136, pp. 106294-1–106294-21, Dec. 2019, doi: 10.1016/j.spmi.2019.106294.

[2] A. Rashidi, M. Monavarian, A. Aragon, S. Okur, M. Nami, A. Rishinaramangalam, S. Mishkat-Ul-Masabih, and D. Feezell, "High-speed nonpolar InGaN/GaN LEDs for visible-light communication," *IEEE Photon. Technol. Lett.*, vol. 29, no. 4, pp. 381–384, Feb. 15, 2017, doi: 10.1109/LPT.2017.2650681.

[3] H.-Y.Lan, I.-C. Tseng, H.-Y. Kao, Y.-H. Lin, G.-R. Lin,and C.-H. Wu, "752-MHz modulation bandwidth of high-speed blue micro light-emitting diodes," *IEEE J. Quantum Electron.*, vol. 54, no. 5, pp. 1–6, Oct. 2018, doi: 10.1109/JQE.2018.2867087.

[4] Y. H. Lin, T. C. Lin, C. H. Cheng, H. C. Kuo, J. J. Huang, and G.-R. Lin, "Photonic crystal structured blue μLED with aperture size dependent data transmission performancein plastic fiber link," *OSA Continuum*, vol. 3, no. 1, pp. 104–119, Jan. 2020, doi: 10.1364/OSAC.378277.

[5] J.-W. Shi, P.-Y. Chen, C.-C. Chen, J.-K. Sheu, W.-C. Lai, Y.-C. Lee, P.-S. Lee, S.-P. Yang, and M.-L. Wu, "Linear cascade GaN-based green light-emitting diodes with invariant high-speed/power performance under high-temperature operation," *IEEE Photon. Technol. Lett.*, vol. 20, no. 23, pp. 1896–1898, Dec. 1, 2008, doi: 10.1109/LPT.2008.2005037.

[6] E. Xie, X. He, M. S. Islim, A. A. Purwita, and J. J. D. Mckendry, "High-speed visible light communication based on a III-nitride series-biased micro-LED array," *J. Lightw. Technol.*, vol. 37, no. 4, pp. 1180–1186, Feb. 15, 2019, doi: 10.1109/JLT.2018.2889380.

[7] J.-W. Shi, K.-L. Chi, J.-M. Wun, J. E. Bowers, Y.-H. Shih, and J.-K. Sheu, "III-nitride-based cyan light-emitting diodes with GHz bandwidth for high-speed visible light communication," *IEEE Electron Device Lett.*,vol.37, no. 7, pp. 894–897,Jul. 2016, doi: 10.1109/LED.2016.2573265.

[8] H. Y. Lan, I. C. Tseng, Y. H. Lin, G. R. Lin, D. W. Huang, and C. H. Wu, "High-speedintegrated micro-LED array for visible light communication," *Opt. Lett.*, vol. 45, no. 8, pp. 2203–2206, Apr. 2020, doi: 10.1364/OL.391566.

[9] S.-C. Zhu, Z.-G. Yu, L.-X. Zhao, J.-X. Wang, and J.-M. Li, "Enhancement of the modulation bandwidth for GaN-based light-emitting diode by surface plasmons," *Opt. Express*, vol. 23, no. 11, pp. 13752–13760, Jun. 2015, doi: 10.1364/OE.23.013752.

[10] K. Rajabi, J. Wang, J. Jin, Y. Xing, L. Wang, Y. Han, C. Sun, Z. Hao, Y. Luo, K. Qian, C.-J. Chen, and M.-C. Wu, "Improving modulation bandwidthof c-plane GaN-based light-emitting diodes by an ultra-thin quantum wells design," *Opt. Express*, vol. 26, no. 19, pp. 24985–24991, Sep. 2018, doi: 10.1364/OE.26.024985.

[11] N. Chi, *Key Devices and Applications of LED Visible Light Communication*, 1st ed. Beijing, China: Post Telecom Press, vol. 2015, ch. 3, sec. 2, p. 61.

[12] M. L. Lucia, J. L. Hernandez-Rojas, C. Leon, and I. Mártil, "Capacitance measurements of p-n junctions: Depletion layer and diffusion capacitance contributions," *Eur. J. Phys.*, vol. 14, pp. 86–89. Sep. 1992, doi: 10.1088/0143-0807/14/2/009.

Influence of Current Density and Capacitance on the Bandwidth of VLC LED

Yong Huang, Zhiyou Guo, Hongyong Huang, and Huiqing Sun

***Abstract*— Visible light communication devices have attracted significant attention recently due to their advantageously high transmission rates. It has been shown that current density and device capacitance has a significant effect on the frequency of visible-light GaN communication devices. We demonstrate a similar linear relationship in a micro-light emitting device (LED) between the −3 dB response frequency, current density, and device diffusion capacity. An experiment was conducted in which, when the device's single light-emitting unit size is between 60–120 μm, increasing the LED current density, the lifetime of the device is substantially reduced for the period of the device's light emission process, and reducing device capacitance improved the device response frequency. To show the relationship between device capacitance and response frequency, four groups of devices with a single unit of the visible GaN communication device was reduced from 120 to 60 μm, the current was set to 35 mA, and the matrix of devices was increased from 1 × 1 to4 × 4, generally, as the numberof series increases, the capacitance decreases. As a result, the −3 dB device response frequency increased from 18 to 74 MHz and luminous efficiency increased from 37 to 74 lm/W, the linear relationship between capacitance and response frequency has been confirmed.**

***Index Terms*— Light-emitting diodes, optical communication, capacitance.**

I. Introduction

VISIBLE light communication (VLC) light emitting devices (LED) are of significant interest due to their security for data communication and high speeds. White LED lights feature high-speed modulation characteristics, enabling the device to simultaneously provide lighting and display to achieve additional functions such as internet communication. The use of white LEDs as a visible light source provides two primary benefits: luminous efficiency and response rate.

Manuscript received January 23, 2018; revised February 20, 2018; accepted March 6, 2018. Date of publication March 8, 2018; date of current version April 6, 2018. This work was supported inpart by theScience and TechnologyProgram Project for the Innovationof Forefront andKey Technology of Guangdong Province, China, under Grant 2014B010119004, Grant 2014B010121001, and Grant 2013B010204065, in part by the Institute of Science and Technology Collaborative Innovation Major Project Guangzhou of Guangdong Province under Grant 201604010047 and Grant 201604010044, and in part by the Special Fund for Scientific and Technological Innovation and Development Guangzhou, Guangdong Province, Foreign Science and Technology Cooperation Project—Graphene electronic paper and its flexible packaging key technology research. *(Corresponding author: Zhiyou Guo.)*

The authors are with the Guangdong Engineering Technology Research Center of Optoelectronic Functional Materials and Devices, Guangzhou 510631, China, also with the Institute of theOpto-Electronic Materials and Technology, South China Normal University, Guangzhou 510631, China, and also with the Guangdong Engineering Research Center of OptoelectronicFunctional Materials andDevices, SouthChina Normal University, Guangzhou 510631, China (e-mail: guozy@scnu.edu.cn).

Color versions of one or more of the figures in this letter are available online at http://ieeexplore.ieee.org.

Digital Object Identifier 10.1109/LPT.2018.2813665

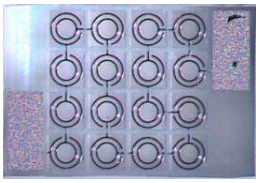

Fig. 1. A prepared LED with the 4×4 micro-LED array.

In addition, improvements have recently been made to the transmission rates for white LED devices [1].

The visible light transmission rate can be improved using an off-the-shelf LED chip (−3 dB with a response frequency of 10-20 MHz) or byoptimizing the transmission system. This allows for data transmission speeds ranging from 1Gbps to several Gbps [2]. The LED modulation bandwidth is the most significant bottleneck in a VLC. Ferreira *et al.* used an LED chip with a 60MHz −3 dB modulation bandwidth, significantly higher than most available LEDs, to achieve a 3Gbps communication speed by orthogonal frequency division multiplexing (OFDM) [3]. LED response frequency can also be improved by optimizing the structural parameters of the device. The micro-LED able to both support communication and illumination base on color shift keying (CSK) modulation [4]. Micro-LEDs have significant potential as a visible light communication device. Kottke *et al.* reported on the use of micro-LEDs, composing a array of individually-addressable 72μm diameter pixels with a center-to-center pitch of 100 μm. These devices were shown to have bandwidths of up to 245 MHz per pixel [2]. The response frequency of micro-LED devices is affected bycarrier lifetime, current density, and capacitance. After analyzing the relationship betweenthese device parameters, we propose a multi-element LED series structure which ensures brightness without affecting device performance. This provides simultaneous improvements in response frequency and optical efficiency. The effects of carrier lifetime and capacitor frequency on the visible optical communication device were studied systematically [5].

II. Experimental Validation

Fig. 1 shows the prepared device (Non-illuminated) for a portion of 4 × 4 micro-LED arrays used in the high-speed Li-Fi communication device, the device is composed by 16 independent light-emitting units, and the light-emitting units are connected inseries by wires. The tworectangles at the two ends are the positive and negative electrodes of the device respectively. Inside ringis the positive electrode and the outside ring is the negativeelectrode, under the positive electrodeare the epitaxial wafer structure layers, which includes ITO (Indium tin oxide), *p*-type layer, the active

layer and n-type layer. The ring electrode facilitates the rapid expansion of the electrons onthe ITO surface, which plays animportant role in improving the response speed of the device. Thetwo sides of the box serve as the anode and cathode electrodes. Four groups including 16 kind of white LEDs with different unit diameters were fabricated. These groups consisted of 1×1, 2×2, 3×3, and4 ×4 micro-LED arrays. Each arrayforms asinglelight-emitting unit with varying diameters of 60, 80, 100, and 120μm. These units wereconnected in seriesto ensure a high output power. In the proposed design, the spacing between individual device lighting areas was increased to 60μm and a copper substrate was included in the working circuit board to enhance the cooling effect. We employed circular electrodes to accelerate the current distribution of N and P poles and the device frequency response. This improved the efficiency of current diffusion and reduced the spontaneous recombination time.

III. Results

Current density and capacitance are the two factors impacting GaN LED −3 dB cut-off frequency. The relationship between frequency response f, carrier lifetime, and current density can be expressed as follows [6]:

$$f_{-3dB} = \frac{1}{2\pi\tau}\sqrt{\frac{BJ}{qd}} \tag{1}$$

In this expression, $f_{-3\mathrm{dB}}$ is the -3 dB cut-off frequency, τ is the carrier lifetime, B is the bimolecular coefficient, J is the injected current density, q is the elementary charge, and d is the thickness of the active layer. Generally, B and d cannot be changed over a wide range. It can be concluded that the relation between the cut-off frequency and the current density is quadratic. Specifically, current density increases with increasing frequency. In addition, we observe an inverse relationship between frequency and carrier life. Since modulation bandwidth is directly proportional to current density, higher currents result in shorter carrier lifetimes for the device. The injection carrier life can be expressed as:

$$\tau = \frac{\Delta n}{R} = \frac{1}{B(P_0 + \Delta n)} \tag{2}$$

Where R is the carrier recombination rate and Δn is the inject excess carrier:

$$\Delta n = \frac{J\tau}{qd} \tag{3}$$

This expression can also be written as:

$$\tau = \frac{-BP_0qd + \sqrt{(BP_0qd)^2 + 4BJqd}}{2BJ} \tag{4}$$

Where P_O is the hole concentration and d is the thickness of the active layer.

From (1) and (4), the cut-off frequency is affected by J and P_0. In the previous study, it was found that the higher the current density and the higher the response frequency [6], the experiments in this letter show that the current density affects the frequency and is present certain conditions.

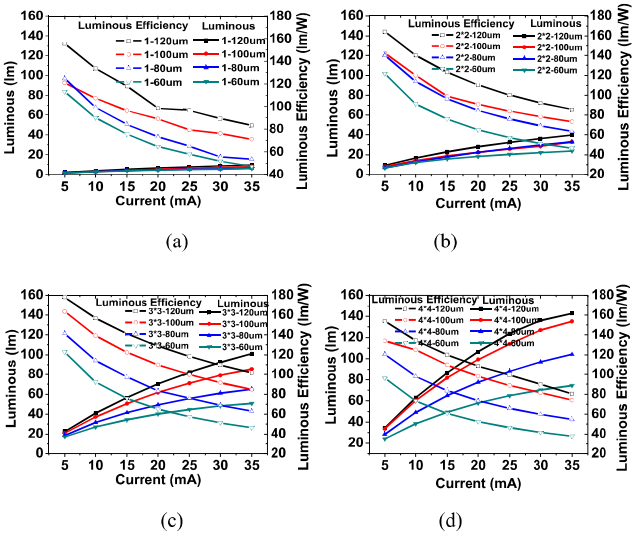

Fig. 2. Four different matriceswith single unit areasof 60, 80, 100, and 120μm, and the resulting light intensity and luminous efficiency for (a) 1×1 micro-LED arrays, (b) 2×2 micro-LED arrays, (c) 3×3 micro-LED arrays, and (d) 4×4 micro-LED arrays.

In addition, the capacitance of the GaN visible light communicationdevice is dividedinto a diffusionand parasitic capacitance. In p-n junction, when the bias voltage superimposed DC and AC voltage, the alternating current will affect the rearrangement of carriers within the device, from another perspective, it will affect the device capacitance. Among them diffusion capacitance and carrier lifetime are directly related [7]:

$$C_{diff} = \frac{qI\tau}{2KT}. \tag{5}$$

In the above expressions, I is the forward bias current across the device, and when the area of the device is fixed, I and J changedsimultaneously. There is acertain correspondence between f and C which is affected by changes in the current density. Larger active areas have a smaller modulation bandwidth at the same current density [8]. This is primarily because the equivalent junction capacitance is larger and the effect of increasing capacitance is more significant on the bandwidth than the effect of reducing the resistance.

Micro-LEDs are of significant importance in visible light communication because a single structure can enhance the total luminous power of the device [9]. In this experiment, four LED groups of varying diameters were selected, forming arrays of 1×1, 2×2, 3×3, and 4×4 to provide a comparison of luminous efficiencyand brightness. Luminous efficiency and power are critical parameters for visible light communication devices. The luminous efficiency of four micro-LEDs decreased as the diameter was gradually reduced from 120 to 60 μm. This is demonstrated at 25 mA in Fig. 2(a)–(d). For example, the luminous efficiency of the 4x4 device was drastically reduced from 96 to 57 lm/W at 25 mA. This is mainlydue to a constant current, area reduction, and a decrease in device efficiency, as shown in Fig. 2(d). At 25 mA, a 4x4 device with a single size of 60 microns can still produce nearly 60 lm.

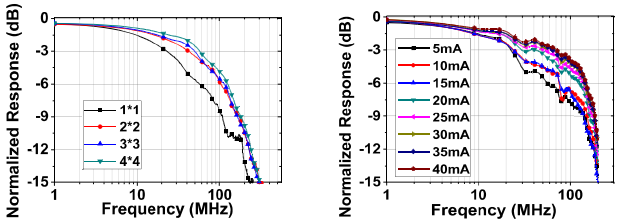

(a) (b)

Fig. 3. (a) Frequency response curves for different matrixtypes, with a diameter of 60μm at a current of 35mA. (b) A 4×4 matrix device structure with a single device size of 60μm, with the corresponding changes in device response frequency and current.

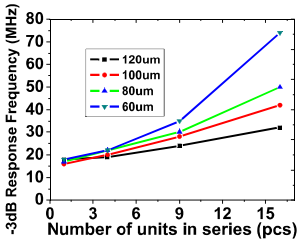

Fig. 4. The 16 micro-LED types used in this study and the corresponding −3 dBresponse frequency data for a current of 40 mA.

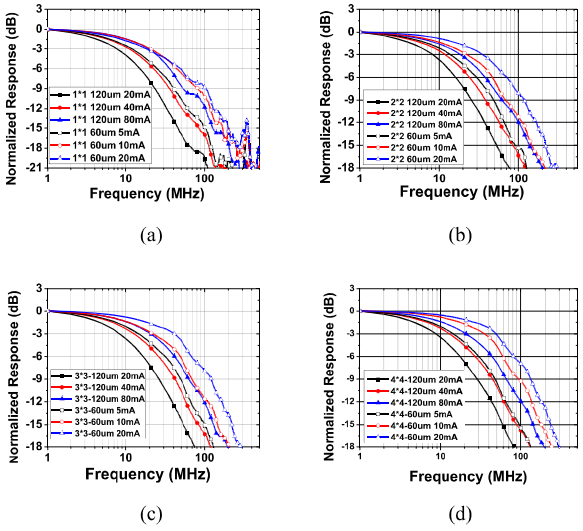

(a) (b) (c) (d)

Fig. 5. Frequency response curves for varying numbers of matrices. The single light emitting unit diameter was 120 μm, the current was 20, 40, and 80 mA. The single light emitting unit diameter was 60 μm for currents of 5, 10, and20 mA. These are shown for a (a) 1 ×1micro-LED array, (b) 2×2 micro-LED array, (c) 3×3 micro-LED array, and a (d) 4×4 micro-LED array.

Fig. 3(a) shows the device frequency response curve for 1×1, 2×2, 3×3, and 4×4 devices with a unit diameter of 60 μm at a current of 35 mA. In the frequency response testing, the input signal which pulse wave source with a peak of ± 0.1V as firstly generated and the transmitted signal was obtained using R&S vector network analyzer. The generated signal was subsequently passed through an amplifier for the purpose of increasing themodulation depth of each LED pixel, whichwas under a DC bias provided by a Keithley 2420 source meter instrument. The amplified signal was then superimposed onto the DC bias current of each pixel via a Pulsar BT-52-400S Bias Tee. The Bias-Tee output was directly supplied to each LED pixel. After the white light from the micro-LED array passes through the filter which the average transmittance of the filter at 380-420nm was 92% and the visible light transmittance of other wavelengths Less than 2%, only remainder blue light in order to avoid the impact of phosphor response and half-life on the frequencyresponse, for the remaining blue light reaches the Newport 818-BB-21A high-speed photo-detector, As seen in the Fig. 3(a), the −3 dB response frequencies for the four devices were 35, 42, 50, and 61 MHz. This indicates the cut-off frequency has a linear relationship with the number of seriesconnections in the device which have the same current density and single device size. This relationship increases the cut-off frequency for the device as the number of tandems increases. Fig. 3(b) shows a device cut-off frequency diagramfor the 4 ×4 array at different currents. Device response frequency increases as the current density increases. At a current density of 40 mA, the device −3 dB cut-off frequency reached 74 MHz, with a brightness of 80 lm and a luminous efficiency of 40 lm/W. This is shown in Fig. 2(d).

Fig. 4 demonstrates this change in −3 dB cut-off frequency for four different constant device sizes at an input current of 40 mA. For example, the 60 μm 3 × 3 matrixdevice with 9 units −3 dB cut-off frequency is 36 MHz. The −3 dB response frequency gradually increased for this group as the number of devices in the series increased. This change is particularly evident with a device size of 60 μm, increasing from 17 to 74 MHz for the 16 series in a 4×4 array. The number of tandem pairs has a significant effect on both thedevice response frequency and thenumber of series. In 4 × 4 matrix device, according to the formula (1), the diameters are 60um and 120um, when the current is 40mA, the current densities differ by 4 and the cutoff frequencies by about 2 times. As the number of devices in a series continued to increase during the same preparation process (i.e., 5×5 or 6×6), the device was unable to pass the set current value of 40 mA given the same parameters, which resulted in device failure.

IV. Discussion

Fig. 5 shows 1×1, 2×2, 3×3, and 4×4 matrixes device series with varying diameters and working currents. The unit diameter of 120μm corresponded with currents of 20 mA, 40 mA, and 80 mA, and the unit diameter of 60μm corresponded with currents of 5 mA, 10 mA, and 20 mA. When the diameter is two times different, the area is 4 times different, so when thedevice with a diameter of 60 μm is 5mA, its current density is equal to the device whose diameter is 120μm, and so on. These figures demonstrates that when the current densities are the same, that is, when the single area is 120μm and the current is 20mA, the as a corresponding area with thesame current density is 60 μm at acurrent of 5mA, the cut-off frequency response curves all exhibit a shift to the right. This corresponds to a higher −3 dB cut-off frequencyvalue, showingbetter frequencyresponse characteristics. For example, as shown in Fig. 5(d), the −3 dB cut-off frequency is was increased from 8, 12, and 18 MHz

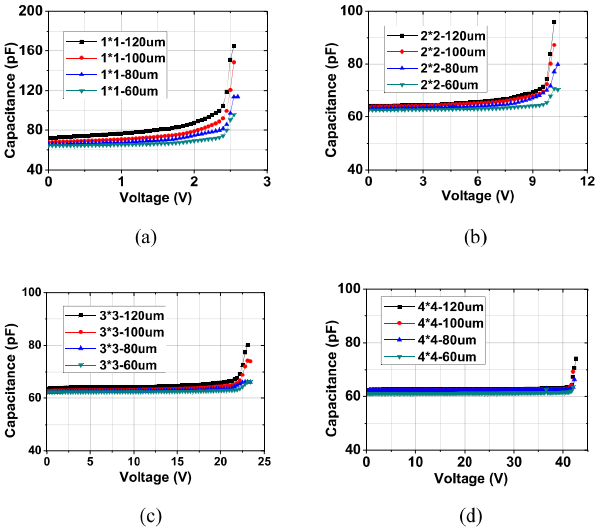

Fig. 6. Device capacitance test results for a (a) 1×1, (b) 2×2, (c) 3×3, and (d) 4×4 matrix structure single light-emitting unit withdiameters ranging from 120 to 60 μm.

to 24, 24.5, and 29 MHz for the same current density for the two kind of devices.

Equation (4) demonstrates the relationship between carrier lifetime, current density, and the cut-off frequency. Experimental results also demonstrate that the carrier lifetime is related to other device factors. In the process of making device changes, the device capacitor cannot be ignored. This is particularly true as the number of series increased from a 1×1 to a 4×4 process. This increase in the light-emitting unit can be regarded as a capacitor series, the total capacitance of which will be reduced by 1/n. We can conclude that the more devices in series, the higher the response frequency. However, as can be seen in Figure 5, different sizes affect the frequency differently. This effect depends on the relationship between the device cut-off frequency and capacitance. The device frequency is mostly affected by the diffusion capacitance.

Device capacitance was tested using a Hewlett Packard 4192A LF impedance analyzer and a signalfrequency of 13 MHz. It can be seen from the Fig. 6 that for a single device, the capacitance decreases from 180 to 80 pF when the individual light emitting diameter decreases from 120 to 60 μm at the appropriate operating voltage. When the voltage is lower than the turn-on voltage, no more carriers are distributed inthe device due to the non-excited state of the device. As a result, less electron holes and diffused capacitance are not displayed. When the voltage continues to increase, Excited, the internal distribution of more electronics, this time a larger capacitor, in order to reduce the impact of capacitance, the use of inductive balance capacitor, and achieved goodresults, the frequencyhas been effectively improved. Epitaxial quantum well structure, electrode shape and other measures can reduce the capacitance, the specific programs to be continued research. The frequency was also increased from 18 to 74 MHz. Devices in series configuration exhibit good data transfer performance, and the data transfer performance of similar device devices is described in [10]. Because of micro-size, relatively close performance and more subtle differences, this letter has not been analyzed. The structure of the epitaxial quantum well and the shape of the electrode can reduce the capacitance. The specific scheme needs to be studied. As the number of devices gradually increased, maximumcapacitances of 165, 96, 80, and 74 pF were achieved for grids of 1×1, 2×2, 3×3, and 4×4, respectively. With the physical structure of the device remaining consistent, and a single light-emitting unit used as a capacitor, an increase in the number of capacitors resulted in a decrease in the overall capacitance of the device.

V. Conclusion

This letter examined the influence of single device size and varying series on the −3 dB response frequency of visible optical communication devices, by adding a series of light-emitting units, increasing the response frequency of the device when the device's single light-emitting unit size is between 60-120 μm, while also increasing the device's luminous power. For a fixed size, increasing the number of series over a certain range had a significant impact onthe response frequency. The impact of different sizes on response frequency was a function of device diffusion capacitance. The influence of current density on the device was analyzed in this study. Current density remained constant for varying sizes. The device also exhibited different response frequency performance. The response frequency of smaller devices can be improved by varying thecurrent density. Theseresults demonstratethe relationship between device capacitance, carrier lifetime, and current density for visible light communication devices.

Acknowledgment

Thanks Liang Xu, Foshan Nation Star Semiconductor Technology Co., Ltd, contribution to this article.

References

[1] J. Vucic, C. Kottke, S. Nerreter, K.-D. Langer, and J. W. Walewski, "513 Mbit/s visible light communications link based on DMT-modulation of a whiteLED," *J. Lightw. Technol.*, vol. 28, no. 24, pp. 3512–3518, Dec. 15, 2010.

[2] C. Kottke *et al.*, "Single-channel wireless transmission at 806 Mbit/s using a white-light LED and a PIN-based receiver," in *Proc. ICTON*, Jul. 2012, pp. 1–4, paper We.B4.1.

[3] R. X. G. Ferreira *et al.*, "High bandwidth GaN-based micro-LEDs for multi-Gb/s visible light communications," *IEEE Photon. Technol. Lett.*, vol. 28, no. 19, pp. 2023–2026, Oct. 1, 2016.

[4] S. Pergoloni, M. Biagi, S. Rinauro, S. Colonnese, R. Cusani, and G. Scarano, "Merging color shift keying and complementary pulse position modulation for visible light illumination and communication," *J. Lightw. Technol.*, vol. 33, no. 1, pp. 192–200, Jan. 1, 2015.

[5] J. J. D. McKendry *et al.*, "High-speed visible light communications using individual pixels in a micro light-emitting diode array," *IEEE Photon. Technol. Lett.*, vol. 22, no. 18, pp. 1346–1348, Sep. 15, 2010.

[6] C. Du *et al.*, "Tuning carrier lifetime in InGaN/GaN LEDs via strain compensation for high-speed visible light communication," *Sci. Rep.*, vol. 6, Nov. 2016, Art. no. 37132.

[7] M. L. Lucia, J. L. Hernandez-Rojas, C. Leon, and I. Mártil, "Capacitance measurements of p-n junctions: Depletion layer and diffusion capacitance contributions," *Eur. J. Phys.*, vol. 14, pp. 86–89, Jan. 1999.

[8] C.-L. Liao, C.-L. Ho, Y.-F. Chang, C.-H. Wu, and M.-C. Wu, "High-speed light-emitting diodes emitting at 500 nm With 463-MHz modulation bandwidth," *IEEE Electro. Devic. Lett.*, vol. 35, no. 5, pp. 563–565, May 2014.

[9] D. Tsonev, "A3-Gb/s single-LED OFDM-based wireless VLC link using a gallium nitride μLED," *IEEE Photon. Technol. Lett.*, vol. 26, no. 7, pp. 637–640, Apr. 1, 2014.

[10] Y. Huang, Z.-Y. Guo, H.-Q. Sun, and H.-Y. Huang, "Micro-light-emitting-diode array with dual functions of visible light communication and illumination," *Chin. Phys. B*, vol. 26, no. 10, p. 108504, Oct. 2017.

Micro-light-emitting-diode array with dual functions of visible light communication and illumination*

Yong Huang(黄涌)[1,2,3], Zhi-You Guo(郭志友)[1,2,3,†], Hui-Qing Sun(孙慧卿)[1,2,3], and Hong-Yong Huang(黄鸿勇)[1,2,3]

[1] *Guangdong Provincial Key Laboratory of Nanophotonic Functional Materials and Devices, Guangzhou* 510631, *China*
[2] *Institute of the Opto-Electronic Materials and Technology, South China Normal University, Guangzhou* 510631, *China*
[3] *Guangdong Engineering Technology Research Center of Optoelectronic Functional Materials and Devices, Guangzhou* 510631, *China*

(Received 3 April 2017; revised manuscript received 9 July 2017; published online 20 August 2017)

We demonstrate high-speed blue 4×4 micro-light-emitting-diode (LED) arrays with 14 light-emitting units (two light-emitting units are used as the positive and negative electrodes for power supply, respectively) comprising multiple quantum wells formed of GaN epitaxial layers grown on a sapphire substrate, and experimentally test their applicability for being used as VLC transmitters and illuminations. The micro-LED arrays provide a maximum −3-dB frequency response of 60.5 MHz with a smooth frequency curve from 1 MHz to 500 MHz for an optical output power of 165 mW at an injection current of 30 mA, which, to our knowledge, is the highest response frequency ever reported for blue GaN-based LEDs operating at that level of optical output power. The relationship between the frequency and size of the device single pixel diameter reveals the relationship between the response frequency and diffusion capacitance of the device.

Keywords: light-emitting devices, optical communications, diffusion capacitance

PACS: 85.60.Jb, 42.79.Sz, 84.37.+q **DOI:** 10.1088/1674-1056/26/10/108504

1. Introduction

Light-emitting-diodes (LEDs) are key transmitter components for light fidelity (Li–Fi) communication networks by using plastic optical fibers (POFs)[1] or visible light communication (VLC) systems due to their relatively low complexity and low cost, and market dominance. They have incomparable advantages in particular environments, such as underwater communication, traffic safety data transmission, indoor environments,[2] and secure communication, and potential applications in implementing wireless communications in environments where radio communication is impossible.[3,4] The use of diverse structures and materials for visible-light LEDs has received considerable attention, and the study of their performances has made significant progress.[5,6] Appropriate device size, the employment of advanced epitaxial materials, and optimum pixel arrangement are the areas of concern in VLC chip development. Micro-LEDs, which are high-density micrometer-sized LED arrays, have aroused the considerable interest in being used as transmitter devices in VLC systems[7] because the structure not only offers numerous benefits such as low power consumption, small size, and long life, but also provides the rapid response conditions required by communication systems. Shi *et al.*[8,9] demonstrated linear cascade arrays of GaN-based LEDs, which were modulated by using a resonant driving technique, resulting in an overall bandwidth of 90 MHz. Arrays of four LEDs provided around four times the optical output power of a single LED, with a maximum output power near 20 mW. McKendry *et al.*[10] evaluated a series of micro-LEDs with different pixel diameters, and concluded that micro-LED pixels with smaller areas generally provide higher modulation bandwidths than those with larger areas, which was attributed to the ability of small-area pixels to be driven at higher current densities. The high-frequency modulation of individual pixels in 8×8 arrays of III-nitride-based micro-pixellated LEDs, where the pixel diameters ranged from 14 μm to 84 μm, were reported. The arrays were driven with a complementary metal–oxide–semiconductor (CMOS) driver array chip, which allowed for simple computer control of the individual micro-LED pixels. The highest optical −3-dB modulation bandwidth from these LED devices was shown to be in excess of 400 MHz, and a maximum output power of about 5 mW was obtained. Liao *et al.*[11] reported on high-speed GaN-based green LEDs with an aperture diameter of 75 μm, and obtained a maximum optical −3-dB modulation bandwidth of 463 MHz at a current of 50 mA. The LED device exhibited a relatively high optical output power of 1.6 mW. For enhancing the diffusion velocity of electrons, a new conductive material was utilized as a top transparent conductive layer. Liao *et al.*[12] later reported on high-speed GaN-based blue LEDs with an aperture diameter of 75 μm, which exhibited a −3-dB modulation bandwidth of 225.4 MHz and an optical output power of 1.6 mW. The researchers employed

*Project supported by the Science and Technology Program Project for the Innovation of Forefront and Key Technology of Guangdong Province, China (Grant Nos. 2014B010119004, 2014B010121001, and 2013B010204065), the Institute of Science and Technology Collaborative Innovation Major Project of Guangzhou City, Guangdong Province, China (Grant No. 201604010047), the Special Project for Key Science and Technology of Zhongshan City, Guangdong Province, China (Grant No. 2014A2FC204), and the Fund from the Huadu Science and Technology Bureau of Guangdong Province, China (Grant No. HD15PT003).

†Corresponding author. E-mail: guozy@scnu.edu.cn

InSnO/Ga-doped Zn oxide (ITO/GZO) or a GZO contact layer deposited by sputtering as a current-spreading layer to enhance the optical output powers of GaN/InGaN LEDs.

Device dimension has also been shown to play a key role in providing optimal LED transmitter device performance. While the decreased size allows for higher frequency operation, the smaller size also leads to a decreased optical output power.[13] In addition, because the sidewall heat radiation is increased with pixel size decreasing, the ohmic contact and the PN junction can be destroyed by over-heating, resulting in overall device failure.[14] Different device structures have also been reported in previous studies, such as heterojunction bipolar LEDs (HBLEDs), which have been utilized as a high-speed LED structure.[14] This device structure allows the distribution of electrons to be altered during the device working cycle, and, owing to the increased operational frequency of the device, a high-speed -3-dB bandwidth of greater than 1 GHz can be obtained. As the size decreases, the current density increases; Walter *et al.*[15] demonstrated a large frequency modulation bandwidth of 524 MHz at a current density of 10 kA/cm^2

In this paper, we demonstrate high-speed blue 4×4 micro-LED arrays (two light-emitting units are used as the positive and negative electrodes for power supply) comprising multiple quantum wells (MQWs) formed of GaN epitaxial layers grown on a sapphire substrate, and experimentally test their applicability for being used as VLC transmitters. The proposed transmitter device (14 light emitting units) achieves a maximum -3-dB frequency response of 60.5 MHz without driver or modulation circuit, and a smooth frequency curve from 1 MHz to 500 MHz is obtained for an optical output power of 11.7 mW for each single unit, and reaches 165 mW for whole chip at an injection current of 30 mA with an active area diameter of 60 μm for single light emitting unit, which, to our knowledge, is the highest bandwidth ever reported for blue GaN-based LEDs operating at that level of optical output power. As is well known, the optical output power has a significant practical influence on transmitter device performance in a VLC system. We also demonstrate that LEDs with smaller mesa areas generally exhibit higher modulation bandwidths than LEDs with large mesa areas, which is attributed to their ability to be driven at higher current density. The bandwidth is set to be 250 MHz in our experiment. Therefore, an aggregate data rate of 1.375 Gbit/s is successfully demonstrated by using bit and power loading orthogonal frequency division multiplexing (OFDM) with the bit error rate (BER) of 3.3×10^{-3} under the forward-error-correction (FEC) limit of 3.8×10^{-3}.

2. Experiment

2.1. Device preparation

Four groups of blue LEDs with different unit mesa diameters were fabricated, where each LED consisted of 4×4 micro-LED arrays (two light-emitting units are used as the positive and negative electrodes for power supply respectively). These units were connected in series to ensure a high output power. Figure 1 shows the LED transmitter device mounted on a circuit board. As the size of a single device unit decreases, a high density of current will cause heat to increase. In the design of the device, the spacing between the individual devices in the lighting area was increased to 60 μm, and copper substrate was used in the working circuit board for enhancing the cooling effect. The epitaxial layers of the LEDs wafers were grown by metal–organic chemical vapor deposition (MOCVD). To ensure high response and high brightness, these layers were: 1) an 800-nm thick undoped GaN buffer layer, 2) a 3000-nm thick n$^+$-GaN confinement layer, 3) an MQW active region consisting of fourteen 3-nm thick $In_{0.25}Ga_{0.75}N$ quantum wells separated by thirteen GaN barrier layers, specifically, a GaN barrier layer is sandwiched between the two adjacent $In_{0.25}Ga_{0.75}N$ quantum wells, 4) a 20-nm thick p-$Al_{0.1}Ga_{0.9}N$ confinement layer, 5) a 100-nm thick p-GaN capping layer, and 6) a 110-nm thick ITO film deposited by magnetron sputtering. After conducting epitaxial growth, the LED devices were fabricated using standard processing techniques, including sample cleaning, photolithography and metallization, lapping, polishing, scribing, and bonding. In the photolithography process, the wafer was divided into a 4×4 array of pixels of equal size (with sizes varying from 60 μm to 120 μm), and a multilayer

(a)

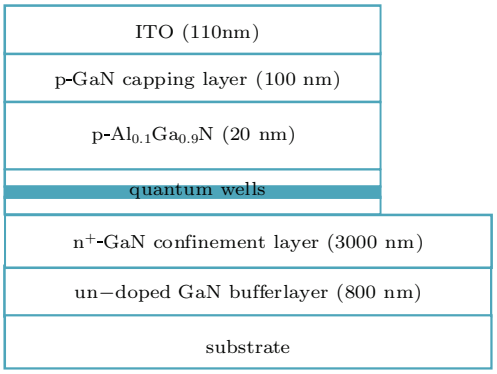

(b)

Fig. 1. (color online) (a) The LED transmitter device mounted on a circuit board, and (b) schematic diagram of visible light communication LEDs.

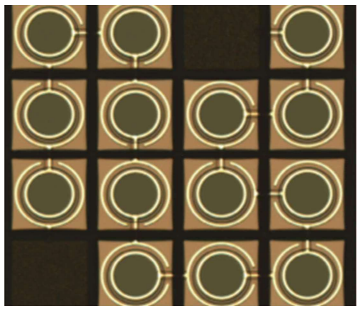

Fig. 2. (color online) 4×4 high-speed light fidelity communication light-emitting diode structure image after metal wire has been deposited on p-GaN prior to the silicon oxide passivation layer deposition, observed by optical microscopy, and two dark square areas are the position of the metal wire.

metal conductive coating consisting of Cr/Al/Cr/Ti/Al with respective thickness values of 20/2000/250/450/20000 nm was applied. Connected between pixels is a conductive metal wire. Prior to depositing a metal wire, a SiO_2 layer was deposited on the area where the metal wire must pass through a deep erosion channel to ensure that the wire properly connects two neighboring pixels. To accelerate the current distributions of the N and P poles, and thereby accelerate the frequency response characteristics of the device, we employed circular electrodes, which can improve the efficiency of current diffusion and shorten the spontaneous recombination time. Figure 2 shows an optical microscopy image of a portion of a 4×4 micro-LED array designed for high-speed Li–Fi communication after conductive metal wire deposition on the p-GaN capping layer, but prior to SiO_2 passivation layer deposition. The two dark square areas are the positions of the metal wire. Simulations have shown that circular p-electrodes can effectively improve the current distribution inside the device, and it was useful for improving the frequency response of the device.

2.2. Measurement system

The experimental system and procedure are shown in Fig. 3. The LED optical data transmission performance testing was conducted as follows. The input signal was first generated using a Tektronix 7122C arbitrary waveform generator (AWG). The generated signal was subsequently passed through an amplifier for the purpose of increasing the modulation depth of each LED pixel, which was under a DC bias provided by a Keithley 2420 source meter (SMU) instrument. The amplified signal was then superimposed onto the DC bias current of each pixel via a Pulsar BT-52-400S Bias Tee. The maximum operating voltage of the amplifier (Coaxial ZHL-32A) is 24 V. In this experiment, the input signal voltage is 0.3 V. It is also found that the signal inputs with different voltages and the response frequencies are the same. The Bias-Tee output was directly supplied to each blue LED pixel. Light from the blue micro-LED array was imaged onto a Newport 818-BB-21A high-speed photo-detector consisting of an avalanche photodiode (APD), and the transmitted signal was obtained using a high numerical aperture (NA) Tektronix DSO 73304D oscilloscope. The received signal was then displayed and analyzed via a computer using MATLAB software.

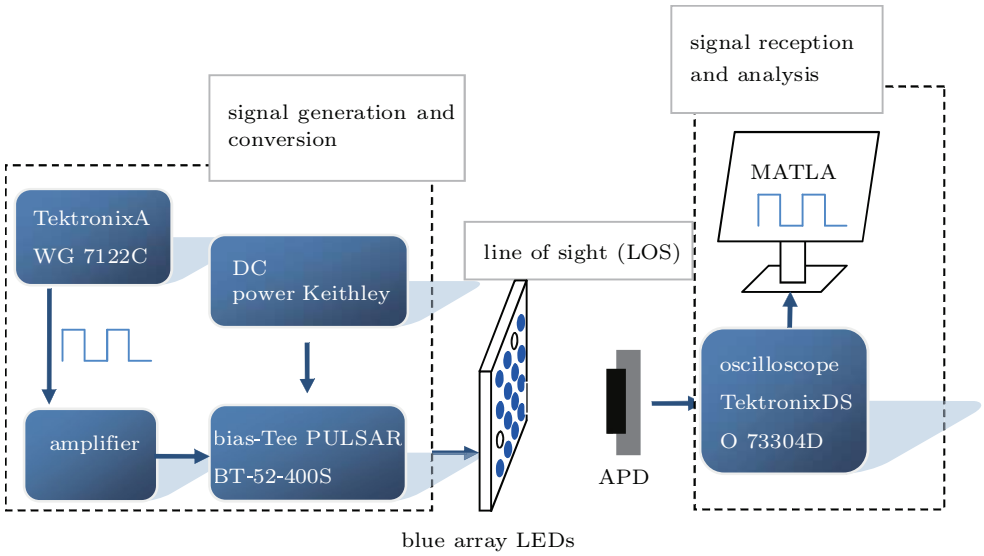

Fig. 3. (color online) Experimental setup of the VLC-LED measurement system composed of an arbitrary waveform generator (AWG), a bias tee to overlay the amplified signal with the DC bias current provided by a source meter (SMU) instrument, and an avalanche photodiode (APD) as a high-speed photo-detector.

3. Results and discussion

As is well known, the frequency response of an LED is mainly limited by its diffusion capacitance[16] and carrier lifetime, and the number of injected carriers in the active region of the device; of course, there are links between these three factors. For all sizes of LEDs, the corresponding frequency response increases significantly as the injected current increases, which results in carriers lifetime shortening. In addition, the

injected carrier density in the active region increases with increasing current injection.

$$f_{-3\ \mathrm{dB}}=\frac{1}{2\pi\tau}\sqrt{\frac{BJ}{qd}}, \tag{1}$$

where B is the bimolecular coefficient, J the injected current density, q the elementary charge d the thickness of the active region, and τ the carrier lifetime.

In addition to the effect of carrier lifetime, the capacitance is also an important factor limiting LED bandwidth. In the LED device, the capacitance is divided into parasitic capacitance and diffusion capacitance, in which the diffusion capacitance and carrier life are related to each other.

The diffusion capacitance

$$C_{\mathrm{D}}=\frac{qI}{kT}\tau, \tag{2}$$

where I is the current of the device, q is the elementary charge, k is the Boltzmann constant, T is the absolute temperature, τ is the carrier lifetime.

The device parasitic capacitance is

$$C_{\mathrm{T}}=A\frac{\varepsilon_{\mathrm{s}}}{\chi}, \tag{3}$$

where A is the junction area, C_{T} is dependent on the characteristics of the device ε_{s} the dielectric constant of the semiconductor, χ is the depletion layer width related to the bias of the p–n junction.

Therefore, the current density of the device, carrier life, the device diffusion capacitance, and the device response frequency have a direct relationship.

Figure 4 shows the I–V characteristics of LEDs with mesa diameters ranging from 60 μm to 120 μm. From the I–V characteristics, it can be observed that the smaller diameter mesa areas tend to have higher turn-on voltages and work voltages than their larger counterparts, which may be attributed to the relatively great laser dry-etching induced damage and/or poor p-contact quality.

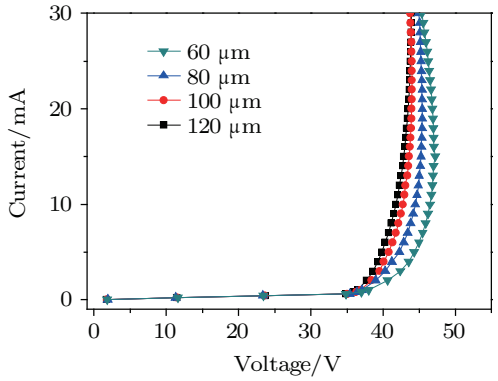

Fig. 4. (color online) I–V characteristics of LEDs with different mesa diameters.

Figure 5 shows the optical output power of LED arrays as a function of the forward current (L–I) measured at room temperature for the LEDs with different mesa diameters. The optical output power values measured by HAAS-2000 (EVERFINE) at a 30-mA injection current are 356, 305, 275, and 165 mW for the LEDs with mesa diameters of 120, 100, 80, and 60 μm, respectively. We see that the output power of the device decreases as the device dimension decreases because the effective area of the LED device decreases. The device luminous efficiency decreases mainly due to the current density increasing caused by the droop effect of the device. In order to reduce the influence of this effect on the device, in the experiment a ring electrode is used as shown in Fig. 6, so that the current distribution in the device is in equilibrium.

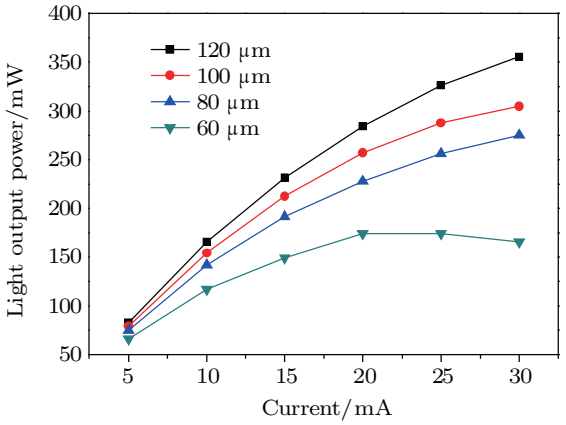

Fig. 5. (color online) Optical output powers of LEDs with different mesa diameters.

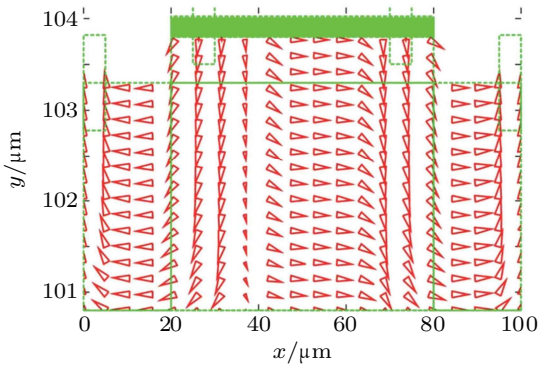

Fig. 6. (color online) Current distribution in cross-section of the ring electrode device.

Figure 7 shows the room-temperature electroluminescence (EL) spectra of the LED with a 60-μm mesa diameter under various injection currents. Each of the LEDs investigated provides a peak emission wavelength of around 450 nm. A slight red shift is observed with increasing injection current due to the quantum confined Stark effect (QCSE) in the MQW layer. As discussed previously, the sidewall heat radiation increases with reducing pixel size, and the ohmic contact and the PN junction may be destroyed due to excessive heating. In addition, an increasing junction temperature will lead to more of the active layer and stronger non-carrier leakage radiation. Finally, an increasing junction temperature also affects the EL spectrum of the LED.

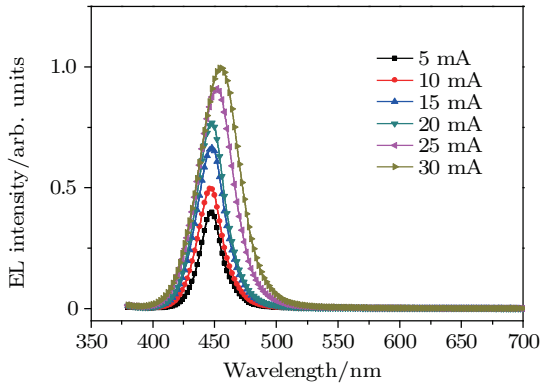

Fig. 7. (color online) Room-temperature electroluminescence (EL) spectra under various injection currents for an LED with a mesa diameter of 60 μm.

Figure 8 shows the frequency response of the LED with a mesa diameter of 60 μm at different injection currents. For injection currents of 5 mA, 10 mA, 15 mA, 20 mA, 25 mA, and 30 mA, the values of $f_{-3\ \mathrm{dB}}$ obtained are 25 MHz, 43.7 MHz, 51.2 MHz, 55.1 MHz, 58.3 MHz, and 60.5 MHz, respectively. With increasing current density in LED device, τ decreases, and hence, $f_{-3\ \mathrm{dB}}$ increases. From the measured values of $f_{-3\ \mathrm{dB}}$, it can be concluded that $f_{-3\ \mathrm{dB}}$ is proportional to the square root of the current density and we see that $f_{-3\ \mathrm{dB}}$ and τ exhibit an inversely proportional relationship. According to Eq. (2), for the device current increasing, the capacitance and current which are proportional to the response frequency should also increase proportionally, but the experimental results indicate that when the current increases, the response frequency increases only to a certain extent, especially when the current increases to a certain value such as 20mA. When the current continues to increase to a certain percentage, the response frequency has a smaller increase, so it can be found that the current grows to a certain extent, the device diffusion capacitance has a significant effect on device frequency.

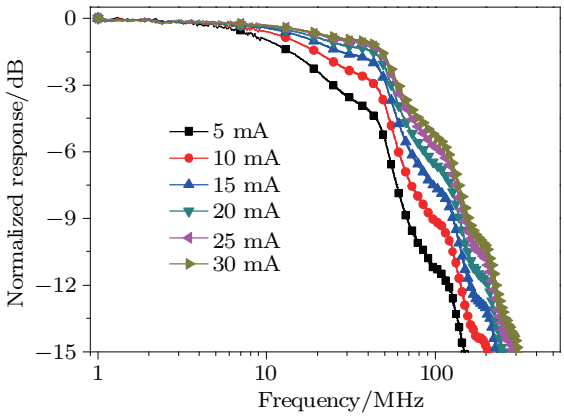

Fig. 8. (color online) Frequency response measured at different injection currents for an LED with a mesa diameter of 60 μm.

Figure 9 shows the frequency responses in linear and logarithmic graphs (the inset) measured at an injection current of 20 mA for LEDs with mesa diameters ranging from 60 μm to 120 μm. For mesa diameters of 60, 80, 100, and 120 μm, the values of $f_{-3\ \mathrm{dB}}$ obtained are 55.1, 42.2, 24.8, and 18.4 MHz, respectively. The maximum −3-dB response frequency curves obtained from the devices are smooth, which are suitable for the application to high-speed VLC systems.

According to Eq. (1), with other factors unchanged, only changing the area of the device, that is, only changing the current density, current per unit area, the frequency ratio of the four devices should be 20:15:12:10. As a result of the test, the response frequency of the four devices is approximately 30:23:13:10 in the same current condition. The difference between them is greater than the difference between the calculated results according to Eq. (1), so we can confirm that the relationship between the frequency and size of the device single pixel diameter reveals the relationship between the response frequency and diffusion capacitance of the device.

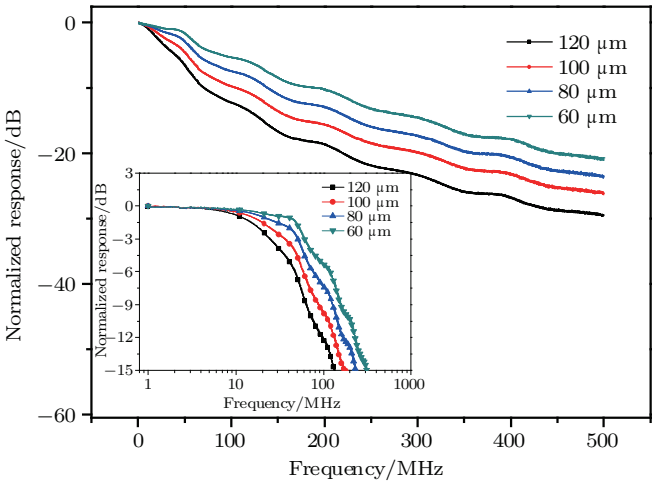

Fig. 9. (color online) Frequency response curves measured at an injection current of 20 mA for LEDs with different mesa diameters. The inset presents the values of $f_{-3\ \mathrm{dB}}$ and the current density obtained at an injection current of 20 mA for different LED pixel diameters.

4. Conclusions and perspectives

In this paper, we demonstrate high-speed blue micro-LED arrays comprising MQWs formed of GaN epitaxial layers grown on a sapphire substrate, and experimentally test their applicability for being used as VLC transmitters and illuminations. The device with 14 pixels achieves a maximum −3-dB frequency response of 60.5 MHz and a smooth response frequency curve from 1 MHz to 500 MHz for an optical output power of 165 mW at an injection current 30 mA. The device performance verifies its applicability to high-speed VLC systems. To the best of our knowledge, the proposed device provides the highest −3-dB frequency response and modulation bandwidth in all ever reported blue GaN-based LEDs operating at that level of optical output power. Smaller mesa area LEDs generally exhibit higher modulation bandwidths than larger mesa area LEDs, which is attributed to their ability to be driven at higher current densities, and the effect of the diffusion capacitor plays an important role in the response frequency of the device. We conclude that the relationship be-

tween the frequency and size of the device (i.e., single pixel diameter) reveals the relationship between the response frequency and diffusion capacitance of the device.

Acknowledgments

The authors are grateful for the support of Drs. Jintian Zhu and Liang Xu, Foshan Nation Star Semiconductor Technology Co., Ltd and the authors would like to thank Guangdong Engineering Research Center of Optoelectronic Functional Materials and Devices support for the program.

References

[1] Shi J W, Sheu J K, Chen C H, Lin G R and Lai W C 2008 *IEEE Electron Dev. Lett.* **29** 158
[2] Harilaos S, Alexander V, Theodoros T and Nicholas V 2017 *Appl. Opt.* **56** 3421
[3] MckendryJ D, GreenR P, Kelly A E, Gong Z, Guilhabert B, Massoubre D, Gu E and Dawson M D 2010 *IEEE Photon. Technol. Lett.* **22** 1346
[4] Haruyama S 2012 European Conference and Exhibition on Optical Communication OSA Technical Digest (online), November 30, 2012, paper We.3.B.5
[5] Arman R, Morteza M, Andrew A, Serdal O, Mohsen N, Ashwin R, Saadat M and Daniel F 2017 *Photon. Technol. Lett.* **29** 381
[6] Li S, Pandharipande A and Willems M J 2017 *IEEE Trans. Commum.* **65** 740
[7] McKendry J J D, Massoubre D, Zhang S L, Rae B R, Green R P, Gu E, Henderson R K, Kelly A E and Dawson M D 2012 *J. Lightw. Technol.* **30** 61
[8] ShiJ W, Sheu J K, Wang C K, Chen C C, Hsieh C H, ChyiJI and Lai W C 2007 *IEEE Photon. Technol. Lett.* **19** 1368
[9] ShiJ W, Chen P Y, Chen C C, Sheu J K, Lai W C, Lee Y C, Lee P S, Yang S P and Wu M L 2008 *IEEE Photon. Technol. Lett.* **20** 1896
[10] McKendry J J, Massoubre D, Zhang S, Rae B R, Green R P, Gu E, Henderson R K, Kelly A E and Dawson M D 2012 *IEEE J. Lightw. Technol.* **30** 61
[11] Liao C L, Ho C L, Chang Y F, Wu C H and Wu M C 2014 *IEEE Electron Dev. Lett.* **35** 563
[12] Liao C L, Chang Y F, Ho C L and Wu M C 2014 *IEEE Electron Dev. Lett.* **34** 611
[13] Qian H, Zhao S, Cai S Z and Zhou T 2015 *IEEE Photon. J.* **7** 7901508
[14] Schubert E F 2008 Light Emitting Diodes, 2nd edn. (Cambridge: Cambridge University Press) p. 103
[15] Walter G, WuC H, ThenH W, Feng M and Holonyak N 2009 *Appl. Phys. Lett.* **94** 241101
[16] Wang X H, Zhao M, Liu X Y, Pu Y, Zheng Y K and Wei K 2010 *Chin. Phys. B* **19** 097302

ACS APPLIED MATERIALS & INTERFACES

www.acsami.org

Research Article

Storage Mechanism of Alkali Metal Ions in the Hard Carbon Anode: an Electrochemical Viewpoint

Yong Huang,* Yuqing Wang, Panxing Bai, and Yunhua Xu*

Cite This: *ACS Appl. Mater. Interfaces* 2021, 13, 38441−38449

Read Online

ACCESS | Metrics & More | Article Recommendations | Supporting Information

ABSTRACT: The storage mechanisms of Li, Na, and K in hard carbon anodes are investigated through systematically exploring their electrochemical behaviors. Two charge/discharge voltage regions are observed for all the Li, Na, and K storage, a slope at a high voltage, and a plateau in a low-voltage range. Considerably different behaviors are revealed by the galvanostatic intermittent titration technique and electrochemical impedance spectroscopy measurements, and accordingly different storage mechanisms are proposed. The sloping region is mainly attributed to the adsorption at defects/heteroatoms for all the Li, Na, and K storage. In the plateau region, pore filling contributes very little to Li storage but much to Na and K storage. Furthermore, significant effects of ionic sizes on the storage behavior in hard carbons are revealed by the electrochemical performance from Li to Na to K. These findings not only offer a fundamental understanding of storage mechanisms of alkali metal ions in hard carbons but also help develop and design innovative electrode materials for low-cost and large-scale energy storage systems.

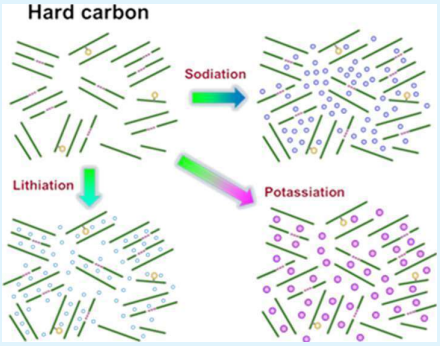

KEYWORDS: *potassium-ion battery, sodium-ion battery, hard carbon anode, micropore filling, intercalation*

INTRODUCTION

The fast increasing demand for large-scale energy storage systems has raised great concerns over Li-ion batteries (LIBs) in terms of affordability and cost due to the limited and unevenly distributed lithium resources in the Earth's crust.[1] Therefore, new energy storage technologies that use earth-abundant and nontoxic materials are urgently desired to enable low cost and high-performance power devices for large-scale applications.

Sodium- and potassium-ion batteries (NIBs and KIBs),[2−36] as alternative energy storage systems to LIBs, have recently attracted considerable attention because of their massive reserves, wide distribution, and nontoxicity of sodium and potassium, as well as the similarity in chemical and physical properties to those of lithium. Significant advancements have been made in sodium storage materials. In particular, encouraging performance has been achieved in cathode materials of NIBs, such as metal oxides,[2,6,7,20,37] phosphates,[3,14,38,39] sulfides,[9,40−43] and organic materials.[43−46] The biggest challenge for NIBs lies in the anode side due to the poor activity of sodium intercalation into graphite,[4,48] a standard anode in commercial LIBs. Hard carbon, as a promising anode for sodium, is capable of delivering capacities of ∼300 mA h/g, comparable to those of the graphite anode in LIBs.[4,17,18,49] However, the poor kinetics and ultra-low reaction potential (<0.1 V) of sodium storage in hard carbons cause poor rate capability and high fire hazards, which may diminish its resource merit for future applications.[47] Therefore, a more efficient material design is needed for high-performance Na storage.

In contrast to sodium, potassium can be intercalated into graphite to form potassium−graphite intercalated compounds (GICs).[48] Electrochemically reversible intercalation of potassium into graphite has been demonstrated in KIBs.[16−19] Although a moderate reversible capacity of ∼240 mA h/g was reported for the graphite anode, the sluggish kinetics leaves a poor rate capability due to the large radius of K ions.[28,29,33,50] Recently, enhanced performance was obtained on hard carbon anodes in KIBs.[51,52] Particularly, superior rate capability was reported for hard carbon anodes in KIBs than NIBs, with a high capacity retention of 73% at 2 C in the former *versus* only 30% in the latter. Electrospun carbon nanofibers also demonstrated an extremely high rate capability with a retention of 100 mA h/g at a high current rate of 7.7 A/g and a very low decay rate of 0.01% per cycle over 1200 cycles, which are much better than those in sodium-ion batteries.[53] These results show that hard carbon anodes have different storage mechanisms and behaviors in LIBs, NIBs, and KIBs.

Received: June 29, 2021
Accepted: July 23, 2021
Published: August 3, 2021

The storage of alkali metal ions in hard carbon is very complicated due to the diverse structures of hard carbon.[54] Hard carbon has an amorphous structure that comprises abundant defects, edges, and functional groups, numerous randomly aligned graphene sheets and graphitic microcrystals, and a vast amount of micropores, which provide various active storage sites. Different storage mechanisms have been proposed, including adsorption on defects, edges, and functional groups, intercalation into graphitic layers, and filling into micropores.[54−68] Recently, though much effort was focused on materials structure modification and characterization to improve the Na storage efficiency,[56−62] controversial Na storage behaviors were reported,[54−68] showing that it is still a great challenge to achieve a comprehensive understanding. The lack of a fundamental understanding of the storage mechanism undoubtedly plagues the design and development of hard carbon electrode materials for high-performance NIBs and KIBs.

In this paper, the energy storage mechanisms of Li, Na, and K in hard carbon anodes were systematically investigated based on electrochemical analysis. Considerably different electrochemical processes and performances were revealed by the charge/discharge profiles, galvanostatic intermittent titration technique (GITT), and electrochemical impedance spectroscopy (EIS) measurements. The cycling stability and rate capability become better and the voltage hysteresis between charge/discharge processes becomes smaller from Li to Na to K, suggesting a dependent relationship of the storage behavior on the alkali metal ions. Accordingly, different storage mechanisms were proposed for Li, Na, and K in hard carbons.

EXPERIMENTAL SECTION

Materials. Sucrose (>99.5%), $LiPF_6$ (>99.99%), $NaPF_6$ (98%), KPF_6 (99.5%), ethylene carbonate (EC, 99%), propylene carbonate (PC, 99.7%), sodium metal (99.8%), potassium metal (99.5%), and lithium metal (99.9%) were purchased from Sigma-Aldrich, USA. Sucrose (99.9%) was bought from J & K, China, and sulfuric acid (98%) was purchased from Sinopharm Chemical Reagent Co., Ltd., China. All the chemicals were used as received.

Synthesis of Hard Carbon. The hard carbon was prepared according to a previously reported method.[72] Typically, pure sulfuric acid was diluted to form a 6 M solution using distilled water. Then, 20 g of sucrose was dissolved in 6 M sulfuric acid to form 5% sucrose solution. After refluxing in a 1 L round-bottom flask at 120 °C overnight, a product with a brown color was collected by filtering and washing with distilled water several times. After drying at 100 °C for 24 h in a vacuum oven, the product was carbonized at 1000 °C for 3 h in an argon atmosphere with a heating rate of 5 °C/min.

Material Characterization. Scanning electron microscopy (SEM) and transmission electron microscopy (TEM) images were taken by a Hitachi TDCLS-4800 scanning electron microscope (Japan) and a JEOL (Japan) 2100F field-emission tranmsission electron microscope, respectively. X-ray diffraction (XRD) data were recorded with a Bruker D8 Advanced (Bruker AXS Inc., USA) using Cu Kα radiation. Raman measurements were performed on a Horiba Jobin Yvon Labram Aramis using a 532 nm diode-pumped solid-state laser, attenuated to give ~900 μW power at the sample surface. The porous structure of the microporous carbon was analyzed using CO_2 (at 273 K) adsorption on an Autosorb-iQ MP (Quantachrome Instruments, USA).

Electrochemical Measurement. Electrodes were prepared by mixing the hard carbon with carbon black and sodium alginate binder to form a slurry at a weight ratio of 80:10:10, which was cast onto a Cu foil using a doctor blade and dried in a vacuum oven at 60 °C overnight, forming films at a thickness of ~10 μm. The mass loading of the active material was ~1 mg/cm^2. Coin-type batteries were assembled with Li, Na, and K metals as the counter electrodes; 1 M $LiPF_6$, 1 M $NaPF_6$, and 0.8 M KPF_6 in EC/PC (1:1 by volume) as electrolytes for Li-ion, Na-ion, and K-ion batteries, respectively; and Celgard2400 (Celgard, LLC Corp., USA) as separators. Electrochemical performance was tested using Land battery test stations (CT2001A, Land Electronics Co., Ltd., China). GITT and EIS data of the HC anodes were recorded using a CHI 600 electrochemical test station (China). GITT measurements were performed by applying a series of current pulses at 20 mA/g for 1.0 h, followed by a 10 h relaxation process. EIS data were measured on fully charged states after two cycles in the frequency range of 0.01−105 Hz at 10 mV amplitude.

RESULTS AND DISCUSSION

The hard carbon was prepared using a previously reported method and characterized by SEM and high-resolution TEM (HRTEM). The SEM image shows that the hard carbon material has a spherical shape with a particle size of about 500 nm (Figure 1a). The HRTEM image reveals that the hard

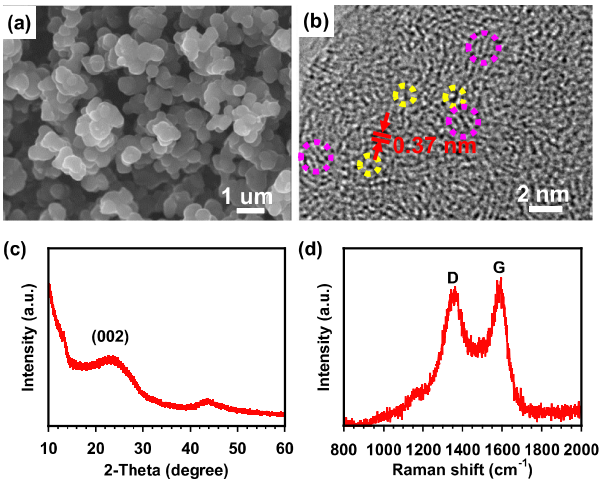

Figure 1. Characterization of the hard carbon: (a) SEM image, (b) HRTEM image, (c) XRD spectrum, and (d) Raman spectrum. Micronanocrystallites (yellow doted cycles) and microvoids (purple doted cycles) are clearly displayed in the HRTEM image (b).

carbon contains randomly oriented graphene layers and nanocrystallite domains (Figure 1b). The disordered arrangement leaves a large amount of microvoids with a pore size of 0.5 nm (Figure 1b). Each nanocrystallite domain is composed of a few stacked graphene layers with a locally ordered structure and an interlayer distance of ~0.37 nm, which is larger than 0.335 nm of graphite. The enlarged spacing is preferred for Na storage.[54,55]

The structure of the hard carbon was further characterized by using XRD, Raman spectroscopy, and CO_2 adsorption/desorption. The XRD pattern shows a broad peak at 2θ = 23.6°, corresponding to the (002) plane and an average interlayer distance of ~0.37 nm (Figure 1c), consistent with the TEM observations. Two strong bands at 1350 and 1580 cm^{-1} are presented in the Raman spectrum. The former is assigned to the defective carbon structures, corresponding to the disordered carbon, while the latter from graphitic carbon, which is associated with the crystallite structure. The Raman spectrum reveals a partially graphitic structure of hard carbon. In the CO_2 adsorption/desorption measurements (Figure S1), two pore sizes were measured. One is 0.37 nm assigned to the

https://doi.org/10.1021/acsami.1c12150
ACS Appl. Mater. Interfaces 2021, 13, 38441−38449

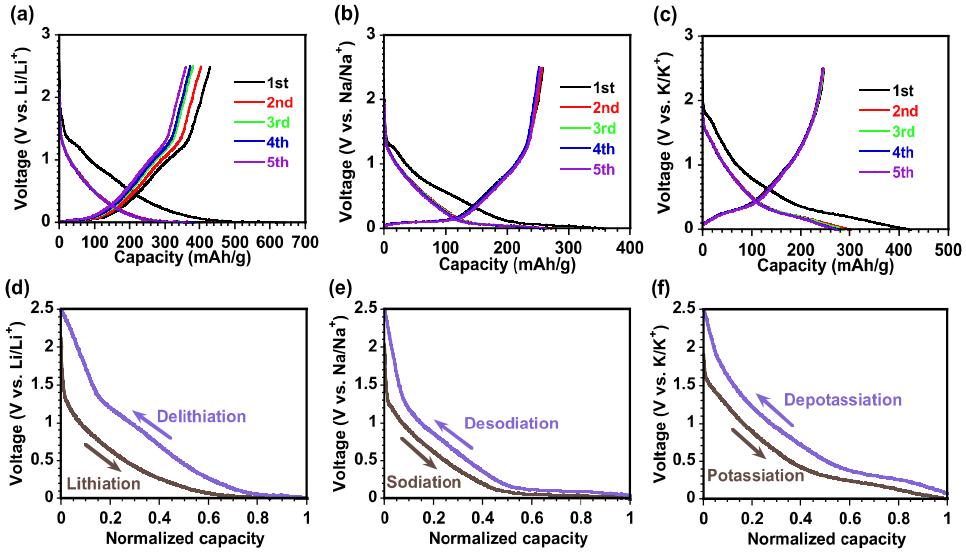

Figure 2. Voltage profiles of (a) Li, (b) Na, and (c) K in the hard carbon anodes in the first five cycles at 20 mA/g and 0−2.5 V, and the normalized voltage curves of (d) Li, (e) Na, and (f) K in the fifth cycle.

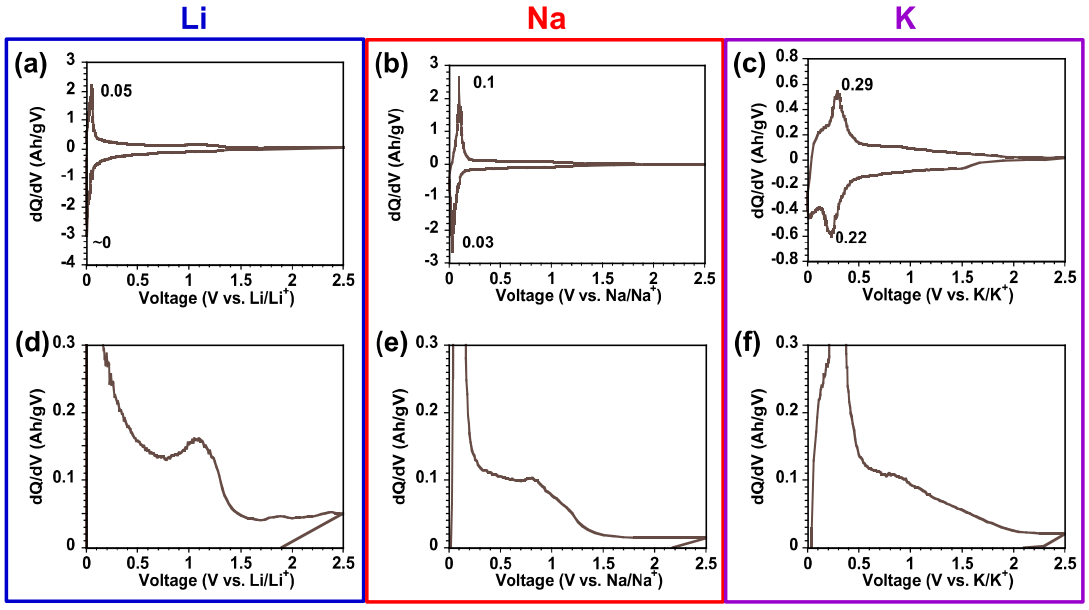

Figure 3. (a−c) dQ/dV and (d−f) enlarged dQ/dV curves of the hard carbon in (a,d) Li-, (b,e) Na-, and (c,f) K-ion batteries.

interlayer space of isolated crystallites and the other at 0.5 nm attributed to micropores produced by the disordered graphene sheets. The large quantity of disordered graphene sheets and micropores provides plenty of active sites for energy storage.

The electrochemical performance of the hard carbon was investigated in coin cells. The insertion/extraction behaviors of Li, Na, and K in the first five cycles are compared in Figures 2 and S2. Small discharge voltage plateaus at 1.3/0.8, 1.3/0.6, and 1.7/0.6 V are displayed in the first cycles for Li, Na, and K storage, respectively, but disappeared in the following cycles (Figure 2a−c). This is attributed to the decomposition of electrolytes to form solid-electrolyte interphase (SEI) films, leading to irreversible capacities. A Coulombic efficiency of 58.3% in the first cycle was observed for K, which is lower than the values of 66.8% of Li and 71.4% of Na (Table S1) and is associated with the larger volume changes induced by the larger K ions.

From the second cycle, a voltage slope at a high voltage above 0.1 V and a plateau close to 0 V are presented in LIBs and NIBs (Figure 2a,b), suggesting two different storage behaviors in the two regions. In the sloping region, different models have been hypothesized, especially those regarding Na storage. The "card house" model ascribed this region to the insertion of Na^+ between graphene sheets within the nanocrystallites,[63,64] while recent studies support the adsorption mechanism at defects/heteroatoms.[54,56,58,59,68] The highly disordered structure consists of numerous structure defects, such as edge hexagonal carbon fragments and heteroatoms (such as oxygen, nitrogen and hydrogen), which provide plenty of storage sites with a wide distribution of binding energy, thus

https://doi.org/10.1021/acsami.1c12150
ACS Appl. Mater. Interfaces 2021, 13, 38441−38449

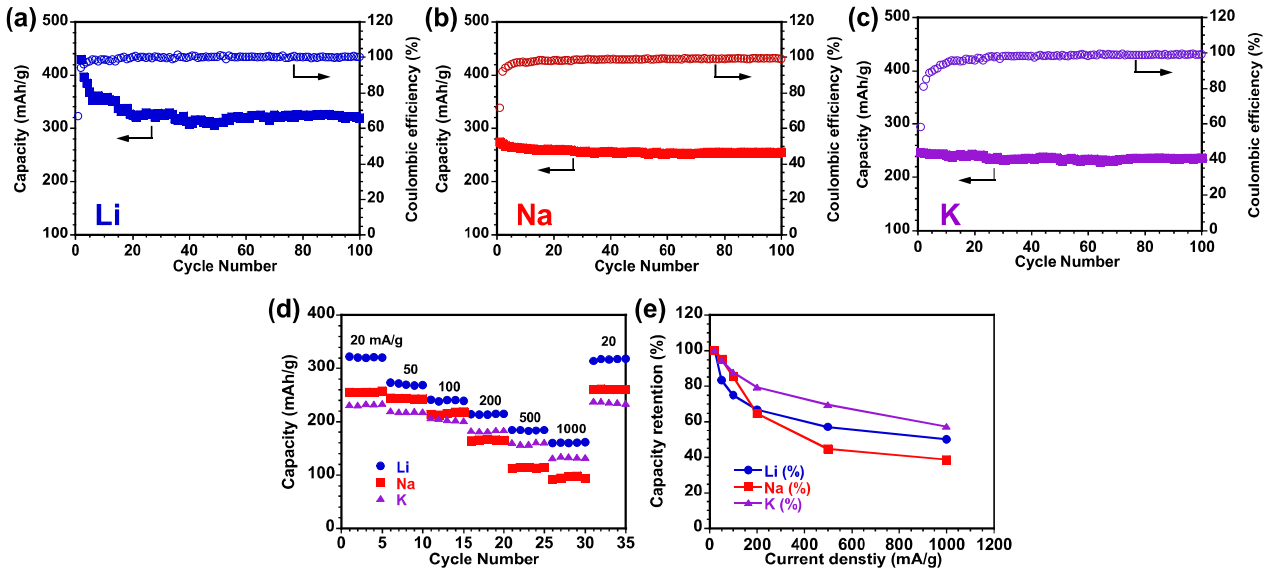

Figure 4. Cycling performance of the hard carbon anodes: cycling performance in (a) LIBs, (b) NIBs, and (c) KIBs at 20 mA/g and 0−2.5 V. (d,e) Rate performance of hard carbon anodes in LIBs, NIBs, and KIBs at current densities from 20 to 1000 mA/g.

forming a voltage slope when binding with metal ions. In contrast to the sloping region, two conflicting mechanisms were proposed for the low-voltage plateau in NIBs. One attributes the plateau capacity to the intercalation between graphene layers within the micro-nanocrystallites,[56,58,60,68] and the other to the pore-filling process into the micropores.[59,63,65] However, it should be pointed out, that they are both mainly derived from XRD measurements. Apparently, it is significantly challenging to elaborate the storage mechanism in hard carbons via surface analysis. In fact, in carbonate-based electrolytes, Na ions are hard to intercalate between graphene layers to produce a voltage plateau below 0.1 V, even with an enlarged interlayer spacing, as revealed by the observations on the expanded graphite.[69] Therefore, the plateau capacity can only be contributed from the pore-filling process, in which the low-voltage plateau can be explained by the extremely weak binding energy between the filled Li or Na ions and carbon atoms in the micropores.

Different from Li and Na storage, the low-voltage plateau shifts up to 0.25 V in the K storage (Figure 2c), implying a different storage behavior for K from those of Li and Na. The voltage change is more clearly illustrated in the logarithmic voltage curves (Figure S2). The rise in the plateau voltage should be associated with the stronger chemical interaction between K ions and C atoms. Similar plateau voltages of hard carbon and graphite anodes in KIBs suggest a similar storage mechanism between them (Figure S3). The pore size of hard carbon is 0.5 nm (Figures 1b and S1), which is smaller than the spacing of potassium-intercalated graphite (0.53 nm).[21] Therefore, when K ions are inserted into micropores, a strong coordination occurred between the K ions and C atoms, making the insertion analogous to the intercalation of potassium into graphite. In contrast, the porous space is relatively larger to accommodate the smaller Li ions, making it impossible to form GICs like that in graphite. It is also noted that, with a larger ionic radius, a weaker chemical interaction with defects/heteroatoms would result in a smaller hysteresis for Na and K than that for Li (Figure 2d−f).

The dimension effects of metal ions on the storage behavior of the hard carbon are further illustrated by the dQ/dV curves in Figure 3. The pore-filling peak shifts from a voltage close to 0 V for Li to 0.1 V for Na and then to 0.29 V for K (Figures 3 and S2), suggesting a dependent relationship on the ionic size of the inserted alkali metal ions. More interestingly, if looking into the enlarged dQ/dV curves, a well-defined anodic peak at around 1.0 V is observed for Li (Figure 3d), which has been assigned to the adsorption at heteroatoms in amorphous carbon materials.[65] This peak becomes weak for Na and almost disappears for K (Figure 3e,f), confirming the variation trend of the chemical binding interaction between the alkali metal ions and heteroatoms from strong to weak as the ions become larger.

Superior performance was achieved for K storage to those of Li and Na. An initial capacity of 247 mA h/g was delivered in the first cycle in K storage, lower than those of Li (429.1 mA h/g) and Na storage (274.9 mA h/g) (Table S1). However, K storage displays the best stability as revealed by the good overlap of voltage profiles in the initial five cycles (Figure 2c). In the fifth cycle, K retained 99% of the capacity in the first cycle, while only 83.8% for Li and 96.4% for Na (Table S1). During the long-term cycling (Figure 4), Li and Na underwent a fast capacity decay in the first 30 cycles, retaining only 76 and 93.5% of their initial capacities, respectively. While K retained 94.3%, much higher than those of Li and Na (Table 1). After 30 cycles, a slow capacity decay still occurred in Li and Na

Table 1. Comparison of Capacity Retention of Hard Carbon Anodes in LIBs, NIBs, and KIBs in the 1st, 30th, and 100th Cycles

	capacity retention					
	1st cycle		30th cycle		100th cycle	
batteries	(mA h/g)	(%)	(mA h/g)	(%)	(mA h/g)	(%)
LIB	429.1	100	326.2	76.0	319.6	74.4
NIB	274.9	100	257.1	93.5	254.9	92.7
KIB	247.2	100	233.2	94.3	237.2	96.0

https://doi.org/10.1021/acsami.1c12150
ACS Appl. Mater. Interfaces 2021, 13, 38441−38449

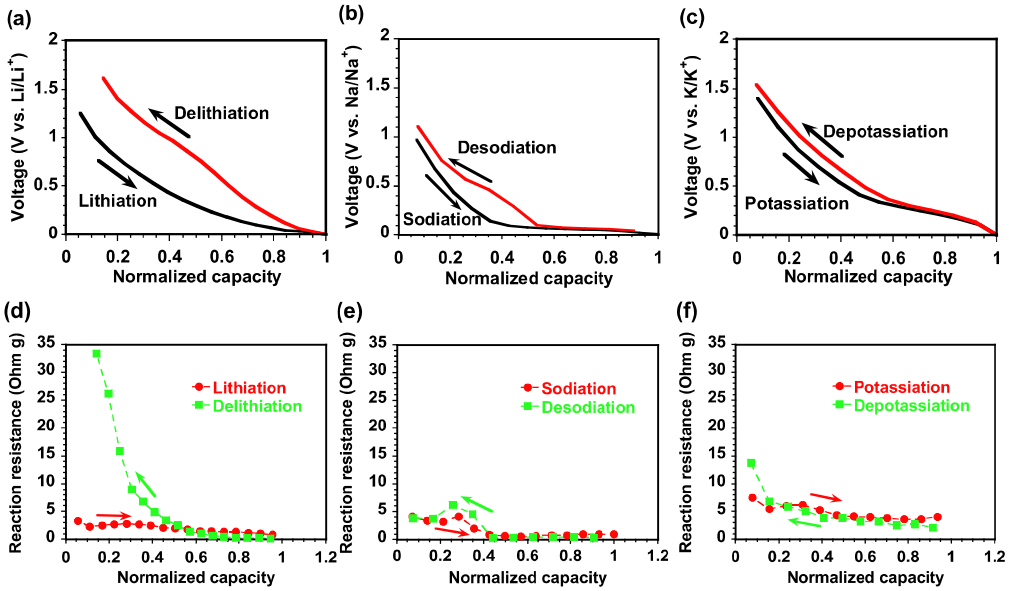

Figure 5. (a–c) Quasi-equilibrium voltage profiles and (d–f) reaction resistances of the hard carbon anodes in (a,d) LIBs, (b,e) NIBs, and (c,f) KIBs analyzed by GITT measurements.

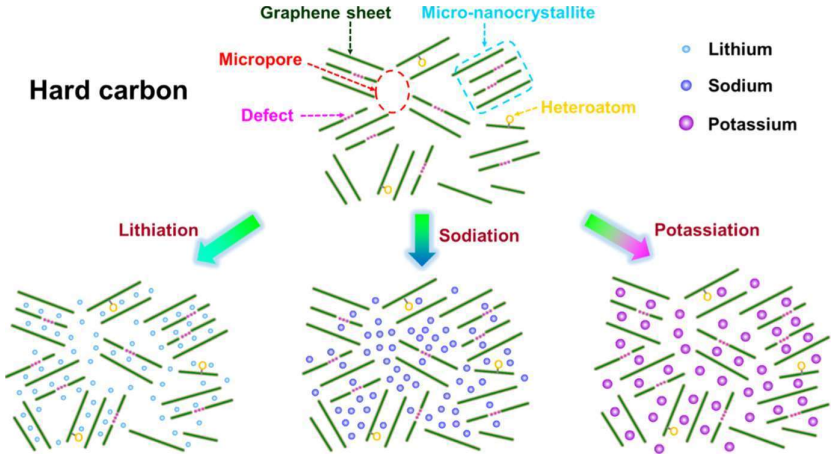

Figure 6. Schematic structure illustration of (top), lithiated (bottom left), sodiated (bottom middle), and potassiated (bottom right) hard carbons.

storage, but there was no capacity loss for K storage (Figure 4a). The exceptional reversibility and stability of the hard carbon for K storage may be associated with the weak interaction between carbon atoms and K ions.

The rate capability of the hard carbon was evaluated at current densities from 20 to 1000 mA/g (Figure 4d,e). Li suffers from a quick capacity roll-off as current increases, particularly at low current density ranges, dropping from 322 mA h/g at 20 mA/g to 215 mA h/g at 200 mA/g. This is mainly caused by the poor tolerance to polarization as a result of the low reaction plateau near 0 V. Na is slightly better than LIBs due to the slightly higher plateau voltage but still show a fast capacity roll-off from 243 to 113 mA h/g as the current density increases from 100 to 500 mA/g. Surprisingly, although K has a much slower diffusion kinetics, better rate capability was achieved with no fast capacity dropping over the testing current rate range. At 500 mA/g, it still retained 161 mA h/g, much higher than the 113 mA h/g of Na (Figure 4d). The exceptional rate capability of the hard carbon electrodes in KIBs is attributed to the high tolerance to polarization because of the high voltage plateau (Figure S4).

The electrochemical insertion behavior and kinetics of Li, Na, and K in the hard carbon anodes were further investigated by GITT, in which the equilibrium potential and overpotential were measured by applying a series of 1 h current pulses at 20 mA/g, followed by a 10 h relaxation process for each current pulse (Figure S5). The open-circuit voltage after 10 h relaxation is assumed to be thermodynamically equilibrium potential. The equilibrium voltage profiles show similar voltage shapes as those obtained by constant current tests (Figures 5a–c and 2d–f), which are composed of a sloping region in the high voltage range and a plateau at a low voltage. A significant voltage hysteresis is displayed for Li (Figure 5a), while it is much smaller for Na and K (Figure 5b,c). In particular, the hysteresis becomes extremely small in the plateau region for Na and K, revealing a different storage behavior in the plateau region from that in the sloping region.

https://doi.org/10.1021/acsami.1c12150
ACS Appl. Mater. Interfaces 2021, 13, 38441–38449

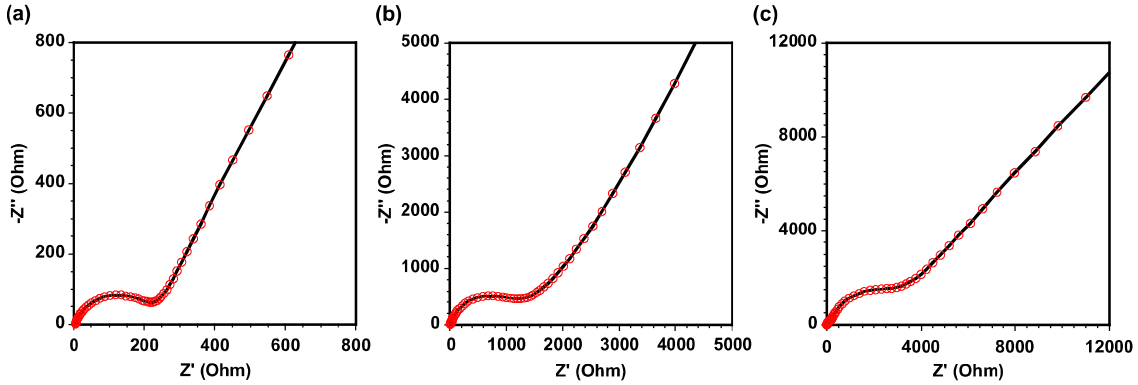

Figure 7. Nyquist plots of the hard carbon anodes in (a) LIBs, (b) NIBs, and (c) KIBs obtained from EIS tests after two activation cycles. Red circle lines are obtained from the experiment, and the black solid lines are the fitted data.

It was also noted that the low-voltage plateau almost disappeared in the equilibrium voltage curves in LIBs (Figure 5a), suggesting that very few Li ions are stored through the pore filling mechanism. Li ions should be mainly attributed to the adsorption at heteroatoms and defective structures. It has been reported that the elimination of heteroatoms and improvement of ordering quality of the micro-nanocrystallites by the heat treatment at a high temperature can significantly reduce the slope capacity,[59] manifesting the adsorption mechanism in the sloping region. In contrast, pore filling behavior contributes a large fraction of capacity in Na and K storage with higher plateau voltages. Unlike the plateau region, however, similar shapes were observed in the sloping region for all three kinds of metal-ion storage except the reducing hysteresis from Li to Na to K, indicating that the adsorption of metal ions at the defects/heteroatoms occurred, regardless of the kind of stored ions. Nevertheless, because of the intercalation capability of Li and K into graphite, it is hard to rule out the insertion of Li and K between graphene layers within the locally ordered micro-nanocrystallites.

On the basis of the above analysis, different storage mechanisms are proposed for the storage of Li, Na, and K in hard carbon anodes, as illustrated in Figure 6. Defect/heteroatom adsorption mainly accounts for the slope capacity for all the Li, Na, and K storage, with a strong dependence of the voltage hysteresis on the ionic diameter. While a notable difference was displayed in the plateau region, that is, pore-filling processes. Within the micropores, it is believed that Li ions are mainly bound to the defective carbon/heteroatom atoms at the edge or/and functional groups on the surface of graphene sheets that form the micropore walls, and very few Li ions overlapped above the bound Li ions as revealed by the absence of a low-voltage plateau in the equilibrium profiles (Figure 5). In contrast, Na ions have a larger ionic radius and are more easy to coordinate with the pore walls, leading to a higher storage potential during the pore filling. Furthermore, the filling of even larger K ions into the micropores produces a stronger coordination with pore walls, resembling the intercalation of K in graphite. It is noteworthy that even if there is no intercalation between the graphene layers for Na ions, the adsorption at defects/heteroatoms within the microcrystallites may enlarge the interlayer space of local-ordered graphene layers as observed in partially oxidized graphite anodes in NIBs.[69] This may explain why a peak shift of the (002) plane in the XRD measurement occurred upon Na-ion insertion.[56]

The reaction kinetics of the hard carbon anodes was also investigated by exploring the reaction resistance that is obtained by dividing an overpotential by the pulse current density (Figures 5d–f and S5). During the insertion process, potassium shows a much higher reaction resistance than Li and Na (Figure S6), which is ascribed to the slow kinetics caused by the larger radius of K ions. However, despite the fact that Na ions are larger than Li ions, a smaller reaction resistance was observed for Na ions than that for Li ions. This can be explained by the stronger interaction of Li ions with defective carbon atoms/heteroatoms as a result of the higher charge density of Li ions. In addition, the reaction resistance decreases along with the insertion advancing for all three kinds of alkali metal ions, which is assigned to the improved conductivity and volume expansion by the inserted metal ions.[48,70] Similar phenomena were also reported for Li- and K-ion insertion in graphite anodes.[21] Upon extraction, K and Na show reverse processes to the insertion due to the reduced conductance, volume contraction, and/or weaker coordination with the host material. Nevertheless, Li suffers from a rapid increase during the deinsertion (Figure 5a), consistent with the strong chemical interaction between the heteroatoms/defects and Li ions.[59,65]

The insertion kinetics of the hard carbon anode was examined by using EIS at a full deinsertion state after two activation cycles. Figure 7 shows the Nyquist plots of the hard carbon electrodes in LIBs, NIBs, and KIBs. Typical impedance curves are presented for the three kinds of batteries, with a depressed semicircle in the high-frequency range followed by a straight line in the low-frequency region. The high-frequency depressed semicircle represents the total resistance of the electrolyte, contact, SEI films, and charge transfer, while the low-frequency sloping line is owing to the ion diffusion and phase transformation in the hard carbon anode. The radius of the high-frequency depressed semicircles gets bigger from Li to Na to K, implying that the kinetics becomes worse as the ionic diameter becomes larger.

To gain further insights into the reaction kinetics of the hard carbon anodes, impedance curves were modeled with equivalent circuits, as shown in Figure S7, where R_s is the Ohmic resistance related to the electrolyte resistance; R_{ct} and R_f represent charge-transfer resistance and contact resistance associated with films, respectively, which are determined by the

https://doi.org/10.1021/acsami.1c12150
ACS Appl. Mater. Interfaces 2021, 13, 38441−38449

diameter of the depressed semicircle; CPEs are capacitors paralleled with R_f and R_{ct}; and Z_w is the Warburg impedance. The values of the resistances are summarized in Table S2. Owing to the weaker solvating effects for larger ions, Ohmic resistance decreases from Li to Na to K, consistent with previous reports.[71] Na shows a much smaller charge-transfer resistance than Li as a result of the weaker binding interaction with defects/heteroatoms. The charge-transfer resistance of K, however, is larger than those of Li and Na, implying a dependence of the charge-transfer kinetics on the ionic diameters. The contact resistance for K is almost 2 times higher than that of Na, which is attributed to the larger volume change for the K-ion insertion/extraction. It is also noted that the sum of the resistances including the electrolyte, charge transfer, and contact resistances becomes bigger as the metal ions become larger. These results are consistent with the observations in the GITT measurements.

CONCLUSIONS

The storage mechanisms of Li, Na, and K ions in hard carbon were for the first time systematically investigated based on electrochemical analysis. In light of voltage profiles, cycling performance, and GITT and EIS measurements, different storage mechanisms are proposed for the storage of Li, Na, and K ions in hard carbon anodes. Li ions are mainly adsorbed at defects, edges, and functional groups, producing a sloping voltage shape, but pore filling contributes very little to Li storage capacity. Besides the adsorption effects in the sloping region, a large fraction of capacity at the low-voltage plateau is assigned to the pore-filling process in NIBs. K ions are adsorbed at defects/heteroatoms with a reduced voltage hysteresis and inserted into the micropores at an elevated plateau voltage compared to those of Li and Na. The elevated voltage plateau not only enhances the rate capability but also reduces the safety hazards caused by plating/stripping on the anode electrode surface. Therefore, larger ions might be potentially favorable for hard carbon anodes to achieve high reversibility, good cycling stability, and excellent rate capability as revealed by the superior storage performance of K compared to those of Li and Na. Our findings provide a comprehensive understanding of the storage mechanisms of alkali metal ions in hard carbon anodes from an electrochemical point of view.

ASSOCIATED CONTENT

Supporting Information

The Supporting Information is available free of charge at https://pubs.acs.org/doi/10.1021/acsami.1c12150.

NLDFT micropore size distribution by CO_2 adsorption measurements and GITT measurements of hard carbon and a comparison of voltage curves of graphite and hard carbon (PDF)

AUTHOR INFORMATION

Corresponding Authors

Yong Huang − *Guangdong Industrial Training Center, Guangdong Polytechnic Normal University, Guangzhou 510665, China*; Email: gsdhuangy@gpnu.edu.cn

Yunhua Xu − *School of Materials Science and Engineering, Key Laboratory of Advanced Ceramics and Machining Technology (Ministry of Education), and Tianjin Key Laboratory of Composite and Functional Materials, Tianjin University, Tianjin 300072, China*; orcid.org/0000-0003-1818-3661; Email: yunhua.xu@tju.edu.cn

Authors

Yuqing Wang − *School of Materials Science and Engineering, Key Laboratory of Advanced Ceramics and Machining Technology (Ministry of Education), and Tianjin Key Laboratory of Composite and Functional Materials, Tianjin University, Tianjin 300072, China*

Panxing Bai − *School of Materials Science and Engineering, Key Laboratory of Advanced Ceramics and Machining Technology (Ministry of Education), and Tianjin Key Laboratory of Composite and Functional Materials, Tianjin University, Tianjin 300072, China*

Complete contact information is available at: https://pubs.acs.org/10.1021/acsami.1c12150

Notes

The authors declare no competing financial interest.

ACKNOWLEDGMENTS

We acknowledge the financial support from the National Key Research and Development Program of China (grant no.: 2019YFE0118800) and the Project of Innovation in Colleges and Universities of Guangdong Province (grant no. 2019KTSCX084).

REFERENCES

(1) Pan, Q.; Wu, Y.; Zhong, W.; Zheng, F.; Li, Y.; Liu, Y.; Hu, J.; Yang, C. Carbon Nanosheets Encapsulated NiSb Nanoparticles as Advanced Anode Materials for Lithium-Ion Batteries. *Energy Environ. Mater.* **2020**, *3*, 186−191.

(2) Zhao, C.; Wang, Q.; Yao, Z.; Wang, J.; Sánchez-Lengeling, B.; Ding, F.; Qi, X.; Lu, Y.; Bai, X.; Li, B.; Li, H.; Aspuru-Guzik, A.; Huang, X.; Delmas, C.; Wagemaker, M.; Chen, L.; Hu, Y.-S. Rational Design of Layered Oxide Materials for Sodium-Ion Batteries. *Science* **2020**, *370*, 708−711.

(3) Shen, X.; Zhou, Q.; Han, M.; Qi, X.; Li, B.; Zhang, Q.; Zhao, J.; Yang, C.; Liu, H.; Hu, Y.-S. Rapid Mechanochemical Synthesis of Polyanionic Cathode with Improved Electrochemical Performance for Na-Ion Batteries. *Nat. Commun.* **2021**, *12*, 2848.

(4) Zhang, S.-W.; Lv, W.; Luo, C.; You, C.-H.; Zhang, J.; Pan, Z.-Z.; Kang, F.-Y.; Yang, Q.-H. Commercial Carbon Molecular Sieves as a High Performance Anode for Sodium-Ion Batteries. *Energy Storage Mater.* **2016**, *3*, 18−23.

(5) Zheng, X.; Gu, Z.; Liu, X.; Wang, Z.; Wen, J.; Wu, X.; Luo, W.; Huang, Y. Bridging the Immiscibility of an All-Fluoride Fire Extinguishant with Highly-Fluorinated Electrolytes toward Safe Sodium Metal Batteries. *Energy Environ. Sci.* **2020**, *13*, 1788−1798.

(6) Zhang, Y.; Foster, C. W.; Banks, C. E.; Shao, L.; Hou, H.; Zou, G.; Chen, J.; Huang, Z.; Ji, X. Graphene-Rich Wrapped Petal-Like Rutile TiO_2 Tuned by Carbon Dots for High-Performance Sodium Storage. *Adv. Mater.* **2016**, *28*, 9391−9399.

(7) Guo, S.; Liu, P.; Sun, Y.; Zhu, K.; Yi, J.; Chen, M.; Ishida, M.; Zhou, H. A High-Voltage and Ultralong-Life Sodium Full Cell for Stationary Energy Storage. *Angew. Chem., Int. Ed.* **2015**, *127*, 11867−11871.

(8) Wang, L.; Lu, Y.; Liu, J.; Xu, M.; Cheng, J.; Zhang, D.; Goodenough, J. B. A Superior Low-Cost Cathode for a Na-Ion Battery. *Angew. Chem., Int. Ed.* **2013**, *125*, 2018−2021.

(9) Cheng, S.; Yao, K.; Zheng, K.; Li, Q.; Chen, D.; Jiang, Y.; Liu, W.; Feng, Y.; Rui, X.; Yu, Y. Self-Assembled VS_4 Hierarchitectures with Enhanced Capacity and Stability for Sodium Storage. *Energy Environ. Mater.* **2021**, 1−7.

(10) Wan, Y.; Song, K.; Chen, W.; Qin, C.; Zhang, X.; Zhang, J.; Dai, H.; Hu, Z.; Yan, P.; Liu, C.; Sun, S.; Chou, S. L.; Shen, C. Ultra-

High Initial Coulombic Efficiency Induced by Interface Engineering Enables Rapid, Stable Sodium Storage. *Angew. Chem., Int. Ed.* **2021**, *60*, 11481−11486.
(11) Wang, Q.; Mariyappan, S.; Rousse, G.; Morozov, A. V.; Porcheron, B.; Dedryvère, R.; Wu, J.; Yang, W.; Zhang, L.; Chakir, M.; Avdeev, M.; Deschamps, M.; Yu, Y.-S.; Cabana, J.; Doublet, M.-L.; Abakumov, A. M.; Tarascon, J.-M. Unlocking Anionic Redox Activity in O3-Type Sodium 3D Layered Oxides via Li Substitution. *Nat. Mater.* **2021**, *20*, 353−361.
(12) Shi, J.; Ding, L.; Wan, Y.; Mi, L.; Chen, L.; Yang, D.; Hu, Y.; Chen, W. Achieving Long-Cycling Sodium-Ion Full Cells in Ether-Based Electrolyte with Vinylene Carbonate Additive. *J. Energy Chem.* **2021**, *57*, 650−655.
(13) Lin, Z.; Xia, Q.; Wang, W.; Li, W.; Chou, S. Recent research progresses in ether- and ester-based electrolytes for sodium-ion batteries. *Infomatics* **2019**, *1*, 376−389.
(14) Zhang, J.; Liu, Y.; Zhao, X.; He, L.; Liu, H.; Song, Y.; Sun, S.; Li, Q.; Xing, X.; Chen, J. a Novel NASICON-Type $Na_4MnCr(PO_4)_3$ Demonstrating the Energy Density Record of Phosphate Cathodes for Sodium-Ion Batteries. *Adv. Mater.* **2020**, *32*, 1906348.
(15) Qin, J.; Wang, T.; Liu, D.; Liu, E.; Zhao, N.; Shi, C.; He, F.; Ma, L.; He, C. A Top-Down Strategy toward SnSb In-Plane Nanoconfined 3D N-Doped Porous Graphene Composite Microspheres for High Performance Na-Ion Battery Anode. *Adv. Mater.* **2018**, *30*, 1704670.
(16) Xiong, P.; Bai, P.; Li, A.; Li, B.; Cheng, M.; Chen, Y.; Huang, S.; Jiang, Q.; Bu, X. H.; Xu, Y. Bismuth Nanoparticle@Carbon Composite Anodes for Ultralong Cycle Life and High-Rate Sodium-Ion Batteries. *Adv. Mater.* **2019**, *31*, 1904771.
(17) Bai, P.; He, Y.; Xiong, P.; Zhao, X.; Xu, K.; Xu, Y. Long cycle life and High Rate Sodium-Ion Chemistry for Hard Carbon Anodes. *Energy Storage Mater.* **2018**, *13*, 274−282.
(18) Bai, P.; Han, X.; He, Y.; Xiong, P.; Zhao, Y.; Sun, J.; Xu, Y. Solid Electrolyte Interphase Manipulation towards Highly Stable Hard Carbon Anodes for Sodium Ion Batteries. *Energy Storage Mater.* **2020**, *25*, 324−333.
(19) Sun, J.; Lee, H.-W.; Pasta, M.; Yuan, H.; Zheng, G.; Sun, Y.; Li, Y.; Cui, Y. A Phosphorene-Graphene Hybrid Material as a High-Capacity Anode for Sodium-Ion Batteries. *Nat. Nanotechnol.* **2015**, *10*, 980−985.
(20) Yabuuchi, N.; Kajiyama, M.; Iwatate, J.; Nishikawa, H.; Hitomi, S.; Okuyama, R.; Usui, R.; Yamada, Y.; Komaba, S. P2-Type $Na_x[Fe_{1/2}Mn_{1/2}]O_2$ Made from Earth-Abundant Elements for Rechargeable Na Batteries. *Nat. Mater.* **2012**, *11*, 512−517.
(21) Zhao, J.; Zou, X.; Zhu, Y.; Xu, Y.; Wang, C. Electrochemical Intercalation of Potassium into Graphite. *Adv. Funct. Mater.* **2016**, *26*, 8103−8110.
(22) Zhou, M.; Qi, W.; Hu, Z.; Cheng, M.; Zhao, X.; Xiong, P.; Su, H.; Li, M.; Hu, J.; Xu, Y. Highly Potassiophilic Carbon Nanofiber Paper Derived from Bacterial Cellulose Enables Ultra-Stable Dendrite-Free Potassium Metal Anodes. *ACS Appl. Mater. Interfaces* **2021**, *13*, 17629−17638.
(23) Xiong, P.; Yin, H.; Chen, Z.; Zhao, C.; Yang, J.; Huang, S.; Xu, Y. Thiourea-based polyimide/RGO composite cathode: A Comprehensive Study of Storage Mechanism with Alkali Metal Ions. *Sci. China Mater.* **2020**, *63*, 1929−1938.
(24) Wang, M.; Lu, W.; Zhang, H.; Li, X. Organic Electrode Materials for Non-aqueous K-Ion Batteries. *Trans. Tianjin Univ.* **2020**, *27*, 1−23.
(25) Ding, J.; Zhang, H.; Fan, W.; Zhong, C.; Hu, W.; Mitlin, D. Review of Emerging Potassium-Sulfur Batteries. *Adv. Mater.* **2020**, *32*, 1908007.
(26) Hosaka, T.; Kubota, K.; Hameed, A. S.; Komaba, S. Research Development on K-Ion Batteries. *Chem. Rev.* **2020**, *120*, 6358−6466.
(27) Luo, C.; Fan, X.; Ma, Z.; Gao, T.; Wang, C. Self-Healing Chemistry between Organic Material and Binder for Stable Sodium-Ion Batteries. *Chem* **2017**, *3*, 1050−1062.
(28) Liu, Y.; Fan, F.; Wang, J.; Liu, Y.; Chen, H.; Jungjohann, K. L.; Xu, Y.; Zhu, Y.; Bigio, D.; Zhu, T.; Wang, C. In Situ Transmission Electron Microscopy Study of Electrochemical Sodiation and Potassiation of Carbon Nanofibers. *Nano Lett.* **2014**, *14*, 3445−3452.
(29) Luo, W.; Wan, J.; Ozdemir, B.; Bao, W.; Chen, Y.; Dai, J.; Lin, H.; Xu, Y.; Gu, F.; Barone, V.; Hu, L. Potassium Ion Batteries with Graphitic Materials. *Nano Lett.* **2015**, *15*, 7671−7677.
(30) Zhang, R.; Huang, J.; Deng, W.; Bao, J.; Pan, Y.; Huang, S.; Sun, C. F. Safe, Low-Cost, Fast-Kinetics and Low-Strain Inorganic-Open-Framework Anode for Potassium-Ion Batteries. *Angew. Chem., Int. Ed.* **2019**, *58*, 16474−16479.
(31) Xiao, N.; McCulloch, W. D.; Wu, Y. Reversible Dendrite-Free Potassium Plating and Stripping Electrochemistry for Potassium Secondary Batteries. *J. Am. Chem. Soc.* **2017**, *139*, 9475−9478.
(32) Zhao, X.; Hong, Y.; Cheng, M.; Wang, S.; Zheng, L.; Wang, J.; Xu, Y. High Performance Potassium-Sulfur Batteries and Their Reaction Mechanism. *J. Mater. Chem. A* **2020**, *8*, 10875−10884.
(33) Li, B.; Zhao, J.; Zhang, Z.; Zhao, C.; Sun, P.; Bai, P.; Yang, J.; Zhou, Z.; Xu, Y. Electrolyte-Regulated Solid-Electrolyte Interphase Enables Long Cycle Life Performance in Organic Cathodes for Potassium-Ion Batteries. *Adv. Funct. Mater.* **2018**, *29*, 1807137.
(34) Sui, D.; Chang, M.; Wang, H.; Qian, H.; Yang, Y.; Li, S.; Zhang, Y.; Song, Y. A Brief Review of Catalytic Cathode Materials for Na-CO_2 Batteries. *Catalysts* **2021**, *11*, 603.
(35) Liu, Y.; Deng, Q.; Li, Y.; Li, Y.; Zhong, W.; Hu, J.; Ji, X.; Yang, C.; Lin, Z.; Huang, K. CoSe@N-Doped Carbon Nanotubes as a Potassium-Ion Battery Anode with High Initial Coulombic Efficiency and Superior Capacity Retention. *ACS Nano* **2021**, *15*, 1121−1132.
(36) Liu, Q.; Deng, W.; Sun, C.-F. A Potassium-Tellurium battery. *Energy Storage Mater.* **2020**, *28*, 10−16.
(37) Hwang, J.-Y.; Oh, S.-M.; Myung, S.-T.; Chung, K. Y.; Belharouak, I.; Sun, Y.-K. Radially Aligned Hierarchical Columnar Structure as a Cathode Material for High Energy Density Sodium-Ion Batteries. *Nat. Commun.* **2015**, *6*, 6865.
(38) Zhu, Y.; Xu, Y.; Liu, Y.; Luo, C.; Wang, C. Comparison of Electrochemical Performances of Olivine $NaFePO_4$ in Sodium-Ion Batteries and Olivine $LiFePO_4$ in Lithium-Ion Batteries. *Nanoscale* **2013**, *5*, 780−787.
(39) Jin, T.; Liu, Y.; Li, Y.; Cao, K.; Wang, X.; Jiao, L. Electrospun $NaVPO_4F$/C Nanofibers as Self-Standing Cathode Material for Ultralong Cycle Life Na-Ion Batteries. *Adv. Energy Mater.* **2017**, *7*, 1700087.
(40) Hu, Z.; Zhu, Z.; Cheng, F.; Zhang, K.; Wang, J.; Chen, C.; Chen, J. Pyrite FeS_2 for high-rate and long-life rechargeable sodium batteries. *Energy Environ. Sci.* **2015**, *8*, 1309−1316.
(41) Zhu, Y.; Suo, L.; Gao, T.; Fan, X.; Han, F.; Wang, C. Ether-based electrolyte enabled Na/FeS_2 rechargeable batteries. *Electrochem. Commun.* **2015**, *54*, 18−22.
(42) Wang, Y.-X.; Yang, J.; Chou, S.-L.; Liu, H. K.; Zhang, W.-x.; Zhao, D.; Dou, S. X. Uniform yolk-shell iron sulfide-carbon nanospheres for superior sodium-iron sulfide batteries. *Nat. Commun.* **2015**, *6*, 8689.
(43) Zhang, S.-W.; Cao, T.; Lv, W.; Zhang, J.; Tao, Y.; Kang, F.; Wang, D.-W.; Yang, Q.-H. High-Performance Graphene/Disodium Terephthalate Electrodes with Ether Electrolyte for Exceptional Cooperative Sodiation/Desodiation. *Nano Energy* **2020**, *77*, 105203.
(44) Tang, M.; Zhu, S.; Liu, Z.; Jiang, C.; Wu, Y.; Li, H.; Wang, B.; Wang, E.; Ma, J.; Wang, C. Tailoring π-Conjugated Systems: From π-π Stacking to High-Rate-Performance Organic Cathodes. *Chem* **2018**, *4*, 2600−2614.
(45) Lee, M.; Hong, J.; Lopez, J.; Sun, Y.; Feng, D.; Lim, K.; Chueh, W. C.; Toney, M. F.; Cui, Y.; Bao, Z. High-Performance Sodium-Organic Battery by Realizing Four-Sodium Storage in Disodium Rhodizonate. *Nat. Energy* **2017**, *2*, 861−868.
(46) Wang, L.; Ni, Y.; Hou, X.; Chen, L.; Li, F.; Chen, J. A Two-Dimensional Metal-Organic Polymer Enabled by Robust Nickel-Nitrogen and Hydrogen Bonds for Exceptional Sodium-Ion Storage. *Angew. Chem., Int. Ed.* **2020**, *59*, 22126−22131.
(47) Mao, M.; Luo, C.; Pollard, T. P.; Hou, S.; Gao, T.; Fan, X.; Cui, C.; Yue, J.; Tong, Y.; Yang, G.; Deng, T.; Zhang, M.; Ma, J.; Suo, L.;

Borodin, O.; Wang, C. A Pyrazine-Based Polymer for Fast-Charge Batteries. *Angew. Chem., Int. Ed.* **2019**, *58*, 17820−17826.
(48) Dresselhaus, M. S.; Dresselhaus, G. Intercalation Compounds of Graphite. *Adv. Phys.* **2002**, *51*, 1−186.
(49) Komaba, S.; Murata, W.; Ishikawa, T.; Yabuuchi, N.; Ozeki, T.; Nakayama, T.; Ogata, A.; Gotoh, K.; Fujiwara, K. Electrochemical Na Insertion and Solid Electrolyte Interphase for Hard-Carbon Electrodes and Application to Na-Ion Batteries. *Adv. Funct. Mater.* **2011**, *21*, 3859−3867.
(50) Liu, S.; Mao, J.; Zhang, L.; Pang, W. K.; Du, A.; Guo, Z. Manipulating the Solvation Structure of Nonflammable Electrolyte and Interface to Enable Unprecedented Stability of Graphite Anodes beyond 2 Years for Safe Potassium-Ion Batteries. *Adv. Mater.* **2021**, *33*, 2006313.
(51) Jian, Z.; Hwang, S.; Li, Z.; Hernandez, A. S.; Wang, X.; Xing, Z.; Su, D.; Ji, X. Hard-Soft Composite Carbon as a Long-Cycling and High-Rate Anode for Potassium-Ion Batteries. *Adv. Funct. Mater.* **2017**, *27*, 1700324.
(52) Zhao, X.; Xiong, P.; Meng, J.; Liang, Y.; Wang, J.; Xu, Y. High Rate and Long Cycle Life Porous Carbon Nanofiber Paper Anodes for Potassium-Ion Batteries. *J. Mater. Chem. A* **2017**, *5*, 19237−19244.
(53) Li, W.; Zeng, L.; Yang, Z.; Gu, L.; Wang, J.; Liu, X.; Cheng, J.; Yu, Y. Free-Standing and Binder-Free Sodium-Ion Electrodes with Ultralong Cycle Life and High Rate Performance Based on Porous Carbon Nanofibers. *Nanoscale* **2014**, *6*, 693−698.
(54) Bai, P.; He, Y.; Zou, X.; Zhao, X.; Xiong, P.; Xu, Y. Elucidation of the Sodium-Storage Mechanism in Hard Carbons. *Adv. Energy Mater.* **2018**, *8*, 1703217.
(55) Zhao, L. F.; Hu, Z.; Lai, W. H.; Tao, Y.; Peng, J.; Miao, Z. C.; Wang, Y. X.; Chou, S. L.; Liu, H. K.; Dou, S. X. Hard Carbon Anodes: Fundamental Understanding and Commercial Perspectives for Na-Ion Batteries beyond Li-Ion and K-Ion Counterparts. *Adv. Energy Mater.* **2020**, *11*, 2002704.
(56) Bommier, C.; Surta, T. W.; Dolgos, M.; Ji, X. New Mechanistic Insights on Na-Ion Storage in Nongraphitizable Carbon. *Nano Lett.* **2015**, *15*, 5888−5892.
(57) Li, Y.; Hu, Y.-S.; Titirici, M.-M.; Chen, L.; Huang, X. Hard Carbon Microtubes Made from Renewable Cotton as High-Performance Anode Material for Sodium-Ion Batteries. *Adv. Energy Mater.* **2016**, *6*, 1600659.
(58) Qiu, S.; Xiao, L.; Sushko, M. L.; Han, K. S.; Shao, Y.; Yan, M.; Liang, X.; Mai, L.; Feng, J.; Cao, Y.; Ai, X.; Yang, H.; Liu, J. Manipulating Adsorption-Insertion Mechanisms in Nanostructured Carbon Materials for High-Efficiency Sodium Ion Storage. *Adv. Energy Mater.* **2017**, *7*, 1700403.
(59) Zhang, B.; Ghimbeu, C. M.; Laberty, C.; Vix-Guterl, C.; Tarascon, J.-M. Correlation Between Microstructure and Na Storage Behavior in Hard Carbon. *Adv. Energy Mater.* **2016**, *6*, 1501588.
(60) Cao, Y.; Xiao, L.; Sushko, M. L.; Wang, W.; Schwenzer, B.; Xiao, J.; Nie, Z.; Saraf, L. V.; Yang, Z.; Liu, J. Sodium Ion Insertion in Hollow Carbon Nanowires for Battery Applications. *Nano Lett.* **2012**, *12*, 3783−3787.
(61) Sun, N.; Guan, Z.; Liu, Y.; Cao, Y.; Zhu, Q.; Liu, H.; Wang, Z.; Zhang, P.; Xu, B. Extended "Adsorption-Insertion" Model: A New Insight into the Sodium Storage Mechanism of Hard Carbons. *Adv. Energy Mater.* **2019**, *9*, 1901351.
(62) Li, Y.; Lu, Y.; Meng, Q.; Jensen, A. C. S.; Zhang, Q.; Zhang, Q.; Tong, Y.; Qi, Y.; Gu, L.; Titirici, M. M.; Hu, Y. S. Regulating Pore Structure of Hierarchical Porous Waste Cork-Derived Hard Carbon Anode for Enhanced Na Storage Performance. *Adv. Energy Mater.* **2019**, *9*, 1902852.
(63) Stevens, D. A.; Dahn, J. R. High Capacity Anode Materials for Rechargeable Sodium-Ion Batteries. *J. Electrochem. Soc.* **2000**, *147*, 1271−1273.
(64) Stevens, D. A.; Dahn, J. R. An In Situ Small-Angle X-Ray Scattering Study of Sodium Insertion into a Nanoporous Carbon Anode Material within an Operating Electrochemical Cell. *J. Electrochem. Soc.* **2000**, *147*, 4428−4431.
(65) Stevens, D. A.; Dahn, J. R. The Mechanisms of Lithium and Sodium Insertion in Carbon Materials. *J. Electrochem. Soc.* **2001**, *148*, A803−A811.
(66) Gotoh, K.; Ishikawa, T.; Shimadzu, S.; Yabuuchi, N.; Komaba, S.; Takeda, K.; Goto, A.; Deguchi, K.; Ohki, S.; Hashi, K.; Shimizu, T.; Ishida, H. NMR study for Electrochemically Inserted Na in Hard Carbon Electrode of Sodium Ion Battery. *J. Power Sources* **2013**, *225*, 137−140.
(67) Morikawa, Y.; Nishimura, S.; Hashimoto, R.; Ohnuma, M.; Yamada, A. Mechanism of Sodium Storage in Hard Carbon: An X-Ray Scattering Analysis. *Adv. Energy Mater.* **2020**, *10*, 1903176.
(68) Li, Z.; Bommier, C.; Chong, Z. S.; Jian, Z.; Surta, T. W.; Wang, X.; Xing, Z.; Neuefeind, J. C.; Stickle, W. F.; Dolgos, M.; Greaney, P. A.; Ji, X. Mechanism of Na-Ion Storage in Hard Carbon Anodes Revealed by Heteroatom Doping. *Adv. Energy Mater.* **2017**, *7*, 1602894.
(69) Wen, Y.; He, K.; Zhu, Y.; Han, F.; Xu, Y.; Matsuda, I.; Ishii, Y.; Cumings, J.; Wang, C. Expanded Graphite as Superior Anode for Sodium-Ion Batteries. *Nat. Commun.* **2014**, *5*, 4033.
(70) Xu, Y.; Zhu, Y.; Liu, Y.; Wang, C. Electrochemical Performance of Porous Carbon/Tin Composite Anodes for Sodium-Ion and Lithium-Ion Batteries. *Adv. Energy Mater.* **2013**, *3*, 128−133.
(71) Komaba, S.; Hasegawa, T.; Dahbi, M.; Kubota, K. Potassium Intercalation into Graphite to Realize High-Voltage/High-Power Potassium-Ion Batteries and Potassium-Ion Capacitors. *Electrochem. Commun.* **2015**, *60*, 172−175.
(72) Xu, Y.; Wen, Y.; Zhu, Y.; Gaskell, K.; Cychosz, K. A.; Eichhorn, B.; Xu, K.; Wang, C. Confined Sulfur in Microporous Carbon Renders Superior Cycling Stability in Li/S Batteries. *Adv. Funct. Mater.* **2015**, *25*, 4312−4320.

https://doi.org/10.1021/acsami.1c12150
ACS Appl. Mater. Interfaces 2021, 13, 38441−38449